



HAL
open science

Development of beam transverse profile and emittance monitors for the CERN LINAC4

Benjamin Cheymol

► **To cite this version:**

Benjamin Cheymol. Development of beam transverse profile and emittance monitors for the CERN LINAC4. Other [cond-mat.other]. Université Blaise Pascal - Clermont-Ferrand II, 2011. English. NNT : 2011CLF22201 . tel-00877031

HAL Id: tel-00877031

<https://theses.hal.science/tel-00877031>

Submitted on 25 Oct 2013

HAL is a multi-disciplinary open access archive for the deposit and dissemination of scientific research documents, whether they are published or not. The documents may come from teaching and research institutions in France or abroad, or from public or private research centers.

L'archive ouverte pluridisciplinaire **HAL**, est destinée au dépôt et à la diffusion de documents scientifiques de niveau recherche, publiés ou non, émanant des établissements d'enseignement et de recherche français ou étrangers, des laboratoires publics ou privés.

Numéro d'ordre: DU 2201
EDSF: 702

PCCF 1110

UNIVERSITÉ CLERMONT-FERRAND II - BLAISE PASCAL

(U.F.R. de Recherche Scientifique et Technique)

Ecole Doctorale des Sciences Fondamentales

THÈSE

préparée au CERN/BE/BI
pour obtenir le grade de

Docteur d'Université
dans la spécialité de Physique des Particules

par

Benjamin Cheymol

**Development of beam transverse profile and
emittance monitors for the CERN LINAC4**

Thèse soutenue le 15 décembre 2011 devant le jury:

Président:	M. Pierre Henrard	UBP Clermont-Ferrand, France
Rapporteurs:	M. Christian Carli M. De Conto Jean Marie	CERN, Genève, Switzerland (absent) LPSC, Grenoble, France
Directeur de thèse:	M. Claudio Santoni M. Federico Roncarolo	UBP Clermont-Ferrand, France CERN, Genève, Switzerland
	M. Uli Raich M. Enrico Bravin	CERN, Genève, Switzerland CERN, Genève, Switzerland

Abstract

LINAC4 is part of the CERN Large Hadron Collider injector chain upgrade (LIU) and will accelerate H^- ions from 45 keV to 160 MeV, it will be the first step of the upgrade with the replacement of LINAC2 in 2018.

In order to measure beam profiles along the LINAC, several SEM grid and wire beam scanner (WS) monitors will be installed between the RF cavities from 50 MeV to 160 MeV. This thesis covers all monitor design aspects intended to cope with the required specifications. In particular, the overall measurement robustness, accuracy and sensitivity must be satisfied for different commissioning and operational scenarios. The physics mechanisms generating the wire signals and the wire resistance to beam induced thermal loads have been considered in order to determine the most appropriate monitor design in terms of wire material and dimensions.

In addition, for the commissioning phase, a movable diagnostics test bench will be used to adjust the machine parameters during different stages of installation. One of the main instruments on this movable bench is a transverse emittance meter. This thesis presents the different studies done for the mechanical design of the slit and for the estimation of the systematical error on the measurement due to space charge and multiple scattering. To complete this section, the first results of the commissioning of the LINAC4 ions source and LEBT are presented, together with results from emittance measurement taken at the Spallation Neutron Source in Oak Ridge (Tennessee, USA).

This last part of the thesis presents different studies done for a beam profiles and emittance measurements with a laser wire, with a large input from the SNS beam diagnostic group.

Résumé

Dans les prochaines années, le complexe d'accélérateur du CERN va subir une profonde mise à jour dont le but est une augmentation de la luminosité du LHC. Le projet LIU (LHC Injectors Upgrade) coordonne les mises à jour des différentes parties de la chaîne d'injection. Le projet LINAC4 s'inscrit dans ce cadre et sera la première étape de la mise à jour.

Cette thèse présente les différentes études conduites lors du développement de l'instrumentation nécessaire à la mesure du faisceau. Ce travail est limité aux instruments permettant la mesure des profils transverses (taille et émittance). La thèse se divise en quatre parties.

La première partie, composée des trois premiers chapitres, est vue comme une partie d'introduction où il sera présenté le projet LINAC4 ainsi que les différents aperçus théoriques nécessaires à la conception de types d'instruments requis. Le chapitre 2 décrit brièvement la dynamique des faisceaux dans un accélérateur et présente également des rappels théoriques sur l'effet de charge d'espace induit par le faisceau. Le chapitre 3 est un rappel sur les interactions entre particules et matière.

La seconde partie, comprenant les chapitres 4 à 6, décrit les différentes études menées lors de la conception des SEM grid, wire scanner et emittance mètre. Le lecteur trouvera dans cette partie une description des instruments mentionnés et qui seront déployés lors de la phase de test et pendant la phase d'opération du LINAC4.

Le chapitre 4 s'attarde sur les effets de charge thermique induite sur les fils des SEM grid et wire beam scanner par le faisceau et leur conséquence sur la survie de ces fils. Le LINAC4 va produire un faisceau intense d'ion H^- , avec une taille de faisceau de l'ordre du millimètre, cette densité de particule va, à basse énergie, induire un grand dépôt d'énergie dans la matière. La hausse de température qui en résulte peut dépasser les limites thermomécaniques des matériaux usuels employés pour ce type de mesure. Cette étude permet de déterminer le matériau idéal pour le fil et d'imposer certaines restrictions sur l'utilisation des différents moniteurs de profils. Au sein de ce chapitre il est aussi présenté une estimation des signaux obtenus pour des géométries et des matériaux de fils différents.

Les chapitres 5 et 6 sont une étude de l'émittance mètre à moyenne énergie du LINAC4 (3 et 12 MeV), le système employé est un système dit "Slit & grid", où une fente permet de sélectionner une faible partie du faisceau, le reste étant absorbé, le profil du faisceau non perturbé est mesuré par une grille.

Le chapitre 5 présente une étude sur les erreurs systématiques des mesures d'émittance dû à la diffusion multiple et à l'effet de charge d'espace du faisceau,

ces deux phénomènes constituant les principales erreurs conduisant à une mauvaise reconstruction de l'émittance mesurée.

Le chapitre 6 quant à lui est dédié à l'étude mécanique de la fente de l'émittance mètre. Comme pour les fils des moniteurs de profils, la charge thermique sur la partie supportant la slit est importante. Ce chapitre décrit les études effectuées pour le choix des matériaux et de la géométrie des pièces mécaniques.

La troisième partie de la thèse, qui se résume au chapitre 7, est consacrée aux différents résultats expérimentaux obtenus dans la phase de test de la source de particule du LINAC4 ainsi que ceux obtenus lors d'une visite d'étude à SNS. Une partie de ce chapitre décrira la mise au point de l'instrumentation aux bancs test de la source, une autre présente l'effet de la diffusion multiple sur les mesures d'émittance à SNS et propose une mise à jour de l'instrument.

Le chapitre 8 constitue la dernière partie de cette thèse. Dans ce dernier chapitre, le lecteur pourra lire une étude préliminaire sur l'utilisation d'un faisceau laser pour la mesure d'émittance et de profil aux hautes énergies du linac.

Contents

1	Introduction	1
1.1	CERN accelerator complex	1
1.1.1	LHC injector chain	1
1.1.2	Linear accelerator at CERN	2
1.2	LINAC4	3
1.2.1	LINAC4 Layout	3
1.2.2	Beam instrumentation for LINAC4	4
2	Principles of accelerator beam dynamics	9
2.1	Basics of accelerator physics	9
2.2	Transverse beam emittance and linear motion	12
2.2.1	Linear motion	12
2.2.2	Transverse beam emittance	15
2.2.3	Courant-Snyder invariant in normalized phase space	16
2.2.4	Beam emittance	17
2.3	Space charge	21
2.3.1	Induced electrical and magnetic field	21
2.3.2	Space charge force	23
3	Particles interaction with matter	25
3.1	Energy loss by heavy particles	25
3.1.1	Bethe Bloch formula	25
3.1.2	Delta-rays	26
3.2	Energy loss of electrons and positrons	27
3.2.1	Ionization	27
3.2.2	Radiation loss	27
3.2.3	Radiation length	29
3.3	Multiple scattering	29
3.3.1	Backscattering	30
3.3.2	Range	31
3.4	Secondary emission	32

3.4.1	Generation of secondary electrons in solids	33
3.4.2	Diffusion process	34
3.4.3	Emission process	34
3.5	Electron stripping	37
4	SEM grids and wire scanner in LINAC4	39
4.1	Introduction	39
4.1.1	Secondary Emission Monitor (SEM grid)	39
4.1.2	Wire Beam Scanner (SEM mode)	42
4.1.3	Signal generation-Secondary emission of H^-	43
4.2	Thermal aspect	44
4.2.1	Temperature and cooling	44
4.2.2	Thermionic emission	45
4.2.3	Sublimation of a carbon wire	46
4.3	Test bench SEM grids	48
4.3.1	Resolution-SEM grid pitch	48
4.3.2	Test Bench SEM grids signal	49
4.3.3	Wire heating	52
4.4	WBS and SEM grid in the LINAC4 line	54
4.4.1	Signal	54
4.4.2	Expected current with polarized wires	55
4.4.3	Expected wire temperature	58
4.5	Chopper line Wire Beam Scanner	60
4.5.1	Wire heating	61
4.5.2	Expected current	62
4.6	Conclusion	64
5	Emittance measurement with a slit and grid system	67
5.1	Method	67
5.2	Effect of the slit design parameters on the emittance measurement accuracy	69
5.2.1	Slit aperture	69
5.2.2	Slit thickness	71
5.3	Profile Monitor resolution	71
5.4	Effect of the space charge on emittance reconstruction	73
5.4.1	Method	73
5.4.2	Phase space reconstruction with an infinite resolution monitor	74
5.4.3	Effect of the monitor resolution on the phase space reconstruction	77
5.5	Effect of scattering and stripping at the slit	80
5.5.1	Signal	80

5.5.2	Emittance reconstruction	81
5.5.3	Comparison proton/ H^-	83
5.5.4	Geometry aspect	83
5.6	Conclusions	83
6	SLIT design for the 3 and 12 MeV Test stand	85
6.1	Thermal effect on the 45 keV slit	86
6.2	FLUKA simulations	88
6.2.1	Material choice	89
6.2.2	Slit geometry	92
6.3	Finite Element Analysis	92
6.4	Final Slit Design	94
6.4.1	Slit geometry	96
6.4.2	Motorization and actuation system	97
6.4.3	Mechanical design.	98
6.5	Multiple scattering effects	99
6.5.1	Simulation model	99
6.5.2	Amount of scattered particles	100
6.5.3	Energy distribution of scattered particles	102
6.6	Conclusion	107
7	LINAC4 and SNS transverse emittance measurements	109
7.1	Beam emittance and beam profile measurement at the LINAC4 source front end	109
7.1.1	Commissioning of the LINAC4 LEBT	109
7.1.2	LINAC4 low energy emittance meter	110
7.1.3	Determination of emittance meter polarization setting	111
7.1.4	Emittance meter commissioning	113
7.1.5	Beam emittance and beam profile results	115
7.1.6	Energy spread and intensity measurements	121
7.2	Beam emittance measurement at the Spallation Neutron Source (SNS) MEBT	123
7.2.1	Description of the SNS emittance meter	123
7.2.2	Emittance measurement	124
7.2.3	Multiple scattering effects on the emittance reconstruction	128
7.3	Summary	137
8	Emittance measurement based on laser and H^0 detection	139
8.1	Laser wire-profile measurement.	140
8.1.1	Principle	140
8.1.2	SNS laser wire beam profile system	140

8.2	Application to LINAC4	143
8.2.1	Photo neutralization	144
8.2.2	Background	145
8.2.3	H^0 detection	151
8.3	Conclusion	156
9	Conclusions	159
A	Appendix: Effect of stripped electron on profile measurement	163
A.1	Introduction	163
A.2	Cross talk between two wires due backscattered electrons	164
A.3	Error on profile reconstruction with SEM grid and effect on the signal due to cross talk	168
A.3.1	Error on profile reconstruction	168
A.3.2	Effect on the signal	168
A.4	Profile reconstruction with Wire Scanners when accounting for stripped electrons scattering	172
A.4.1	FLUKA simulations of the SNS 1 GeV H^- beam case	173
A.5	Conclusion and outlook	174
	Bibliography	179

Chapter 1

Introduction

1.1 CERN accelerator complex

1.1.1 LHC injector chain

The Large Hadron Collider (LHC) is accommodated in the 27 km tunnel previously used for LEP. Four experimental areas are equipped for observing the proton beams collisions. Two of them consist of general purpose detectors, ATLAS and CMS. The other two are: a detector dedicated also to heavy ions, ALICE, and a detector specialized in the physics of the B-meson, LHCb. The locations of the four areas around the ring are depicted in Fig. 1.1. In addition, the experimental setup named TOTEM investigates the p-p total cross section, elastic scattering and diffraction processes.

LHC is supplied with protons by the injector chain also illustrated in Fig. 1.1. The protons are generated by a Duoplasmatron source from which they are extracted with a kinetic energy of 95 keV , accelerated by an RFQ up to 750 keV and injected in the Linac. The linac consists of a beam transport line of about 80 m along which the particles are accelerated to 50 MeV . The protons are then injected in the Proton Synchrotron Booster (PSB), a 157 m circumference complex capable of accelerating high intensity beams up to 1.4 GeV and composed of a stack of four separate rings with a common magnetic and radio frequency system. From the PSB the particles are transferred to the Proton Synchrotron (PS), a 628 m circumference ring (4 times the PS Booster ring), where they are accelerated to 26 GeV . Up to this point the accelerator complex is installed at ground level. A beam transport line connects the PS to the Super Proton Synchrotron (SPS), which has a circumference of 6.9 km and lays at about 50 m underground. In the SPS the beam energy increases from 26 to 450 GeV . The particle beams will be injected from the SPS to the LHC via two different transfer lines in order to establish two circulating beams in opposite directions. These two transfer lines

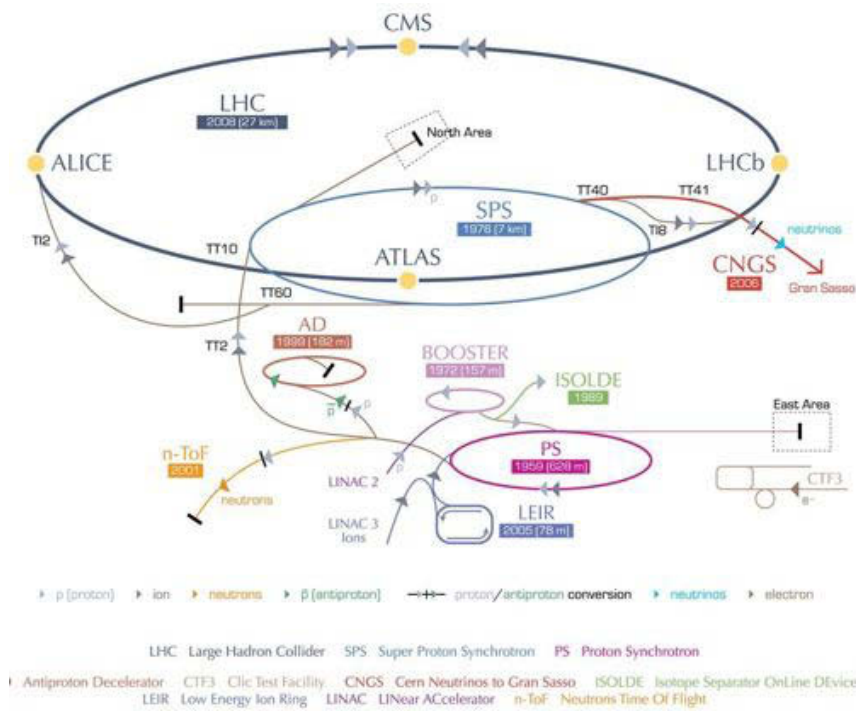


Figure 1.1: CERN accelerator complex.

provide the connection between the SPS tunnel and the LHC plane which lays between 80 and 150 m underground.

1.1.2 Linear accelerator at CERN

The linear accelerator (or LINAC) is the first vital stage of any hadron accelerator complex. The source and the LINAC determine the initial transverse and longitudinal beam emittances and define the beam quality for the next stages of acceleration. Moreover, the reliability of the injector has to be higher than any other stage of acceleration, a fault in a LINAC implies a shutdown of all other accelerator.

The first linear accelerator at CERN (LINAC1) started operating in 1959, injecting proton beams of a few mA at $50 MeV$ into the Proton Synchrotron (PS). The beam intensity of the LINAC1 was increase to $50 mA$ by the mid-70s after several hardware upgrades. In 1972, the limits of the LINAC1 capacities were reached with the commissioning of the Proton Synchrotron Booster (PSB). The preparation of the Super Proton Synchrotron (SPS) increased the demand for the LINAC, and led to the decision to build a new linear injector, the LINAC2. The new LINAC was designed with the same energy as the LINAC1, but with a

maximum current of 150 mA [1].

Since 1978, the LINAC2 is the injector of the CERN accelerator complex. During the last 33 years several upgrades took place. The most notable is the replacement in 1993 of the 750 keV Cocktoft-Walton pre-injector with a Radio Frequency Quadrupole (RFQ). This upgrade increased the beam current up to 180 mA. The reliability of the LINAC2 was constantly improved and a remarkable availability of 98.5 % average over the last 10 years was reached. Nevertheless, after more than 30 years of operation important vacuum leaks have been progressively appearing along the large acceleration tanks, requiring important repair interventions during the shut-down periods and being a constant cause of concern for future operation.

Considering the cost to maintain a reliable operation of LINAC2 today and in the future, and the many advantages of a new up-to-date H^- LINAC, it became clear after the successful running in of the heavy-ion LINAC3 in 1994, that the next priority for the LINAC team was to analyze the option of building a new LINAC injector for protons at CERN.

1.2 LINAC4

1.2.1 LINAC4 Layout

Fig. 1.2 shows the LINAC4 layout. The source will provide an H^- beam current of 80 mA at 45 keV at a repetition rate of 2 Hz and will be followed by the Low-Energy Beam Transport (LEBT) line. This line provides the beam matching from the source to the following Radio frequency Quadrupole (RFQ) and contains the diagnostics to monitor the source.

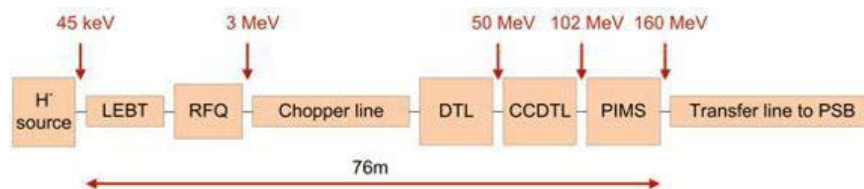


Figure 1.2: LINAC4 schematic layout.

The RFQ will perform the beam capture and bunching and will accelerate to the energy of 3MeV, followed by a Medium Energy Beam Transport (MEBT), or chopper line, containing the beam chopping system, which is an essential component of modern linear accelerators. The system consists of a fast traveling-wave electrostatic beam deflector followed by a dump, which is capable of stopping selected sequences of beam bunches (micro-pulses). The purpose of this operation is

to avoid the losses at high energy that occur when injecting LINAC bunches with typical frequencies in the hundreds of MHz range into ring buckets at frequencies in the MHz range and match the PSB frequency.

The following structure is the Drift Tube LINAC (DTL), that accelerates up to $50 MeV$. The present CERN proton LINAC (LINAC2) consists of three drift tube LINAC tanks accelerating the beam to $50 MeV$. LINAC2 has operated from the start at the design current of $150 mA$ and has been upgraded lately to $180 mA$, indicating the validity of the mechanical solutions adopted for construction and alignment of the drift tubes. For this reason, the basic mechanical design concept of LINAC2 has been retained for LINAC4, although applying the many improvements made possible by the technological advance in the last 25 years, in particular adopting modern and more reliable vacuum seals.

The next accelerating section will accelerate the beam to $102 MeV$ in RF structures called Cell-Coupled Drift Tube LINAC (CCDTL) . The beam is finally accelerated up to $160 MeV$ by a π -mode structure (PIMS) based on the LEP expertise. The beam dynamic has been optimized in order to reduce the losses between the different parts of the LINAC4. A new transfer line [2], and an upgrade of the exiting transfer line from LINAC2 to the PS booster and of the PSB for the charge exchange injection are also part of the project [3].

1.2.2 Beam instrumentation for LINAC4

Location	Energy [MeV]	BPM	BCT	SEM grids	WBS	BLM
diagn. Bench	3 and 12	3	2	3	-	-
LEBT	0.045	-	1	3	-	-
MEBT	3	-	2	-	2	1
DTL	3 to 50	2	-	2	-	2
CCDTL	50 to 102	7	1	4	2	4
PIMS	102 to 160	6	1	6	2	3

Table 1.1: LINAC 4 diagnostics overview.

Beam current and position

During commissioning, the beam current at the source exit will be monitored by a retractable Faraday cup, coupled to a $250 kHz$ sampling ADC readout allowing a $4 \mu s$ time resolution. Along the LINAC structure, the beam intensity will be continuously monitored by means of Beam Current Transformers (BCT) with a maximum sampling rate of $10 MHz$. The devices need a very good magnetic

shielding to avoid electro-magnetic coupling with the pulsed magnets that may be close to the detectors. The first two detectors have been already installed in the chopper line in the laboratory and successfully tested without beam, to verify the EM screening effectiveness.

A number of Beam Position Monitors (BPM) will measure:

- The absolute beam position .
- The relative beam current among monitors.
- The absolute beam current after calibration with the BCTs.
- The average beam energy via the time-of-flight between two monitors.

The systems are based on strip line detectors.

Transverse beam profile and emittance

A slit-grid system has been studied for measuring the emittance at the different stages where the diagnostics bench will be installed during commissioning. This System will be described in detail in Chapter 5 and 6. A Beam Halo monitor [4] will be used in the MEBT line at 3 *MeV* to detect unchopped or partially chopped bunches and to characterize the beam transverse tails. As shown in Table 1.1 and as will be discussed in Chapter 4, a number of SEM grid and Wire Beam Scanner (WBS) monitors will be installed at different LINAC4 locations. Those are retractable devices, permanently installed and will be used to measure beam profiles.

Longitudinal distribution and energy

The Bunch Shape Monitor (BSM) has been developed by A. Feshenko at INR in Russia [5]. It consists of a wire which can be inserted into the beam. Secondary electrons created through the interaction of the H^- beam with the wire are accelerated by a HV polarization voltage applied to the wire. The electrons pass through an input collimator and are deflected by an RF deflector whose RF pulse is in synchronism with the accelerating RF. The deflected electrons pass through an output collimator and are detected by an electron detector. The phase of the deflecting field can be shifted to scan the longitudinal intensity distribution of the incoming beam. The BSM will be used on the diagnostics test bench for the beam characterization at low energy and then permanently installed at the exit of the PIMS modules at 160 *MeV*.

Beam Losses

Beam Loss Monitoring (BLM) system will be included to observe beam losses between the 3 *MeV* and 160 *MeV* regions. It is foreseen to use LHC type monitors, i.e. ionization chambers with similar electronics. The exact detector number and location is currently under study [6]. This configuration is expected to provide multiple integration history windows between 2 μ s and 1.2 s, and a dynamic range covering the maximum losses (i.e. $4 \cdot 10^{13}$ ions) expected when the full 400 μ s pulse is injected. The BLM system will be included into the beam interlock system granting safe beam permits or block injections if the predefined thresholds get exceeded. Additionally, on some locations along the transfer to the PSB for observation and measurement reasons, e.g. during commissioning, faster monitors will be installed, for which Aluminum Cathode Electron Multiplier (ACEM) detectors are being considered.

Movable Test Bench

All machine elements from the source to the exit of the chopper line at 3 *MeV* will be installed and tested with beam in the laboratory where the source is presently commissioned. A movable diagnostics bench will be used to characterize the beam at the end of the RFQ and the chopper line at 3 *MeV*.

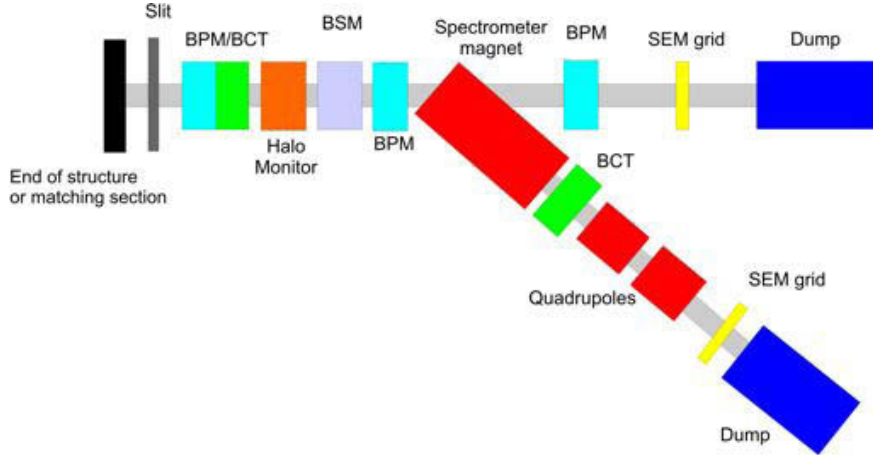


Figure 1.3: Layout of the movable diagnostic bench that will be used to commission all the accelerator element up to the DTL tank 1 at 12 *MeV*.

The movable test bench layout is shown in Fig. 1.3. During the machine installation in the tunnel, the bench will be re-used at the same two stages and then at the exit of the first DTL tank at 12 *MeV*. After this, the permanent LINAC4 instrumentation will be installed and used for both commissioning and

operation. Given the different beam parameter scenarios, shown later in Table 4.1, the LINAC4 diagnostics must cover a wide operational range. Details about the diagnostics functional specifications can be found in [7].

Chapter 2

Principles of accelerator beam dynamics

2.1 Basics of accelerator physics

In an accelerator, charged particles are accelerated and focused by magnetic and electrical fields. The machine elements are chosen in order to guide the beam along an ideal trajectory and reach the desired energy.

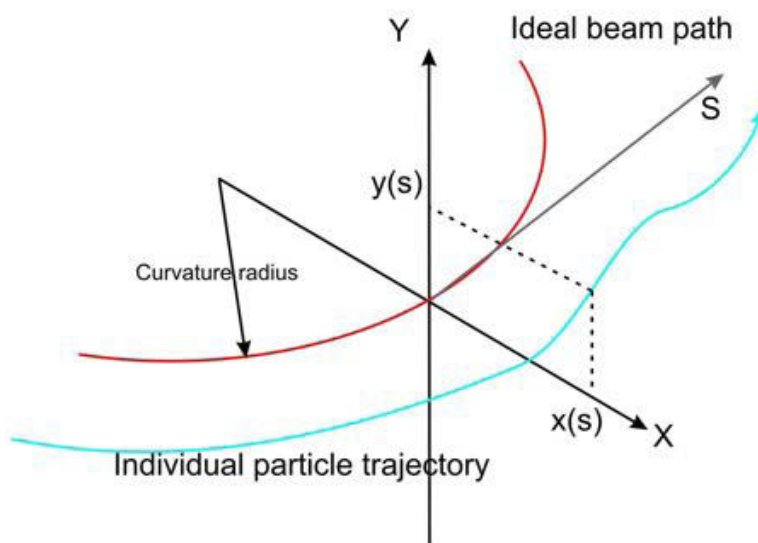


Figure 2.1: Coordinates system used in accelerator.

The following definitions refer to the coordinate system shown in Fig. 2.1 in which the longitudinal direction s is defined as the one following the beam refer-

ence path, while x and y define the transverse plane (orthogonal to the particle trajectory) and describe the particle deviations from the reference path. Locally, the design trajectory (reference orbit) has a curvature radius ρ . Such coordinate system moves following the reference path along sections which can be straight as well as curved and is therefore a curvilinear coordinate system. The trajectory of the reference particle is the one for which $x = 0$ and $y = 0$ for all s .

The scope of the accelerator design is the arrangement of the beam line elements with the aim of guiding the beam particles along the reference path and accelerates it to a desired energy. In practice it is not possible to keep all the particles on the same trajectory, the beam is populated by a number of particles performing small amplitude oscillations around the reference orbit.

The principal elements of particle accelerators are those that provide the beam guidance and focusing system. This is achieved by applying electromagnetic forces to the charged particles. Such forces are intended to accelerate, bend and direct the particles on the design trajectory, or to hold them close to it. The motion of a particle, with a charge e , in an electromagnetic field is described by the Lorentz law:

$$\frac{d\vec{p}}{dt} = e(\vec{E} + \vec{v} \times \vec{B}) \quad (2.1)$$

Where \vec{E} and \vec{B} are respectively the electric and magnetic fields and \vec{v} the particle velocity.

The particle is accelerated by longitudinal electrical fields, the bending and the focusing of the beam is provided by magnetic fields. A few magnet types are used in accelerators for focusing, in this thesis only the quadrupole magnets are describes, the dipole magnets are used to bend the beam, this type of magnet will be described quickly.

By design, the magnetic field of any type of magnet has a null component in the longitudinal direction, and can be expressed as:

$$\vec{B} = B_x \vec{i} + B_y \vec{j} \quad (2.2)$$

$$B_x = B_x(0, 0) + x \frac{\partial B_x}{\partial x} + y \frac{\partial B_x}{\partial y} \quad (2.3)$$

$$B_y = B_y(0, 0) + x \frac{\partial B_y}{\partial x} + y \frac{\partial B_y}{\partial y} \quad (2.4)$$

Where \vec{i} and \vec{j} are the unit vectors defining the transverse plane and the field components have been expanded to the first order terms.

Dipole magnets provide a constant field B_y in the magnet gap. The instantaneous radius of curvature ρ for a particle with momentum p , travelling in the

horizontal plane, comes from the equilibrium between the centrifugal and the centripetal Lorentz forces:

$$\rho = \frac{p}{eB_y} \quad (2.5)$$

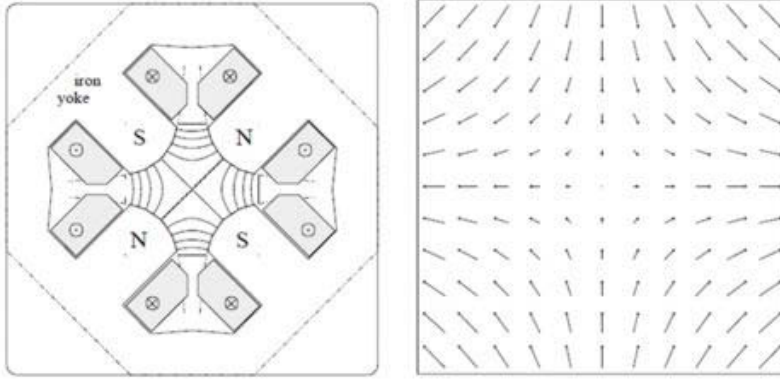


Figure 2.2: Cross section of a quadrupole magnet with indicated the magnetic field lines and Lorentz forces in vectorial representation. The force felt by a particle is increasing with the distance from the magnet center.

The Fig. 2.2 shows the cross section of a quadrupole magnet and the force applied to a particle passing at different locations in the magnet. A particle passing through the center of the quadrupole does not experience any force, the particle bending rises linearly with the distance from the center. Maxwell equation $\vec{\nabla} \times \vec{B} = 0$ always imposes

$$\frac{\partial B_y}{\partial x} = \frac{\partial B_x}{\partial y} \quad (2.6)$$

And due to the field pattern the Lorentz force is always focusing in one plane and defocusing in the other. Consequently quadrupoles with opposite polarities, alternated in an accelerator system, provide focusing in the two transverse directions. The most common structure in accelerator consists in the repetition of a basic cell called FODO. Each cell contains a horizontal focusing (F) quadrupole, a drift space (O), a horizontal defocusing (D) quadrupole and another drift space. The dipole magnets designed for the bending are inserted in between the quadrupoles.

Since they use quadrupoles, FODO cells are also defined as strong focusing structures: the restoring forces are as high as possible, but the magnetic elements cannot focus in the two planes at the same time. However simple considerations, involving geometrical optics, guarantee that if the drift spaces between quadrupoles

are small compared to the magnets focal lengths, each FODO cell produces a net focusing in both planes.

Higher order multipole magnets are also normally included in FODO cells. They are intended to correct beam perturbations which can be characterized only going beyond the approximation of transverse linear motion that will be treated in the next section.

2.2 Transverse beam emittance and linear motion

This section describes the transverse motion of the accelerated charged particles in a first order (linear) approximation. In this section, we suppose a circular accelerator without energy change like a storage ring, the equation and the results described in this part can be applied to the other type of accelerator. An additional assumption is the absence of coupling of the two transverse planes: the motion in the horizontal plane is not affected by the one in the vertical [8].

2.2.1 Linear motion

The accelerator magnetic elements are designed to guide and focus the beam along the reference circular orbit. However, particles which at the time t_0 have non zero transverse coordinates (x_0, y_0) and slope (x'_0, y'_0) start to perform oscillations in the horizontal (bending) and vertical planes around the reference orbit. Such oscillations are called Betatron Oscillations for historical reasons and depend on the magnetic fields applied in the ring.

The equation of motion derives from Lorentz law and reads:

$$\frac{d\vec{p}}{dt} = e\vec{v} \times \vec{B} \quad (2.7)$$

The magnetic field \vec{B} can be defined and expanded with horizontal (B_x) and vertical (B_y) components, while as a first approximation the field component along the curvilinear coordinate s is null. Developing the vector product of Eq. 2.5, leads to the expression of the motion in the two transverse directions:

$$x'' + \left[\frac{1}{\rho(s)^2} + \frac{1}{(B\rho)} \frac{\partial B_y(s)}{\partial x} \right] x = 0 \quad (2.8)$$

$$y'' + \frac{1}{(B\rho)} \frac{\partial B_y(s)}{\partial x} y = 0 \quad (2.9)$$

$B\rho$ is equal to the ratio of momentum to charge p/e and is called magnetic rigidity. The two equations differ for the term $1/\rho(s)^2$ which is related to the centripetal force in the radial direction. The gradient terms result equal due to the curl condition and their meaning can be explained as follows:

Considering a particle passing through a magnetic field with gradient $B' = \partial B_y / \partial x$ over a distance Δs , the slope of the particles trajectory (in a circular machine with radius r) $x' = dx/ds$ changes by an amount such that:

$$\frac{\Delta x'}{\Delta s} = -\frac{\beta'(s)}{B\rho} x \quad (2.10)$$

In fact, with the limit $\Delta s \rightarrow 0$, the previous equation becomes a second order differential equation:

$$x'' + \frac{\beta'(s)}{B\rho} x = 0 \quad (2.11)$$

Which perfectly reproduces the equation of motion in the vertical direction and the one in the horizontal direction without the centripetal term. The gradient term depends on the momentum and is also defined as the *normalized quadrupole strength*.

$$k(s) = \frac{1}{(B\rho)} \frac{\partial B_y(s)}{\partial x} = \frac{e}{p} \frac{\partial B_y(s)}{\partial x} = 0 \quad (2.12)$$

The equation x and y can be written as:

$$x'' - \left(k(s)x - \frac{1}{\rho^2}\right) = 0 \quad (2.13)$$

$$y'' + k(s)y = 0 \quad (2.14)$$

In general, a new parameter $K(s)$ is defined and the one equation can be used for the both plane:

$$u'' + K(s)u = 0 \quad (2.15)$$

For the horizontal plane:

$$K(s) = -\left(k(s)x - \frac{1}{\rho^2}\right) \quad (2.16)$$

And for the vertical plane:

$$K(s) = k(s) \quad (2.17)$$

The obtained second order differential equation resembles the one of a harmonic oscillator, with the only difference of having the "spring constant" K that depends on the variable s . Within each component of the accelerator, K can be considered constant, and therefore the harmonic oscillator solutions can be used to describe the particle motion through each single component. The solutions can be divided in three cases which depend on the value of K . For $K = 0$ the evolution of $x(s)$ and $x'(s)$ along an element of length L can be written in matrix formalism:

$$\begin{bmatrix} x(s) \\ x'(s) \end{bmatrix}_f = \begin{bmatrix} 1 & L \\ 0 & 1 \end{bmatrix} \begin{bmatrix} x(s) \\ x'(s) \end{bmatrix}_i \quad (2.18)$$

And reflects a passage of the particle through a drift space of length L . For $K > 0$.

$$\begin{bmatrix} x(s) \\ x'(s) \end{bmatrix}_f = \begin{bmatrix} \cos(\sqrt{K}L) & \frac{1}{\sqrt{K}}\sin(\sqrt{K}L) \\ -\sqrt{K}\sin(\sqrt{K}L) & \cos(\sqrt{K}L) \end{bmatrix} \begin{bmatrix} x(s) \\ x'(s) \end{bmatrix}_i \quad (2.19)$$

If $K < 0$, the solution is

$$\begin{bmatrix} x(s) \\ x'(s) \end{bmatrix}_f = \begin{bmatrix} \cosh(\sqrt{K}L) & \frac{1}{\sqrt{K}}\sinh(\sqrt{K}L) \\ -\sqrt{K}\sinh(\sqrt{K}L) & \cosh(\sqrt{K}L) \end{bmatrix} \begin{bmatrix} x(s) \\ x'(s) \end{bmatrix}_i \quad (2.20)$$

Every accelerator component has its characteristic matrix M_j and the transport of a particle through N elements is described by a matrix $M = M_N \cdot M_{N-1} \cdot \dots \cdot M_1$. When M represents the transport along one accelerator turn, M^n describes the particle motion after n revolutions. For a stable motion of a particle with initial conditions x_0 and x'_0 the quantity:

$$M^n \begin{bmatrix} x_0 \\ x'_0 \end{bmatrix} \quad (2.21)$$

Must remain finite for an arbitrary large value of n . It can be proved, by calculating the matrix Eigen values, that the stability condition results:

$$-2 < \text{trace}(M) < 2 \quad (2.22)$$

Considering a FODO cell, the elements of M , depending of the values of $K(s)$, reflect the bending and focusing strengths and the stability criteria requires:

$$\left| \frac{d}{2f} \right| \leq 1 \quad (2.23)$$

Where d is the distance between a focusing and a defocusing magnet, both with focal length f . A more rigorous solution of the equation of motion can be deduced observing that Eq. 2.14 has the form of Hills equation which has been extensively studied during the nineteenth century. For K everywhere a positive constant the solution would become the one of a harmonic oscillator which can now be expressed as:

$$x(s) = a_1 \cos(\sqrt{K}s) + a_2 \sin(\sqrt{K}s) \quad (2.24)$$

where a_1 and a_2 are determined by the boundary conditions.

2.2.2 Transverse beam emittance

Only a single particle has been considered, the particles distribution is generally described by a density function in a six dimension space:

$$\psi = \Phi(x, p_x, y, p_y, s, p) \quad (2.25)$$

where, x, y and s are the particle coordinates previously defined, p_x and p_y the components of the particle momentum in such a coordinate system and E the particle energy. In systems with a constant energy like storage ring, the transverse momenta are usually replaced by the slope of particles trajectory (x' and y').

In this case, the coupling between the two transverse planes and between each transverse plane and the longitudinal one has been neglected. In this case the six dimensional space can be factorized into three independent subspaces (x, x'), (y, y') and (s, p), that are often called trace spaces, even if in the following they will be referred as phase spaces. The notions that will be figured out for the horizontal plane apply also to the vertical.

The general solution of Hill's equation is

$$x(s) = A\sqrt{\beta(s)}\cos(\Psi(s) + \Psi_0) \quad (2.26)$$

Where A and Ψ_0 are integration constant determined by initials conditions. $\beta(s)$ is a periodic function given by focusing properties of the lattice (i.e. quadrupoles).

From Eq. 2.26, the slope of the trajectory can be defined as:

$$\begin{aligned} x'(s) &= \frac{dx(s)}{ds} = -\frac{A}{\sqrt{\beta(s)}}\sin\theta(s) + A\cos\theta(s)\frac{1}{2\sqrt{\beta(s)}}\frac{d\beta(s)}{ds} \\ &= -\frac{A}{\sqrt{\beta(s)}}[\sin\theta(s) + \alpha(s)\cos\theta(s)] \end{aligned} \quad (2.27)$$

With:

$$\alpha(s) = -\frac{1}{2} \frac{d\beta(s)}{ds} \quad (2.28)$$

$$\gamma(s) = \frac{1 + \alpha^2(s)}{\beta(s)} \quad (2.29)$$

α, β and γ are called *Courant-Snyder parameters*.

From Eq. 2.26 and 2.27, it is interesting to introduce $x(s)$ and $x'(s)$ in the following polynomial expression:

$$\begin{aligned} \gamma x^2 + 2\alpha x x' + \beta x'^2 &= A^2 \gamma \beta \cos^2 \theta - 2A^2 \alpha [\sin \theta \cos \theta + \alpha \cos^2 \theta] \\ &\quad + A^2 [x \sin^2 \theta + \alpha^2 \cos^2 \theta + 2\alpha \sin \theta \cos \theta] \\ &= A^2 [\cos^2 \theta (\gamma \beta - \alpha^2) + \sin \theta \cos \theta (2\alpha - 2\alpha) + \sin^2 \theta] \\ &= A^2 \end{aligned} \quad (2.30)$$

In which all the variables x , x' , α , β , γ and θ are functions of s although not indicated for simplicity. The quantity $\gamma x^2 + 2\alpha x x' + \beta x'^2$ is constant along a particular particle trajectory and is referred to as *Courant-Snyder invariant*.

A^2 is referred as the *emittance* of a single particle following its individual trajectory,

$$\varepsilon = A^2 = \frac{\text{ellipse area}}{\pi} \quad (2.31)$$

The parameters of the ellipse are determined by the lattice functions α, β and γ at the location s_0 , and by the emittance ε , as depicted in Fig. 2.3. The ellipse in phase space may assume different orientations in different locations around the ring, but the ellipse area (i.e. the particle emittance) remains constant.

2.2.3 Courant-Snyder invariant in normalized phase space

Sometimes it is useful to apply a change of coordinates in phase space from (x, x') to $(x, \alpha x + \beta x') = (x, z)$. In this new coordinate system, which is often named normalized, the ellipse in phase space becomes a circle, and in polar coordinates the radial variable is $r^2 = x^2 + z^2 = x^2 + (\alpha x + \beta x')^2$. The Courant-Snyder invariant $\gamma x^2 + 2\alpha x x' + \beta x'^2 = A^2$, becomes:

$$\frac{x^2}{\beta} + \frac{z^2}{\beta} = \frac{r^2}{\beta} = A^2 \quad (2.32)$$

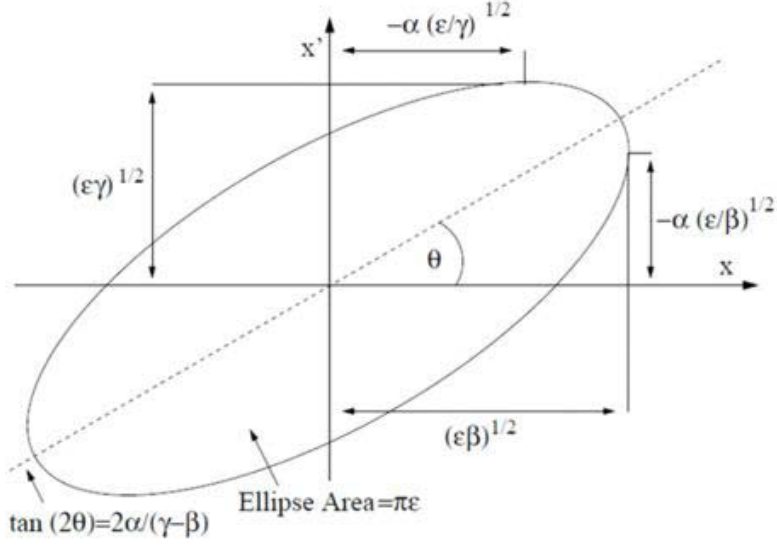


Figure 2.3: Courant Snyder invariant in normalized phase space.

2.2.4 Beam emittance

Considering the particles centered around the reference orbit, for any distribution of the particles, it is possible to define a region in phase space occupied by the particles.

It is convenient to change the coordinates system to two axis X, X' centered on the distribution barycenter and orientated in order to minimize the sum of the square distances of each point from each axis. Such coordinate system is shown in Fig. 2.4. If θ is the rotation angle of X with respect to x , the distance of the point $P(x_i, x_i)$ from the axis X is:

$$d_i = |x'_i \cos\theta - x_i \sin\theta| \quad (2.33)$$

Minimizing the distance d defines the rotation angle θ :

$$\frac{d}{d\theta} \left(\frac{1}{N} \sum_{i=1}^N d_i^2 \right) = \frac{d}{d\theta} \sigma_x^2 = 0 \quad (2.34)$$

This results in:

$$\tan 2\theta = \frac{2\bar{x}\bar{x}'}{\bar{x}^2 - \bar{x}'^2} \quad (2.35)$$

Where:

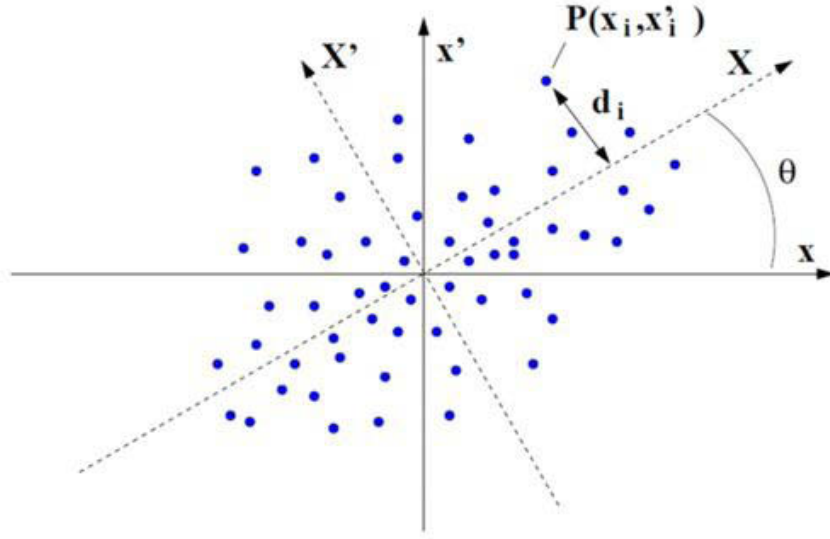


Figure 2.4: Particles distribution in phase space. The Cartesian axes X, X' are chosen in order to minimize the sum of the square distances between the points and the axis X .

$$\bar{x}^2 = \frac{1}{N} \sum_{i=1}^N x_i^2 \quad (2.36)$$

$$\bar{x'^2} = \frac{1}{N} \sum_{i=1}^N x_i'^2 \quad (2.37)$$

$$\bar{xx}'^2 = \frac{1}{N} \sum_{i=1}^N xx_i'^2 \quad (2.38)$$

are the central second-order moments of the distribution, being $x = x' = 0$. The value of θ also defines the orientation of X' to $\theta + 90^\circ$. Referring to the new Cartesian system, the variances of the particles distances from X and X' result:

$$\sigma_X^2 = \frac{1}{2}(\bar{x}^2 + \bar{x'^2} + \frac{2\bar{xx}'}{\sin 2\theta}) \quad (2.39)$$

$$\sigma_{X'}^2 = \frac{1}{2}(\bar{x}^2 + \bar{x'^2} - \frac{2\bar{xx}'}{\sin 2\theta}) \quad (2.40)$$

The variances of the particles distribution in phase space can be assigned as semi-axes of the beam envelope ellipse. The equation of such ellipse is:

$$\frac{X^2}{\sigma_X^2} + \frac{X'^2}{\sigma_{X'}^2} = 1 \quad (2.41)$$

and its area results $A = \pi\sigma_X\sigma_{X'}$. Hence it is possible to define the beam emittance or r.m.s. emittance as the area of this ellipse divided by π ,

$$\varepsilon_{rms} = \frac{A}{\pi} = \sigma_X\sigma_{X'} \quad (2.42)$$

By a rotation of θ , the ellipse can be expressed with respect to the axes x, x'

$$x^2\sigma_{x'}^2 - 2xx'\sigma_x\sigma_{x'} + x'^2\sigma_x^2 = \sigma_x^2\sigma_{x'}^2 \quad (2.43)$$

where σ_x and $\sigma_{x'}$ are the standard deviations and $r = \frac{xx'}{\sqrt{x^2x'^2}}$ is the correlation coefficient. Using the parametrization:

$$\sigma_x = \sqrt{\beta\varepsilon_{rms}} \quad (2.44)$$

$$\sigma_{x'} = \sqrt{\gamma\varepsilon_{rms}} \quad (2.45)$$

$$4r\sigma_x\sigma_{x'} = -\alpha\varepsilon_{rms} \quad (2.46)$$

This result explains the concept of beam emittance, as the area of the ellipse with contour defined by the particles dispersion in phase space. According to this definition, from the variance with respect to x , one can directly calculate the beam emittance:

$$\varepsilon_{rms} = \frac{\sigma_x^2}{\beta} \quad (2.47)$$

Where, as already seen, β is the betatron function at the location s . Along the ring, in order to respect the Courant-Snyder invariant, β and σ_x vary in order to keep the emittance constant. This remarkable outcome can also be explained by stating that [9] *"in a linear lattice, the envelope ellipse at a position s_1 is mapped into the envelope ellipse of the new particle distribution at another position s_2 . Moreover, any ellipse homothetic to the envelope ellipse is mapped into an ellipse homothetic to the new envelope ellipse."* In case of a Gaussian distribution, the standard deviation of the distribution coincides with the Gaussian width σ . Even if the particle distributions inside the bunch can be far from being Gaussian at the particles source, after acceleration to collision energies the normal function is a very good approximation, due to the central limit theorem of probability and

the diminished importance of space charge effects. From now on, only Gaussian beams will be considered, with their RMS emittance expressed as

$$\varepsilon = \frac{\sigma_x^2}{\beta} \quad (2.48)$$

σ_x is also called beam size. This definition of beam emittance relies on the contour ellipse drawn at one σ_x and one $\sigma_{x'}$ of the distribution in phase space. It can be proven that this corresponds to the ellipse containing 39 % of the particles populating the distribution. However this definition is not the only one used to represent the particles transverse distribution. Table 2.1 resumes the fraction F of a Gaussian beam associated with various definitions of emittance.

ε	F(%)
σ^2/β	15
$\pi\sigma^2/\beta$	39
$4\pi\sigma^2/\beta$	81
$6\pi\sigma^2/\beta$	95

Table 2.1: Fraction F of particles in a Gaussian beam, associated with different definitions of emittance.

The previous considerations have been done assuming a constant energy for the beam. This case is only for a ring. In a linac, the beam is constantly accelerate, the beam energy changes everywhere except in a few and short locations (drift space or transfer line). Fig. 2.5 shows the effect of acceleration on the momentum of the particle.

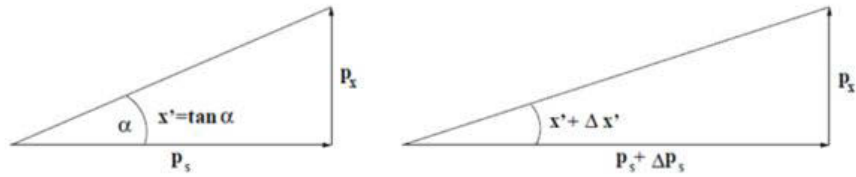


Figure 2.5: Longitudinal momentum increase during acceleration. The transverse momenta remain unchanged.

The transverse momentum remains constant, so the beam emittance is reduced with acceleration. In order to have a constant variable for all the energy of an accelerator, a normalized emittance is defined like:

$$\varepsilon_{norm} = \beta_{rel} \gamma_{rel} \varepsilon \quad (2.49)$$

Where β_{rel} and γ_{rel} are respectively the velocity of the particle divided by the light velocity and the Lorentz factor. In the following part of this thesis, only the normalized emittance has been considered.

2.3 Space charge

Inside a bunch, the distance between the particles is low, the charge of the particles has the same polarity and the Coulomb force lead the particles to push away from each other. The effect of the space charge is equivalent to a defocusing force in the both transverse planes. The strength of the force depends on the beam parameters (intensity, particle type energy and beam size), the field generated by the beam itself can be derivate from these parameters [10].

2.3.1 Induced electrical and magnetic field

In order to determinate the fields, a continuous beam has been considered, with a linear charge λ or a volume charge $\rho(x, y)$. The potential of this distribution of charge is defined by Poisson's equation:

$$\Delta V = -4\pi\rho(x, y) \quad (2.50)$$

Where ρ is finite within the beam and vanishes outside, the same consideration can be applied for the magnetic potential vector and:

$$\Delta \vec{A} = -1\pi\frac{\vec{v}}{c}\rho(x, y) \quad (2.51)$$

In an accelerator, the beam velocity, in a first approximation, has only one component along the longitudinal axis, so:

$$\begin{bmatrix} 0 \\ 0 \\ A_z \end{bmatrix} \quad (2.52)$$

The beam has generally an elliptical cross section, if we assume a constant charge density, the electrical potential can be written as :

$$V(x, y) = -2\pi\rho\frac{ab}{a+b}\left[\frac{x^2}{a} + \frac{y^2}{b}\right] \quad (2.53)$$

The longitudinal component of the magnetic potential vector can be written as :

$$A_z(x, y) = -2\pi\rho\frac{v}{c}\frac{ab}{a+b}\left[\frac{x^2}{a} + \frac{y^2}{b}\right] \quad (2.54)$$

Where a and b are respectively the horizontal and vertical half axis of the ellipse and v the beam velocity. From these two expressions, the electric and magnetic field can be derived from Maxwell's Law:

$$\vec{E} = -\nabla V \quad (2.55)$$

$$\vec{B} = \nabla \times \vec{A} \quad (2.56)$$

The horizontal and vertical component of the electrical field are written as

$$E_x = \frac{4e\lambda}{a(a+b)}x \quad (2.57)$$

$$E_y = \frac{4e\lambda}{b(a+b)}y \quad (2.58)$$

And for the magnetic field

$$B_y = -\frac{4e\lambda\beta}{a(a+b)}x \quad (2.59)$$

$$B_x = \frac{4e\lambda\beta}{b(a+b)}y \quad (2.60)$$

With $\beta = v/c$ and $\lambda = \pi ab\rho(x, y)$, the linear charge density.

The transverse charge distribution of particles is not constant in an accelerator, but with a good result, this distribution can be approximated with a Gaussian shape. The charge distribution of such a shape is:

$$\rho(x, y) = \frac{\lambda}{2\pi\sigma_x\sigma_y}e^{\frac{-x^2}{2\sigma_x^2} + \frac{-y^2}{2\sigma_y^2}} \quad (2.61)$$

The potential for a transverse bigaussian charge distribution can be expressed by:

$$V(x, y) = -e\lambda \int_0^\infty \frac{1 - e^{\frac{-x^2}{2\sigma_x^2+t} + \frac{-y^2}{2\sigma_y^2+t}}}{\sqrt{(\sigma_x^2+t)(\sigma_y^2+t)}} dt \quad (2.62)$$

The vertical component of the electric field is derived from this expression:

$$E_y = -\frac{\partial V(x, y)}{\partial y} = ey\lambda \int_0^\infty \frac{e^{\frac{-x^2}{2\sigma_x^2+t} + \frac{-y^2}{2\sigma_y^2+t}}}{(\sigma_y^2 + t)\sqrt{(\sigma_x^2 + t)(\sigma_y^2 + t)}} dt \quad (2.63)$$

A solution can be found if it restrict to a symmetry plane ($x = 0$ or $y = 0$) and for small amplitudes ($y \ll \sigma_y, x \ll \sigma_x$). These assumptions are appropriate for most space charge effect, the potential can be written as:

$$V(x = 0, y \ll \sigma_y) = -\frac{\lambda}{\sigma_y(\sigma_x + \sigma_y)} y^2 \quad (2.64)$$

For symmetrical reasons, a similar expression can be derived for the horizontal plane. The electrical field derivates from the potential are:

$$E_x = \frac{2\lambda}{\sigma_x(\sigma_x + \sigma_y)} x \quad (2.65)$$

$$E_y = \frac{2\lambda}{\sigma_y(\sigma_x + \sigma_y)} y \quad (2.66)$$

For the magnetic fields, the expression can be written as :

$$B_x = \frac{-2\lambda\beta}{\sigma_y(\sigma_x + \sigma_y)} y \quad (2.67)$$

$$B_y = \frac{2\lambda\beta}{\sigma_x(\sigma_x + \sigma_y)} x \quad (2.68)$$

The fields are null in the center of the beam and increase linearly with the distance.

2.3.2 Space charge force

The strength of the space charge force can be calculated from this field expression with the Lorentz law:

$$\vec{F} = e\vec{E} + \frac{e}{c}[\vec{v} \times \vec{B}] \quad (2.69)$$

In the horizontal plane:

$$F_x = e(1 - \beta^2)E_x = \frac{eE_x}{\gamma^2} = \frac{e}{\gamma^2} \frac{2\lambda}{\sigma_x(\sigma_x + \sigma_y)} x \quad (2.70)$$

And in vertical plane:

$$F_y = e(1 - \beta^2)E_x = \frac{eE_y}{\gamma^2} = \frac{e}{\gamma^2} \frac{2\lambda}{\sigma_y(\sigma_x + \sigma_y)} y \quad (2.71)$$

The force is proportional to the beam particle density and as the invert of the beam size; the effect is important at low energy and decreases with $1/\gamma^2$. The density of particle per unit of volume has a strong influence on the force; the strength is higher when the beam is compressed in real space. In an accelerator, generally at low energy, a part of the focusing system is used to counteract the effect of the space charge. If this effect is not taking in account, it leads to an emittance increase. Space charge is the limiting factor for the minimum emittance that can be produced by a particle source or an accelerator.

Chapter 3

Particles interaction with matter

3.1 Energy loss by heavy particles

The electronic interactions of fast charged particles with speed $v = \beta c$ traversing matter occur in single collisions with energy losses leading to ionization and atomic (or collective) excitation. Most frequently the energy losses are small (for 90 % of all collisions the energy losses are less than 100 eV). The interaction with a nucleus is less frequent and can be neglected at low energy. The projectile particle transfers a part of its energy to the electrons of the medium. These electrons can be excited to higher energy levels, or gain enough energy to escape the potential of the atom and therefore ionize it. For an elastic collision, the maximum transfer in a single interaction can be written as:

$$T_{max} = \frac{2m_e c^2 \beta^2 \gamma^2}{1 + \frac{\gamma m_e c^2}{M c^2} + (\frac{m_e c^2}{M c^2})^2} \quad (3.1)$$

Where m_e is the mass of the electron, M the mass of the particle, γ, β the relativistic parameters [11].

3.1.1 Bethe Bloch formula

The stopping power of moderately relativistic ($\beta\gamma < 1000$) charged heavy particles is well-described by the *Bethe-Bloch* equation:

$$-\frac{dE}{dx} = K z_e^2 \frac{Z}{A} \frac{1}{\beta^2} \left[\frac{1}{2} \ln \left(\frac{2m_e c^2 \beta^2 \gamma^2 T_{max}}{I^2} \right) - \beta^2 - \frac{\delta(\beta\gamma)}{2} \right] \quad (3.2)$$

where I is the mean excitation energy for the given absorber, Z and A the atomic number and mass number of the absorber, z_e is the charge of the projectile, K/A is $0.307 MeV g^{-1}.cm^2$ and $\delta(\beta\gamma)$ is a parameterized density correction factor

necessary for highly relativistic particles, units are $MeV.cm^2.g^{-1}$ [11]. I varies from few eV for low Z to hundreds of e for high Z materials and can be calculated with an empirical formula:

$$I(eV) = 16Z^{0.9} \quad (3.3)$$

For energy ranges such that $0.1 < \beta\gamma < 1000$ and for intermediate- Z materials Eq. 3.3 describes the mean rate of energy loss with an accuracy of a few %. At the lower limit the projectile velocities become comparable to the atomic electron velocities and at the upper limit radiative effects begin to be important. As example, Fig. 3.1 shows the stopping power of muons on copper for a $\beta\gamma$ range between 0.001 and 10^6 .

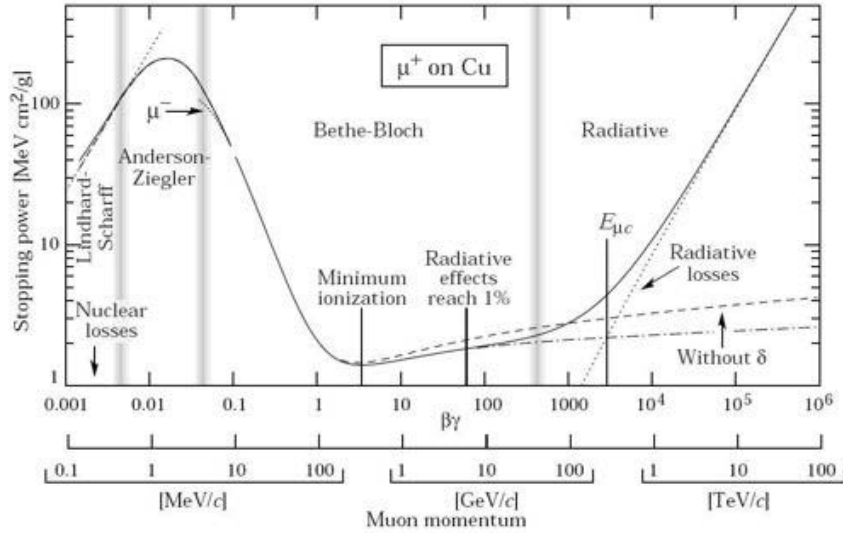


Figure 3.1: Stopping power for muons on copper as function of the particle momentum. The solid curve represents the total stopping power. (from [11])

3.1.2 Delta-rays

If the energy transferred to electrons is above few hundred eV (up to T_{max}), the particles can create secondary ionization. These high energy (compare to the electrons produce by ionization) electrons are called δ -rays. The distribution of δ -ray with kinetic energy $I \ll T < T_{max}$ is given by the formula:

$$\frac{d^2 N}{dT dx} = \frac{1}{2} K z^2 \frac{Z}{A} \frac{1}{\beta^2} \frac{F(T)}{T^2} \quad (3.4)$$

The factor F is spin- dependent, but is about unity for $T \ll T_{max}$

Depending on the energy of the primary particles, the δ electrons can reach an energy above 1 *keV*. Secondary emission electrons are generated when the electron energy is enough to escape the material (see section 3.3.2).

3.2 Energy loss of electrons and positrons

For electrons, quantum mechanics shows that the maximum energy transfer is $E/2$, where E is the energy of the incident electron. The Bethe Bloch formula as expressed in Fig. 3.1 is not valid anymore. As electrons traverse matter, due to the low mass, their trajectory can be affected by Coulomb interactions and the energy loss per unit length is difficult to determine. In general below few *MeV* the losses by ionization are the dominant process, while at high energy, the energy loss process is dominated by Bremsstrahlung.

3.2.1 Ionization

The two processes leading to energy loss by ionization are Moeller scattering [12] and Mott scattering [13]. The Moeller scattering is the name given to electron-electron scattering in Quantum Field Theory. The reaction can be written as:

$$e^-e^- \rightarrow e^-e^-$$

Mott Scattering is similar to Rutherford scattering and describes the interaction electrons-nucleus. The formalism of the Bhabha scattering is used when the incident particle is a positron [14]. From the cross section of these two processes the Bethe-Bloch formula can be modified according to:

$$-\frac{dE}{dx} = \frac{K'}{2} \frac{Z}{A\beta^2} \ln\left(\frac{m_e c^2 \beta^2 E}{2I^2(1-\beta^2)}\right) \quad (3.5)$$

With:

$$K' = \frac{1}{4\pi\epsilon_0} \frac{e^4}{m_e c^2} N_a$$

and N_a the Avogadro number.

3.2.2 Radiation loss

Electromagnetic radiation is emitted every time the particle velocity vector changes. Inside matter, the trajectory of electrons (or positrons) is deviated by

the fields of the nucleus and the radiation in this case is called Bremsstrahlung. The loss by radiation increases with the z of the material. The critical energy E_c is sometimes defined as the energy at which the two loss rates (ionization and Bremsstrahlung) are equal. An empirical formula gives E_c in MeV :

$$E_c = \frac{800}{z + 1.2} \quad (3.6)$$

For example, the critical energy for lead is around $10 MeV$. The Bremsstrahlung cross section for a particle with a mass m and a velocity $v = \beta c$ is given by:

$$\frac{d\sigma}{dk} \approx 5\alpha z^4 Z^4 \left(\frac{m_e c^2}{m c^2 \beta}\right)^2 \frac{r_e^2}{k} \ln\left(\frac{m c^2 \beta^2 \gamma^2}{k}\right) \quad (3.7)$$

Where k is the kinetic energy of the emitted photon, and r_e the classical radius of the electron ($r_e = \frac{1}{4\pi\epsilon_0} \frac{e^2}{m_e c^2}$) and α the fine-structure constant. The cross section is proportional to the square of the ratio of the electron mass over the particle mass. For electrons this ratio equals 1, for protons with the same $\beta\gamma$, the ratio is about 10^{-6} . Therefore radiation losses are negligible for proton and heavier particles.

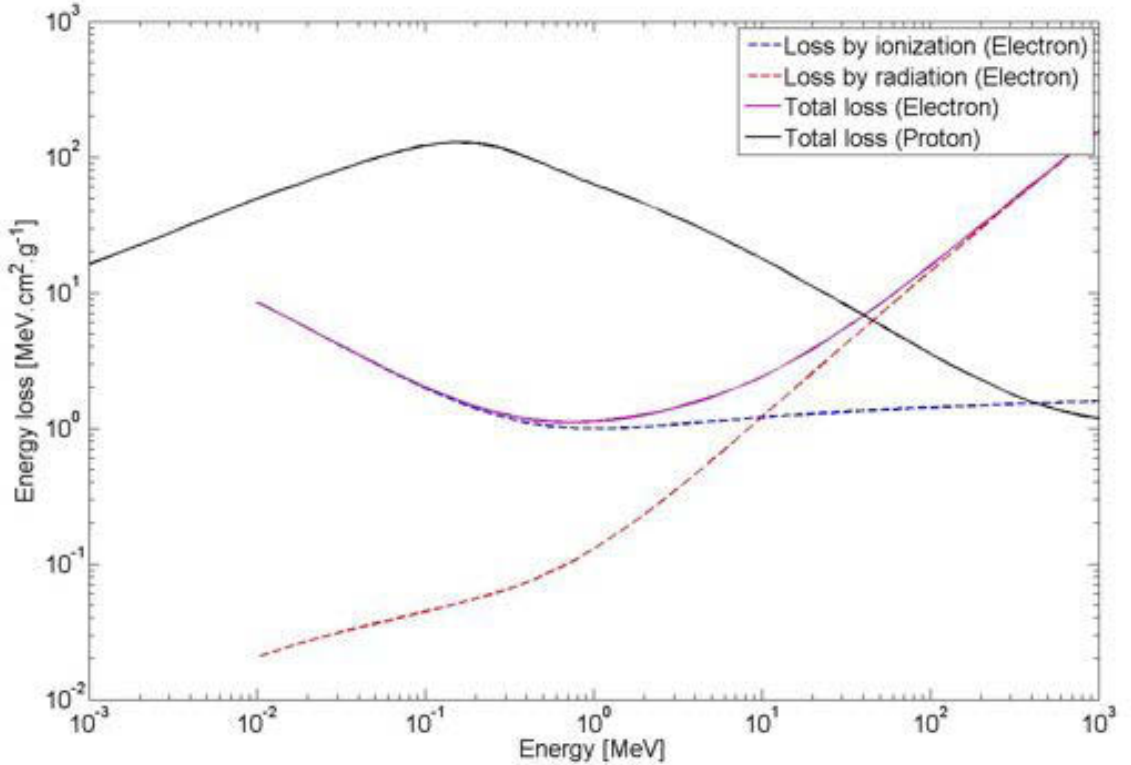


Figure 3.2: Energy losses for proton and electron in Lead [11].

Fig. 3.2 shows the energy loss by electrons and protons in lead. For electrons above 10 MeV the rate of radiation loss increases quickly, and is the dominant effect on energy loss.

3.2.3 Radiation length

As discussed above, high-energy electrons predominantly lose energy in matter by Bremsstrahlung. The radiation length X_0 , usually measured in $g.cm^{-2}$ is the mean distance over which a high-energy electron loses all but $1/e$ of its energy by Bremsstrahlung. For a given energy, the loss by radiation is proportional to the atomic number of the material. The radiation length is a property of the matter. An approximation of the value of X_0 can be calculated with the formula:

$$X_0 = \frac{716.4A}{Z(Z+1)\ln(\frac{287}{\sqrt{Z}})} \quad (3.8)$$

3.3 Multiple scattering

Charged particles traversing a material are elastically scattered by the time-averaged potential created by the atomic nucleus of the material and its associated electrons. This process is well described by the Coulomb scattering theory [15]. Each interaction is described by the Rutherford scattering cross section formula, written as:

$$\frac{d\sigma}{d\Omega} = \frac{z^2 Z^2 r_e^2}{4 \sin^4(\frac{\theta}{2})} \left(\frac{m_e c^2}{\beta p}\right)^2 \quad (3.9)$$

Where z and Z are the charge of the incident particle and the charge of the nucleus respectively, θ is the angle of the trajectory deviation, p is the momentum of the particle. $\frac{d\sigma}{d\Omega}$ represents the area provided by a target particle for scattering an incident particle into the solid angle $d\Omega$.

The $\frac{1}{\sin^4 \frac{\theta}{2}}$ dependency shows that the mean angle of deviation is null and most of the deviation are small. The energy transfer is also small if the mass of the particle is small compared to the mass of the nucleus. As a consequence, the trajectory of the particle is not straight and the sum of the deviation in matter implies a net deviation.

If the particles pass through a thin layer, the probability of interaction is low. Assuming only one Coulomb interaction in the matter, the angular distribution is given by the Rutherford formula and the process is called single scattering.

For thicker layers, the probability of multiple interaction increases, a statistical method can be applied for a number of interactions > 20 . The Moliere theory gives

good results for particles heavier than electrons and if the angle θ is lower than 30° [16]. At small angles, the angular distribution is similar to a Gaussian, while a tail appears at large angles and is well reconstructed by the Rutherford formula for a single interaction. The intermediate case values are also well reproduced by the Moliere theory. The variance of the scattering angle is given by :

$$\sqrt{\langle \theta^2 \rangle} = \frac{13.6 \text{ MeV}}{\beta pc} z \sqrt{\frac{x}{X_0}} [1 + 0.038 \ln(\frac{x}{X_0})] \quad (3.10)$$

Where X_0 is the radiation length and x the thickness of the target.

3.3.1 Backscattering

Due to its low mass, the probability for an electron to be backscattered is high (see Fig. 3.3). The effect is proportional to the Z of the absorber and to the inverse of the electron energy. The ratio between the incident electron and the backscattered electron is called backscattered coefficient.

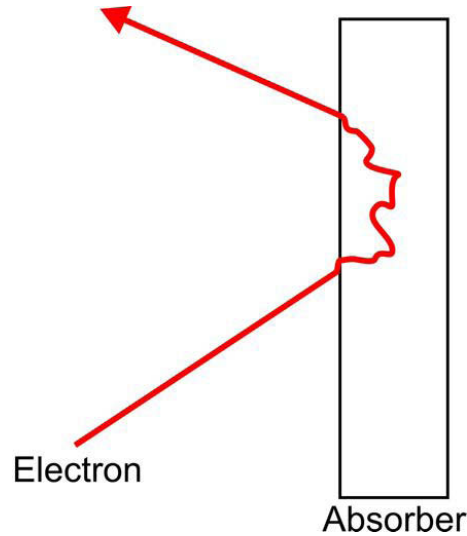


Figure 3.3: Backscattering of electron due to large multiple scattering angle.

This effect is important for a kinetic energy of the incident particle below 1 MeV. Above 10 MeV the percentage of backscattered electrons is less than 10 % for high Z material and less than 2 % for low density materials such as Carbon or Aluminum. More detail can be found in [17].

3.3.2 Range

The process of energy loss is probabilistic; the straggling is due to the fluctuation of the number of collisions and the fluctuation of the energy transfer at each interaction. For heavy particles, the range can be calculated by integrating the Bethe-Bloch formula.

$$R(E_0) = \int_0^{T_{E_0}} \left(\frac{dE}{dx}\right)^{-1} dE \quad (3.11)$$

The effect of scattering on the particle trajectory is not included in this calculation and the range calculated is smaller. For particles above few MeV, the result of the integration is similar to the experimental values. After integration, the relation between range and energy is:

$$R(E) \propto E^2 \quad (3.12)$$

The variation of the dE/dx as function of the penetration depth is called Bragg curve.

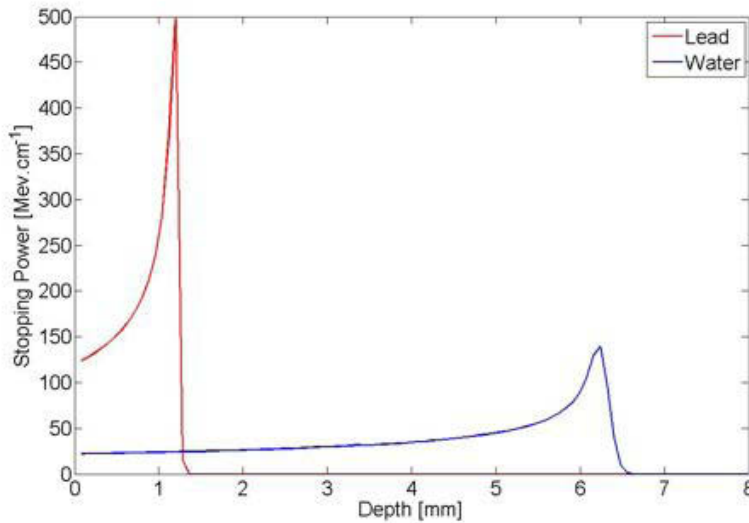


Figure 3.4: Bragg curve for 25 MeV incident protons in Water and Lead.

As shown in Fig. 3.4 this curve has a very pronounced maximum before a sharp fall, showing the energy deposition is very localized. For electron, the effect of multiple scattering induces chaotic trajectories and the range is very difficult to estimate. An approximation can be calculated with the Feather formula [18]:

$$R(E) = 412 \frac{13 A}{27 Z} E^n \quad (3.13)$$

With $n = 1.265 - 0.0954 \ln(E)$, E the energy of the electron, A and Z , respectively the number of nucleons and the atomic number of the material. R is given in $mg.cm^{-2}$.

3.4 Secondary emission

When a charged particle passes through an interface of a solid material, very low energy electrons can be emitted from the surface by the Secondary Electron Emission (SEE) process. The SEE phenomenon was discovered already in 1902 by Austin and Starke [19] and since then extensively studied for many different target projectile combinations and kinetic energy ranges going up to the few MeV . The main parameter describing the SEE is the Secondary Emission Yield (SEY), which is the average number of electrons emitted when an incident projectile enters or exits a surface. An example of the differential SEY for different target materials can be seen on Fig. 3.5 In general, the maximum is reached for energies of few eV and a longer tail extends up to several tens of eV [20].

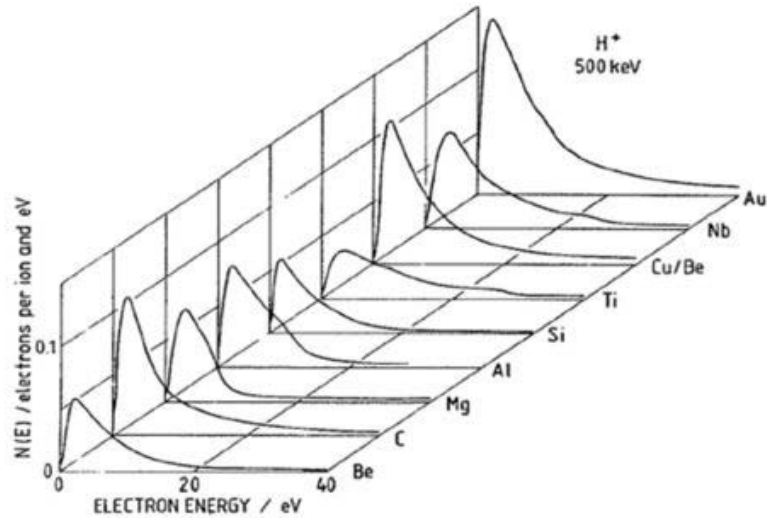


Figure 3.5: Energy spectrum of secondary electrons generated by a 500 keV proton [20].

The SEE process can be generally divided into three consecutive steps:

- Generation of secondary electrons.
- Diffusion of these electrons to the surface.

- Emission process.

The SEY for different projectile / target combinations is proportional to the energy loss rate $\frac{dE}{dx}$ in the target material. A plot summarizing the linear relationship over three orders of magnitude is shown in Fig. 3.6.

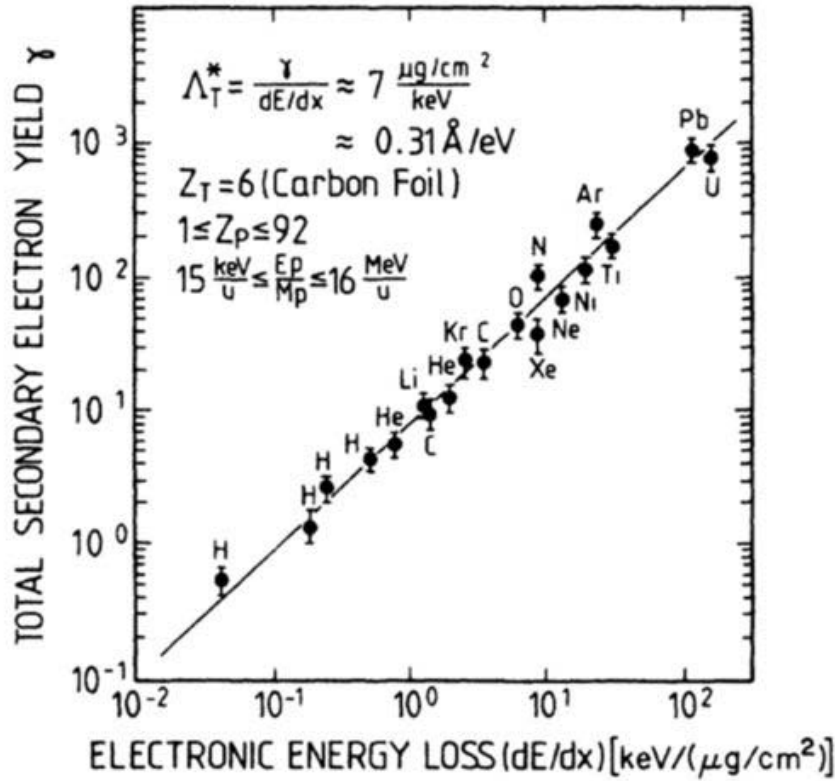


Figure 3.6: Secondary emission yield as function of the energy loss on a Carbon foil ([21]).

3.4.1 Generation of secondary electrons in solids

The secondary electrons are generated by a fast particle in matter, these particles creating electrons ion pair in the material. In order to create a secondary electron, the minimum transfer of energy is the one required to excite electrons from the conduction band above the Fermi level. The ionizations in the outer or even in the inner shells are less probable but also possible.

3.4.2 Diffusion process

The low energy electrons produced by ionization propagate through the solid, strongly interact with the electron cloud and rapidly lose their energy. The energy loss rate of low energy electrons in Aluminum can be seen in Fig. 3.7. The peak loss occurs at about 30 eV (above the conduction band). But for electrons below 20 eV, the loss rate decreases and such electrons can therefore diffuse to larger distances.

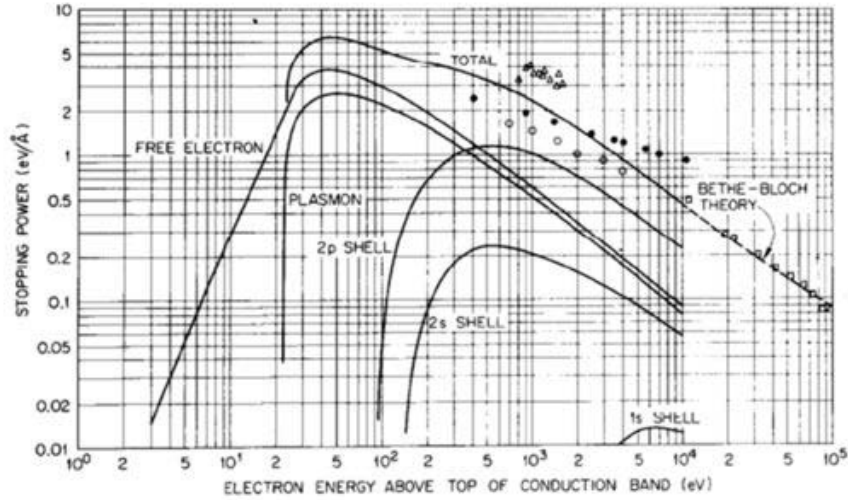


Figure 3.7: Energy losses in Aluminum for electrons as a function of electron energy. Contributions to the total stopping power from inner-shell ionization, Plasmon excitation, and electron-hole pair excitation (free electron curve). From [22].

The fast energy loss permits only a very shallow penetration depth of the low energy electrons. In metals, the behavior of the conduction band electrons can be approximated by an electron gas and the excited electrons with higher velocities propagate by diffusion and by cascade multiplication thus creating many low energy secondaries.

3.4.3 Emission process

Before a secondary electron is emitted from a metallic surface, it has to overcome the surface barrier potential, which is characterized by the mean work function and the barrier height $W = E_f + e$, with E_f as the Fermi energy and e as the surface potential.

The emission process can be regarded as a refraction phenomenon, as only the

momentum vector normal to the surface (longitudinal) is lowered due to the barrier crossing and the transverse momentum is conserved. As a consequence, the electrons able to surmount the barrier with a given energy E_i inside the solid have a velocity vector lying inside an escape cone with a maximum angle θ_{max} with respect to the surface normal:

$$\theta_{max} = \arccos\left(\sqrt{\frac{W}{E_i}}\right) \quad (3.14)$$

with $E_i \geq W$.

Assuming an isotropic distribution of the low energy electrons inside the solid, the probability $P(E)$ for a secondary electron with energy $E = E_i W$ outside the solid to penetrate the surface barrier is:

$$P(E) = 1 - \frac{W}{E_i} \quad (3.15)$$

The theoretical treatment of the SEE by E.J. Sternglass was formulated in 1957 [23] and was used in a simplified form for generating the secondary electrons in the simulations presented later in this work. The theory is valid only for the backward emission (projectile entering the target).

Two main channels of the Secondary Electron (SE) formation are assumed. The low energy electrons produced by the small energy transfer to the target electrons during ionization represent the main contribution, whereas the fast delta electrons emitted mostly in the forward region can produce additional SE. The number of low energy electrons produced in a depth x is approximated to:

$$n_e^{(1)}(x, v) = \frac{1}{\langle E_0 \rangle} \left\langle \frac{dE^{(1)}}{dx} \right\rangle \quad (3.16)$$

Where $\langle E_0 \rangle$ is the mean energy loss per secondary formed and the $\left\langle \frac{dE^{(1)}}{dx} \right\rangle$ is the mean differential energy loss going directly into the production of low energy secondaries. The number of the electrons produced by the delta electrons is:

$$n_e^{(2)}(x, v) = f(x, v) \frac{1}{\langle E_0 \rangle} \left\langle \frac{dE^{(2)}}{dx} \right\rangle \quad (3.17)$$

The stopping power $\left\langle \frac{dE^{(2)}}{dx} \right\rangle$ is now the energy loss going into the production of delta rays and $f(x, v)$ represents the fraction of that energy available for the production of delta-ray caused by electrons at the depth x . Sternglass makes use of the Bethe-Bohr equipartition rule [24] stating that half of the total ionization energy loss goes in the formation of the delta rays and the second half to the production of the slow electrons. The probability $P(x)$ that an electron produced

at a depth x can escape from the material follows an exponential behavior written as:

$$P(x) = TA \exp\left(-\frac{x}{L_s}\right) \quad (3.18)$$

where T is a surface transmission coefficient. A is a constant related to the distribution of the initial velocities of electrons and to the number of collisions required to absorb the electron. The characteristic length L_s describing the diffusion of the low energy electrons (which is of the order of distance between inelastic collisions) is obtained by:

$$L_s = \frac{1}{\alpha' N \sigma_g} \quad (3.19)$$

Where N is the number of atoms per unit volume, σ_g is the cross section of the target atoms which can be parameterized by $1.6Z^{1/3}10^{16} \text{cm}^2$ and α' is a factor depending on the cross section of the SE scattering process. The SEY is now given by

$$dSEY = n_e(v, x)P(x)dx \quad (3.20)$$

Sternglass estimated the mean energy $\langle E_0 \rangle$ lost per ion formed inside the solid to be 25 eV . Also the coefficients T and A should be constant for all the metals and were estimated to be $TA = 0.5$ and α' was obtained from the available measurements of the L_s , which lead to $\alpha' = 0.23$. The ratio of the effective path lengths of delta electrons to low energy electrons was estimated in [25] to $L/L_s = kE/Ap$, with $k \approx 5.4 \times 10^6 \text{amu.eV}^{-1}$ and E and Ap the kinetic energy and mass of the projectile. If the above estimations are inserted into the previous equations, the following numeric relation is obtained [26]:

$$SEY = 3.6810^{-19} \frac{N_a \rho Z^{1/3}}{M} \left[1 + \frac{1}{1 + (5.410^{-6} E_k)} \right] \frac{dE}{dx} \quad (3.21)$$

With E_k in eV and $\frac{dE}{dx}$ in eV.cm^{-1} .

This formula is valid for the secondary electron emitted on the entry face on the target. For the rear face, the secondary emission is difficult to distinguish from the exiting δ -rays. In first approximation, we consider this formula also for SEY of the rear face, assuming the fact that the error due to δ -ray emission can be in the order of few %.

3.5 Electron stripping

Measurements of the stripping cross section for H^- and H^0 on carbon at 2 MeV and 7 MeV are available in literature [27]. The ionization cross sections depend on $\frac{1}{\beta^2}$ (relativistic factor) of the ions and on the Z of the material [27]. In order to obtain values suitable for our studies the experimental results are interpolated (see Table 3.1), 3 MeV is the energy at the exit of the RFQ, 12 MeV at the exit of the DTL tank 1. Since the cross section is decreasing with energy, these two cases are the most critical for the emission of secondary electron.

Energy [MeV]	β	$\sigma_{-0}(10^{-16}cm^2)$	$\sigma_{0+}(10^{-16}cm^2)$
2 (measured)	0.065	1	0.4
3 (scaled)	0.08	0.66	0.264
7 (measured)	0.12	0.35	0.15
12 (scaled)	0.16	0.16	0.11

Table 3.1: Measured and extrapolated cross section

Where σ_{-0} is the cross section of the stripping of H^- ions into a H^0 and σ_{0+} is the cross section for stripping an H^0 into an H^+ .

Fig. 3.8 shows the ratio of the different hydrogen ions mixture as a function of the depth inside a carbon foil.

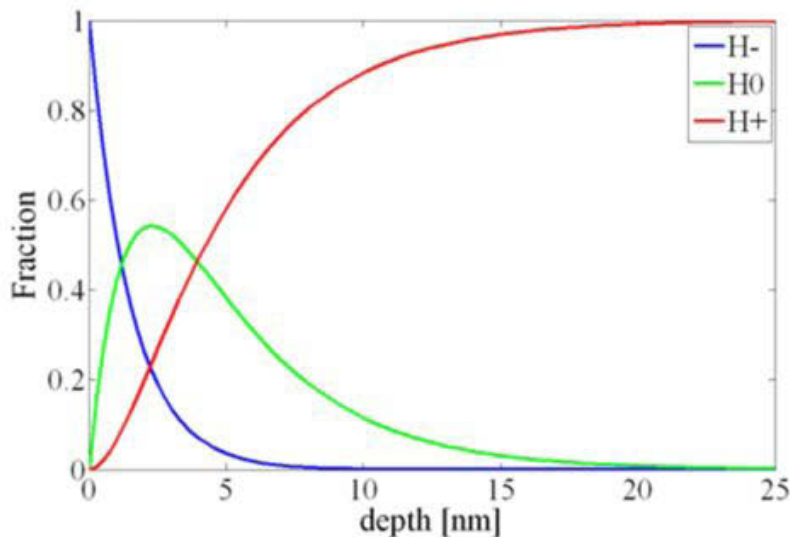


Figure 3.8: Relative fraction of hydrogen ions inside a carbon foil for a 3 MeV impinging H^- beam.

The secondary emission is an effect that takes place in a very thin layer near the surface of the material. Below a few MeV the H^- ions are stripped in the first few nanometers and the secondary emission of the incoming particle is dominated by the proton while for beam energies above 3 MeV the ionization happens after the SE layer and the secondary emission is dominated by the H^- ions. The SEY of the H^- ions is again calculated with the Sternglass formula assuming that the stopping power of the H^- ions is the same as that of protons.

For the higher energy, the measurement of the cross section at 200 MeV is available [28], these results have been interpolated to 160 MeV (see Table 3.2).

Energy [MeV]	β	$\sigma_{-0}(10^{-19}cm^2)$	$\sigma_{0+}(10^{-19}cm^2)$
160 (scaled)	0.52	17.72	6.92
200 (measured)	0.566	15.33	6

Table 3.2: Stripping cross section at 200 MeV (measured) and at 160 MeV (scaled) for H^- ion and Hydrogen atom impinging a carbon foil.

For a Carbon foil with a density of $1.7 g.cm^{-3}$, the ratio of H^- is less than 10^{-6} after $0.9 \mu m$, while for H^0 , the same ratio is obtained after $2.35 \mu m$. These results show that for a layer thicker than $3 \mu m$, the H^- ions could be considered fully stripped. At lower energy, the thickness sufficient for a full stripping is smaller. For typical thickness of the profile monitors (wire, screens etc), it can be assumed that H^- are fully stripped at all LINAC4 energies as they hit the monitor.

Chapter 4

SEM grids and wire scanner in LINAC4

4.1 Introduction

During the operation of the LINAC4, beam profile measurements will be performed from 3 *MeV* to 160 *MeV* with SEM grids and wire scanner. In addition, 3 SEM grids will be used in the diagnostic test bench, designed for the commissioning at 3 *MeV* and 12 *MeV* in the laboratory and in the LINAC4 tunnel (see Chapter 1). These profile diagnostics can be separated in 3 groups depending on the beam characteristics at their locations:

- Low current and high energy deposition.
- High current and low energy deposition.
- High current and high energy deposition.

The first case corresponds to the grid in the diagnostic test bench, the second to the wire scanners and SEM grids installed in LINAC4 at beam energies above 50 *MeV*, and the last one to the two wire beam scanners installed in the Chopper line at 3 *MeV*. In order to estimate the thermal load and the signal each case has been studied separately.

4.1.1 Secondary Emission Monitor (SEM grid)

The process of secondary emission is described in Chapter 3. Typically, a secondary emission monitor (SEM) consists of thin ribbons or wires, which individually interact with the beam. Each wire of the grid is connected to an individual acquisition channel and sampled with an Analog to Digital Converter (ADC). The

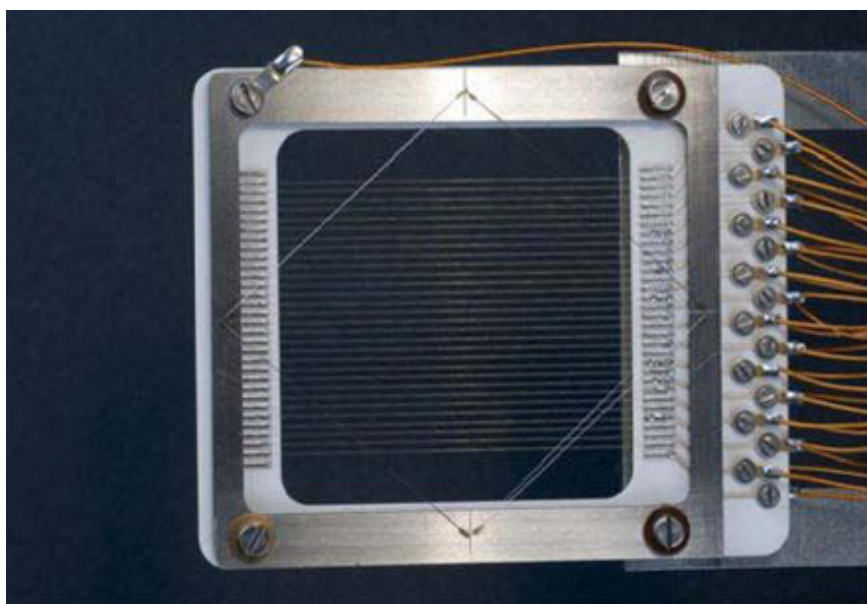


Figure 4.1: Example of a SEM grid installed in the CERN accelerator complex.

signal is proportional to the number of particles reaching each wire, and allows the reconstruction of the beam profile. An example of a SEM grid is shown in Fig. 4.1.

In addition, SEM grids are also used for emittance measurement (see Chapter 5) and in a dispersive region for energy spread measurement. In both cases, the SEM grid is positioned downstream a slit, that allow the sampling of a small slice of the beam. In case of Energy spread measurement, a bending magnet is positioned between the slit and the grid, the profile monitor is at a focal point of the bending magnet and the spread in energy of the beam can be reconstructed by the profile measurement given by the grid.

Materials with a high melting (or sublimation) point are generally used for the wire, in particular at low energy where the stopping power is higher. The monitor is mounted on a pneumatic feed-through (see Fig. 4.2) or on a movement with a stepping motor, that allows its removal from the parking position only during the measurement and possibly its fine movement inside the beam pipe aperture.

A SEM grid intercepts few percent of the total beam, and can be considered as a non destructive measurement. For protons or electrons, the particles passing through the wires are scattered, leading to an increase of the emittance. At all LINAC4 energies, H^- ions are fully stripped as they traverse the wires and the emerging protons are lost. Even though the fraction of lost particles is small, the system design must ensure not to damage the downstream machine elements.

Fig. 4.3 shows an example of beam profiles measured with SEM grids in LINAC2 (protons with energy of 50 MeV).

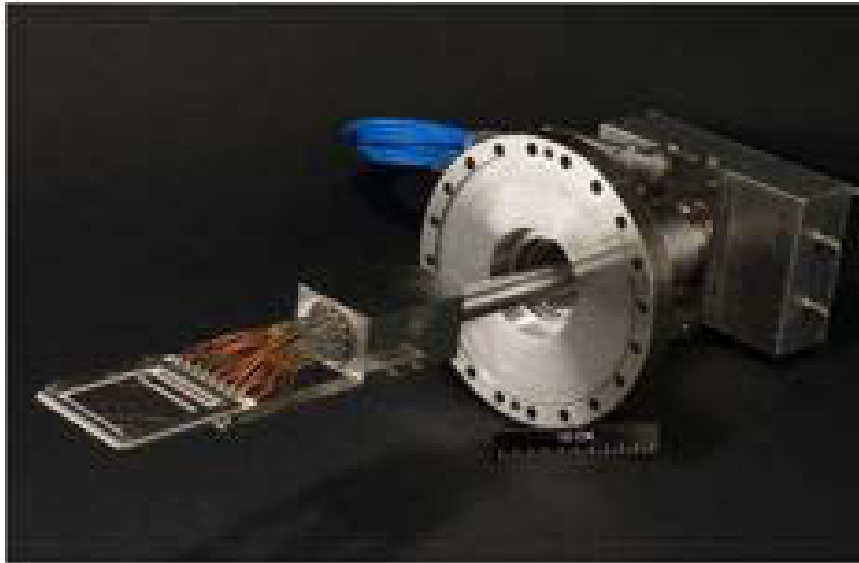


Figure 4.2: SEM grid and its actuation system

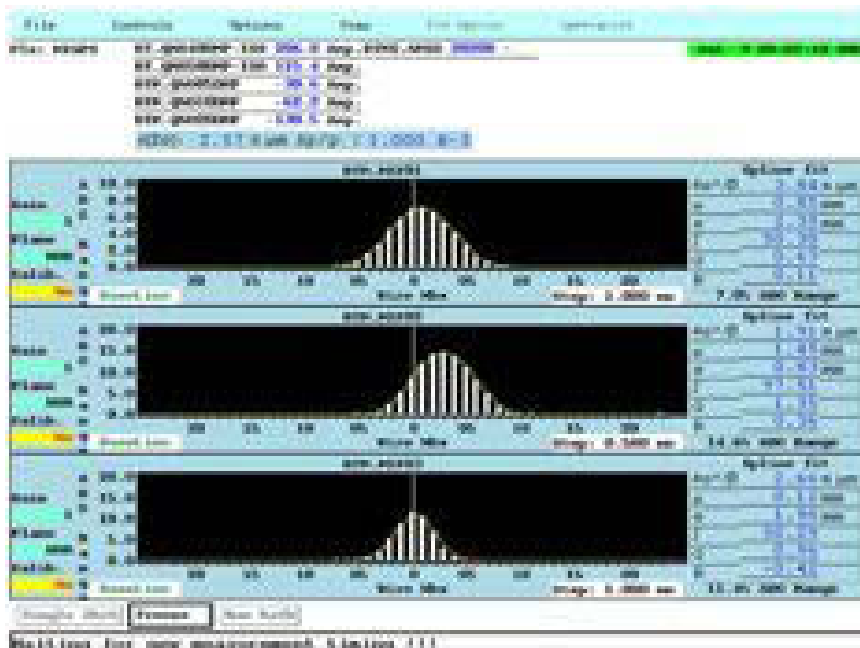


Figure 4.3: Profile measurement with SEM grids used at the exit of the LINAC2 at 50 MeV

The system resolution is determined by the wires spacing. Increasing the number of wires improves the measurement and resolution but requires more electronics

channels.

4.1.2 Wire Beam Scanner (SEM mode)

In order to minimize the cost and increase the resolution, a single wire can be moved across the beam. By means of stepping motors, it is possible to sample the particle distributions with resolutions of the order of the wire diameter, typically $30\text{-}50\ \mu\text{m}$. Fig. A.10 shows an example of a wire beam scanner designed for the electron injector of the CERN LEP (Large Electron Positron collider).

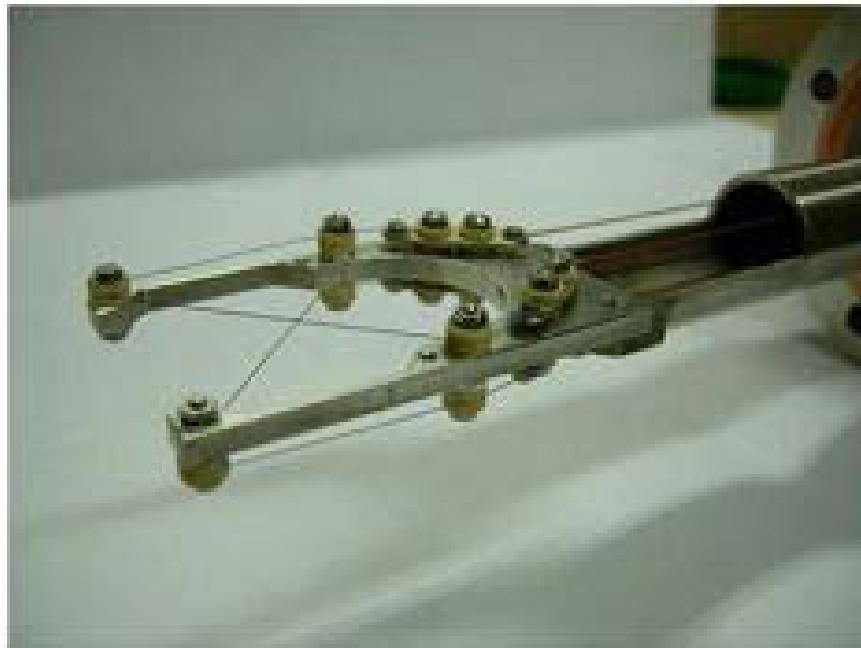


Figure 4.4: Detail of the fork on a wire beam scanner used in the LPI (LEP injector), the two wires are used to sample the two transverse planes at the same time.

The two wires are mounted on a fork, that is inserted in the beam pipe by a single feed-through oriented at 45° with respect to the vertical. This allows the simultaneous measurement of both transverse planes. The schematic diagram of a wire beam scanner is shown in Fig. 4.5.

When used in linacs, a SEM grid can measure the beam profile in one pulse, while a wire beam scanner can measure only one profile point per linac pulse. Consequently, a high resolution measurement can take several minutes.

SEM grids and wire scanners designs have many common aspects, like the estimation of the wire signal and the thermal loads induced by the beam hitting the wires.

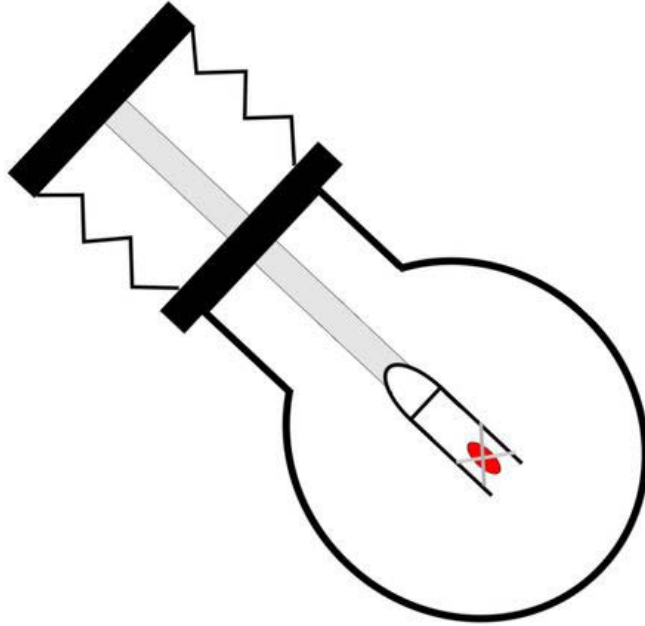


Figure 4.5: Diagram of a Wire Beam Scanner.

4.1.3 Signal generation-Secondary emission of H^-

The secondary emission of the exiting particles depends on the ion energy and on the wire properties and geometry as the H^- ions will be decomposed into the 3 constituents and these will lose energy and eventually be stopped inside the material. The charge created on the wire is given by the formula:

$$Q = Y_e + \eta Y_s + (1 - \eta) - 2\mu \quad (4.1)$$

Where Y_e and Y_s are respectively the SEY of H^- and the SEY of proton exiting the wire, η is the proportion of proton exiting the wire, μ the proportion of electron stopping in the wire. Above 50 MeV , $\eta = 1$ and the stopping power of the particles entering the wire is the same as the particle exiting the wire, in this case $Y_e = Y_s$ and the charge created becomes:

$$Q = 2Y - 2\mu \quad (4.2)$$

With $Y = Y_e = Y_s$.

The proportion of electron exiting the wire is determined by the geometry and the material of the wire. The energy of the electron is reduced by a factor 1836 compare to the energy of the H^- ions, we also assume that the two electrons don't lose energy during the ionization process. The range of the electron is given by the formula:

$$r(E) = 412 \frac{13 A}{27 Z} E^n \quad (4.3)$$

With, $n = 1.265 - 0.0654 \ln(E)$ and E is the energy of the electron.

Until now, the probability of backscattering for stripped electron has not been considered. At low energy, this probability is not negligible and the charge creation must be modified. From Eq. 4.2:

$$Q' = 2Y + 2\mu \cdot f(E, Z) \cdot [Y_b - 1] \quad (4.4)$$

Where $f(E, Z)$ is a function depending on the beam energy E and the wire material Z and Y_b the SEY of backscattered electrons. $f(E, Z) < 1$ for all the energies and material considered (see Appendix A).

In the next sections, the charge has been calculated with Eq. 4.2 for energies below 20 MeV, due to the lack of data available in this energy range and the possible error at very low energy in the Monte Carlo simulation code. Above 50 MeV both charge with and without backscattering effect has been estimated.

Creation of δ -ray has also an influence on the charge creation, Eq. 4.4 can be modified:

$$Q'' = Q' + g(E, Z) \quad (4.5)$$

$0 \leq g(E, Z) \ll 1$ for all the energies and material considered.

4.2 Thermal aspect

4.2.1 Temperature and cooling

The thermal load on the wires induced by the beam could produce thermo ionic emission and in the worst case damage the wire. Given a linac pulse, populated by N_{part} particles with RMS transverse beam sizes σ_x and σ_y , traversing a wire, the induced temperature can be calculated as [29]:

$$\Delta T = \frac{N_{part}}{Cp(T)} \frac{dE}{dx} \frac{1}{2\pi\sigma_x\sigma_y} e^{-\left(\frac{x^2}{2\sigma_x^2} + \frac{y^2}{2\sigma_y^2}\right)} \quad (4.6)$$

Where $Cp(T)$ is the specific heat capacity of the material of the wire and $\frac{dE}{dx}$ the stopping power of the particles in the material. In first approximation, the wire

cooling is dominated by black body radiation, described by Stefan-Boltzmann's law. The heat radiated from the wire surface is proportional to the fourth power of the temperature. The difference from the ideal black-body radiation is described by a factor called emissivity and the radiated power is given by :

$$P = \sigma \varepsilon A (T^4 - T_0^4) \quad (4.7)$$

Where σ is the Stefan-Boltzmann constant, ε the emissivity, A the area of the body, T its temperature and T_0 the ambient temperature. After a linac pulse the temperature variation can be calculated as:

$$\frac{dT}{dt} = \frac{\sigma \varepsilon A (T^4 - T_0^4)}{\rho C p(T) V} \quad (4.8)$$

Where ρ is the wire material density and V the wire volume of the wire.

To estimate the temperature increase, we assume that the energy deposition is constant in the direction of beam propagation (i.e perpendicular to the wire axis). The wire has been separated in thin slices, where the particle density is almost constant, Eq. 4.6 and 4.8 have been used to estimate the wire heating after one or more linac pulses inside a bin. It was also assumed that there is no temperature gradient inside each bin.

4.2.2 Thermionic emission

If the wire temperature increases above a given threshold, the thermal energy transferred to the material electrons overcomes their binding potential and they can escape from the wire surface. This phenomenon is known as thermionic emission. The density of the current emitted by the wire is described by Richardson-Dushman :

$$J_{th} = AT^2 e^{-\frac{\phi}{kT}} \quad (4.9)$$

Where ϕ is the binding potential (or work function) and A is Richardson constant, theoretically equal to:

$$A = \frac{4\pi m_e k^2 q_e}{h^3} \quad (4.10)$$

With m_e the electron mass, k , the Boltzmann constant, q_e the charge of the electron and h the Planck constant. In the case of carbon $A = 120.3A/(cm^2 K^2)$ and the work function is equal to $\phi(T) = 4.39eV - 1.7 \cdot 10^{-4} eV \cdot T$

The variation of the current emitted by a 40 μm carbon wire as function of temperature is shown in Fig. 4.6.

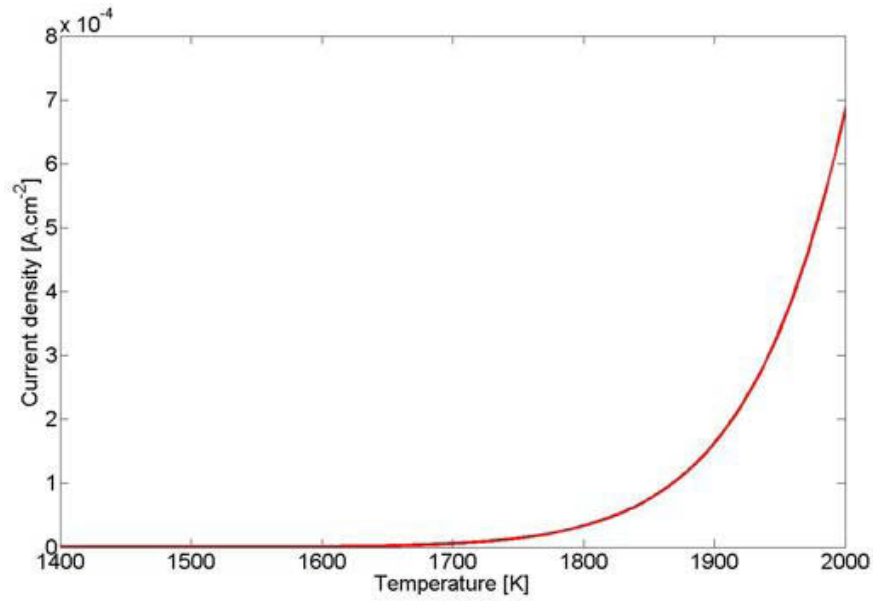


Figure 4.6: Thermionic current as a function of the temperature for a carbon wire.

The thermionic emission is threshold process. Below 1500 K in case of carbon, the emitted current can be neglected. For tungsten, the threshold is similar. Above this temperature, the emitted current density increases quickly and could perturb the measurement. Nevertheless, in the case of the wires for SEM grids or WBS the energy deposition is localized in a small volume of the wire, the area with a temperature above the threshold emission is thus very small.

4.2.3 Sublimation of a carbon wire

High temperatures can yield to damage of the wire due to sublimation. This can be modeled by a carbon vapor (as an ideal gas), lying in a thin layer in equilibrium with the wire material. The carbon vapor pressure depends strongly on temperature; data is available in literature and is shown on Fig. 4.7 [30].

In the thin layer around the wire, the average velocity of the carbon atoms can be calculated by the ideal gas theory:

$$V = \frac{1}{2} \sqrt{\frac{8kT}{m\pi}} \quad (4.11)$$

Where k is the Boltzmann constant, m the mass of a carbon atom and T the temperature considered as uniform around and at the surface of the wire and equal and calculated with the Eq, 4.6 and 4.8 . The vapor density in the layer is also

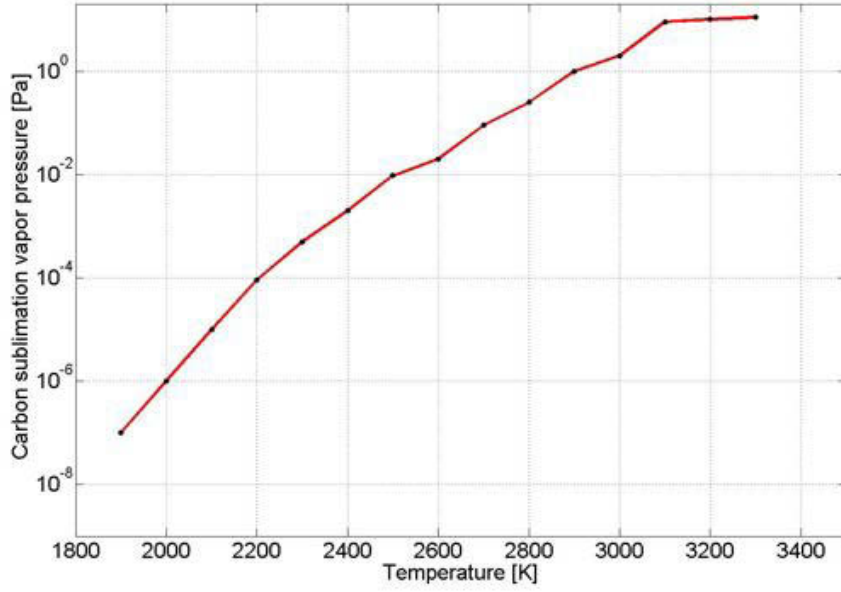


Figure 4.7: carbon sublimation vapor pressure as function of temperature

given by the ideal gas theory:

$$\frac{P_{atm}V_0}{T_0} = \frac{P_v V}{T_v} \quad (4.12)$$

From this, the carbon vapor density can be calculated as:

$$\rho_v = \frac{MT_0P_v}{V_{mol}P_0T_v} \quad (4.13)$$

Where M is the molar mass of carbon, V_{mol} the molar volume (22.4 dm^3), P_v the vapor pressure, T_v the temperature of the vapor and T_0 and P_0 the atmospheric pressure and standard temperature respectively. The amount of matter exiting the surface is equal to

$$\phi = \frac{1}{2}\rho_v V \quad (4.14)$$

ϕ in $\text{g.cm}^2\text{s}^{-1}$.

With a density of carbon equal to $\rho = 2 \text{ g.cm}^3$, the velocity of decrease radius is

$$v_d = \frac{\phi}{\rho} \quad (4.15)$$

The result of the wire heating (see section 4.4.3) shows that the maximum temperature is 2800 K , for which the radius of the wire is decreased by $1\ \mu\text{m}$ after 2 hours.

If the temperature is below 2000 K , the life time of a wire is above 15 years.

4.3 Test bench SEM grids

During the commissioning phase, 3 SEM grids will be used in the test bench, two for the emittance measurement and one in spectrometer line for the energy spread measurement [31], a diagram of the diagnostic test bench is show in Fig 4.8.

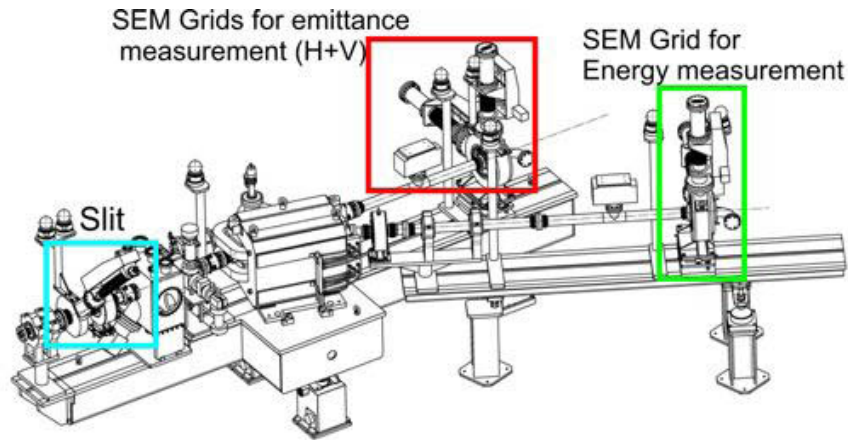


Figure 4.8: Diagram of the test bench

4.3.1 Resolution-SEM grid pitch

For the two SEM grids used for the emittance measurement, the resolution will be discussed in Chapter 5, where it is explained how the SEM grids are driven by stepping motors and how the measurement resolution can be improved by small steps for each slit position. The spectrometer grid is equipped only with an IN-OUT system and the profile resolution is determined by the distance between wires (grid pitch). The pitch must be chosen in order to reach the best resolution for 3 different measurement locations. The main parameters of the particle distribution at the grid position are summarized in Table 4.1 .

The total beam width (5 RMS) varies from 9 mm (DTL) to 22 mm (MEBT). In order to minimize electronics cost and complications, the number of acquisition channels should not exceed 48. To reach a good resolution, the sensitive area should cover the all beam and at least 3 wires per RMS beam size should provide

Position	RFQ	MEBT	DTL
σ_x (1 RMS) [mm]	3.08	4.4	1.8
σ_y (1 RMS) [mm]	10	12	10.4
E <i>MeV</i>	3	3	12

Table 4.1: Beam parameters at the SEM grid position.

a signal. With a wire spacing of 1 *mm*, 3 and 4 wires should provide signals for the RFQ and MEBT cases respectively. Nevertheless, in the DTL case, with this pitch, less than 2 wires per σ of the beam size are hitting by the beamlet and the resolution will be degraded. The criterion for a good measurement resolution is achieved by using a pitch of 500 μm . With a constant pitch, the sensitive area will not be sufficient to cover the full MEBT beamlet. The solution so far is to use a 500 μm pitch for the central wires and a 1 *mm* pitch for the outside wires. From side to side, the grid will consist of:

- 12 wires with 1 *mm* pitch
- 24 wires with 500 μm pitch
- 12 wires with 1 *mm* pitch

For a total sensitive area of 36 *mm*, which is enough to intercept the all beamlet. This solution allows a good measurement resolution in all cases with 48 acquisition channel.

4.3.2 Test Bench SEM grids signal

Starting from the SEM grid systems foreseen for the test bench, the percentage of protons leaving the wire and their energy has been simulated using FLUKA [32]. The average kinetic energy of such protons is used to calculate the SEY while, the number of charges created (in unit of electron charge) per ion hitting the wire is given by the Eq. 4.13. At 3 and 12 *MeV*, the two electrons of the H^- ions have not enough energy to cross the wire. Two wire types have been considered: a 40 μm diameter tungsten wire and a 33 μm diameter carbon wire.

Signals at 3 MeV

At 3 *MeV* the range of protons in tungsten is about 30 μm , therefore about 73 % of the protons are stopped inside the 40 μm tungsten wire, the remaining fraction produces SE as they exit the wire. The average kinetic energy of these leaving protons is 1.52 *MeV*. The contribution to the signal is thus -0.18 electrical

charge (e) per H^- . For carbon the range of protons is about $100 \mu m$ and all protons will exit the wire. The signal from a carbon wire is provided by direct charge deposition of electrons and SE generated by both entering H^- ions and exiting protons. In this case the signal is $-1.26 e$ per H^- ion hitting the wire, higher than the one for tungsten.

Signals at 12 MeV

At $12 MeV$ the range of protons is larger than $200 \mu m$ in tungsten and around $1 mm$ in carbon. For a tungsten wire, the contribution of SE is equal to $0.65 e/H^-$. The total signal for tungsten is thus $-1.35 e/H^-$ while for carbon the total signal is $-1.8 e/H^-$.

These results are compiled in Table 4.2.

Energy [MeV]	carbon	tungsten
3	-1.23	-0.18
12	-1.8	-1.35

Table 4.2: Charge creation in carbon and tungsten wire for a beam energy of 3 and $12 MeV$

Expected current

Fig. 4.9, Fig. 4.10 and Fig. 4.11 show the expected signal for the 3 stages foreseen for the test bench in case of horizontal emittance measurement. For each position, the particle distribution at the SEM grid location for the slit in the central position and close to the beam edges have been sampled from PATH simulations [33]. These distributions have been used for simulating the signal on SEM grids with 40 wires and a pitch of $0.5 mm$.

From this figures it can be concluded that:

- At $3 MeV$, the signal provided by a carbon wire is 5 times higher than a tungsten wire.
- The maximum current is few μA at the MEBT and RFQ, the noise from the acquisition channel is about $5 nA$, when the slit is on the central position the ration signal/noise is around 1000 for a carbon wire and 200 for a tungsten wire.
- When the slit is moved to the beam edges, for a carbon wire the signal is around $50 nA$, (ratio signal/noise of 10), an $10 nA$ in case of tungsten close to electronic noise, carbon wire should be used at $3 MeV$.

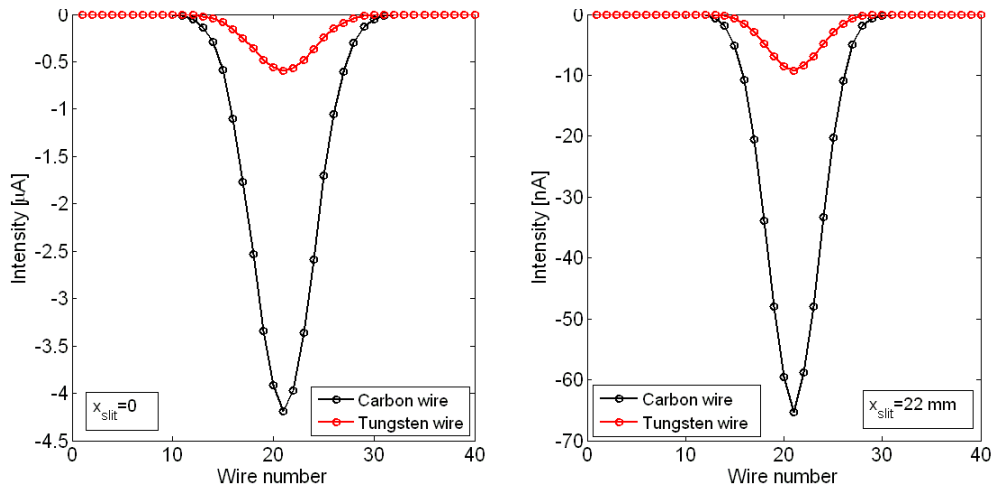


Figure 4.9: Expected current for an emittance scan after the RFQ, when the slit is at the center of the beam (left) and when the slit is moved to the beam edge (right).

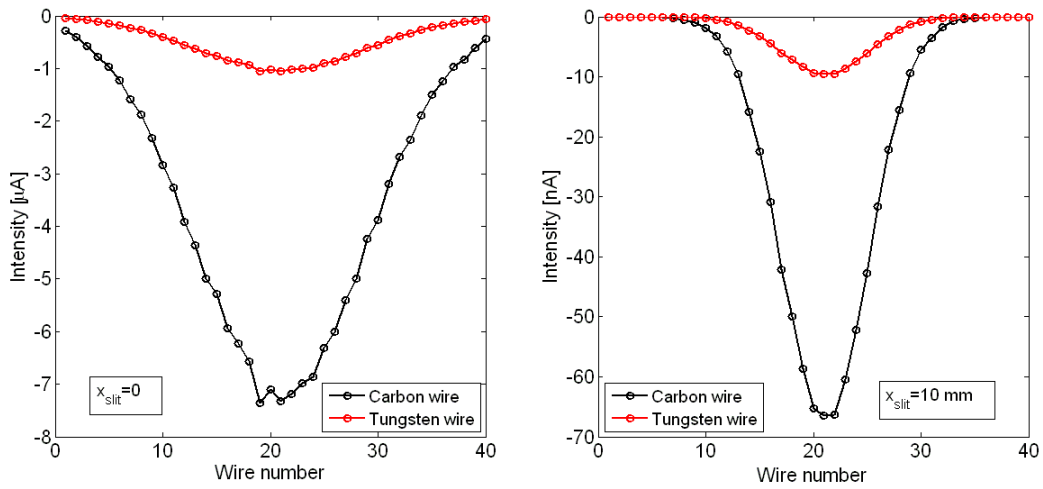


Figure 4.10: Expected current for an emittance scan after the MEBT, when the slit is at the center of the beam (left) and when the slit is moved to the beam edge (right).

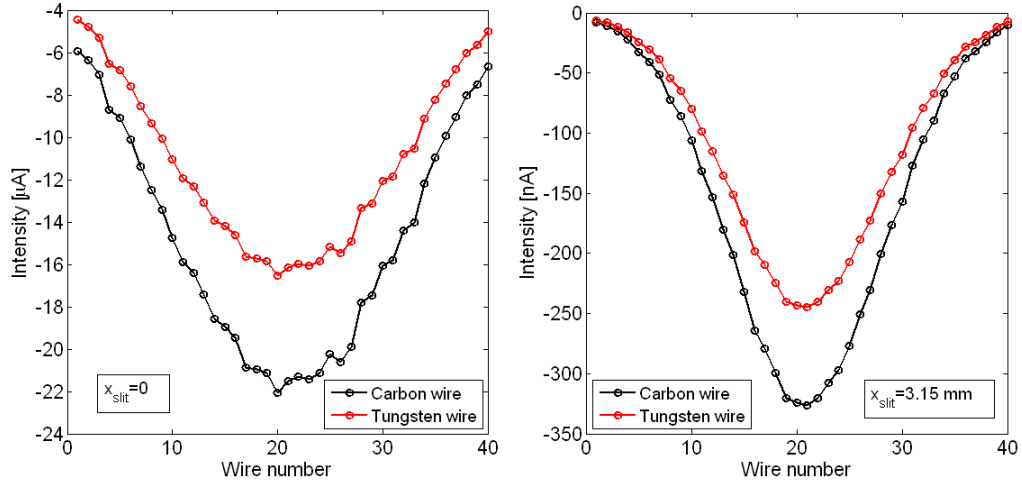


Figure 4.11: Expected current for an emittance scan after the DTL, when the slit is at the center of the beam (left) and when the slit is moved to the beam edge (right).

- At 12 MeV the signal provided by a tungsten wire is in the order of the signal provided by a carbon wire, both material can be used.
- A pitch of 0.5 mm is not enough for several slit positions, and a larger sensitive area is sometimes needed.

4.3.3 Wire heating

As shown in Fig. 4.12, at low energy, the stopping power is not constant in the wire, even though in case of a 40 μm tungsten wire, a 3 MeV protons beam is stopped inside the wire and the energy deposition at the Bragg peak position is much higher than the energy deposition at the surface of the wire. To be conservative, the maximum of energy deposition has been used to calculate the temperature increase i.e at 3 MeV :

- 125 $MeV.g^{-1}.cm^{-2}$ for a 33 μm carbon wire.
- 100 $MeV.g^{-1}.cm^{-2}$ for a 40 μm tungsten wire.

For the DTL case, the stopping power is more or less constant, and the stopping power from table has been used.

Table 4.3 and Table 4.4 show the maximum temperature reached on the wire at the center of the beamlet passing through the slit for both carbon and tungsten wires and at the 3 measurement positions as calculated using Eq. 4.6 and Eq. 4.8

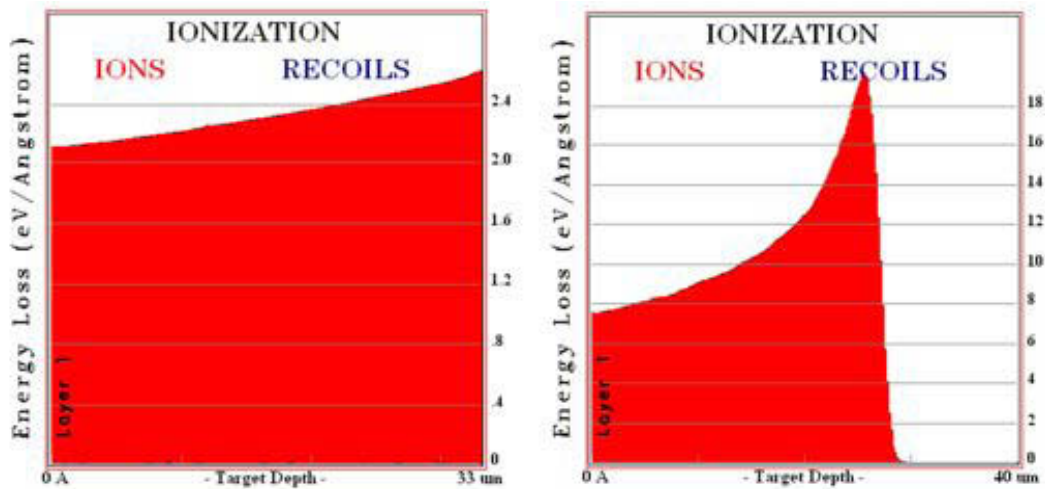


Figure 4.12: Energy deposition of a 3 MeV protons beam inside a 33 μm diameter carbon wire (left) and 40 μm diameter tungsten wire (right) data from SRIM [34].

Material	carbon	tungsten
Position	Tmax [K]	Tmax [K]
RFQ	309	343
DTL	303	320
MEBT	306	306

Table 4.3: Maximum temperature on the SEM grid in the emittance measurement line.

Material	carbon	tungsten
Position	Tmax [K]	Tmax [K]
RFQ	299	299
DTL	299	299
MEBT	299	299

Table 4.4: Maximum temperature on the SEM grid in the spectrometer line, the temperature increase is below 1K, the values has been approximated, assuming a room temperature of 298 K.

Due to the small proportion of particles passing through the slit, in all cases, the temperature is far below the sublimation/melting point (3773 K for graphite and 3680 K for tungsten) of the materials and also well below the threshold for thermionic emission.

4.4 WBS and SEM grid in the LINAC4 line

4.4.1 Signal

As for the test bench SEM grids, carbon (33 μm diameter wires) and tungsten (40 μm diameter wires) are the materials considered for all BWS and SEM grids to be installed in LINAC4. The range of the electrons in these two materials has been calculated with Eq. 4.3 for beam energies from 50 MeV to 160 MeV in 10 MeV steps (see Tab. 4.5).

Beam Energy [MeV]	Electron energy [MeV]	Range in C [μm]	Range in W [μm]
50	0.0272	6.02	0.77
60	0.0327	8.57	1.10
70	0.0381	11.5	1.48
80	0.0436	14.77	1.90
90	0.0490	18.37	2.36
100	0.0545	22.27	2.86
110	0.0599	26.47	3.40
120	0.0654	30.94	3.98
130	0.0708	35.67	4.58
140	0.0763	40.65	5.22
150	0.0817	45.87	5.89
160	0.0871	51.31	6.59

Table 4.5: Electron range in carbon and tungsten.

At all LINAC4 energies, the two H^- electrons are stopped in the tungsten wire. For a carbon wire, if we assume an average width of $d_{eq} = \pi d/4 = 26\mu m$, the electrons have enough energy to escape the wire for beam energies above 110 MeV .

At first neglecting the effect of backscattering, but taking into account knowledge of the stopping power (see Chapter 3) this allows estimating the charge in the wire, as shown in Table 4.6.

For a carbon wire the polarity of the signal changes for beam energies above 110 MeV , and the charge deposition is reduced by at least factor 50. For a tungsten wire, the signal polarity does not change and the charge deposition remains almost constant. The secondary emission of electrons can be suppressed with a positive bias voltage on the wire. Secondary electrons have a low energy (about a few eV) and a voltage of 100 V is enough.

With a biased tungsten wire, the charge deposition is equal to -2 independently of beam energy. For a carbon wire, below a certain threshold the charge deposition

Beam Energy [<i>MeV</i>]	charge deposition in carbon wire	charge deposition in tungsten wire
50	-1.934	-1.762
60	-1.943	-1.791
70	-1.949	-1.812
80	-1.954	-1.829
90	-1.958	-1.842
100	-1.961	-1.854
110	-1.964	-1.863
120	0.034	-1.871
130	0.032	-1.877
140	0.030	-1.883
150	0.029	-1.888
160	0.028	-1.893

Table 4.6: charge deposition in a 40 μm tungsten wire and a 33 μm carbon wire (whithout bias polarization).

is equal to -2. Above this threshold, if the polarization is still active, the charge deposition is equal to 0. In conclusion, the polarization on the wire is an advantage for several reasons:

- The signal per ion is independent of beam energy.
- SE is influenced by surface aging, that can vary for different wires, but the signal provided by the wire with polarization is constant.

Even with polarization bias, the creation of δ -ray in the wire could perturb the measurement; these electrons with high energy are not affected by the polarization.

In order to keep the charge deposition constant, the wire diameter must be at least twice the electron range, that means for a carbon wire, the diameter must be 100 μm at 160 *MeV*.

4.4.2 Expected current with polarized wires

The nominal LINAC4 beam intensity is 40 *mA*, whereas during the commissioning phase it can be increased to 70 *mA*. The beam sizes are almost constant at the monitor locations, about 1 *mm* in one plane and 2 *mm* in the other (RMS beam sizes). The expected current has been calculated for the central wire and for the plane where the beam size is minimum, four types of wire have been simulated:

- carbon wire with a diameter of 33 μm and 100 μm .
- tungsten wire with a diameter of 40 μm and 100 μm .

In all the cases, a bias polarization on the wire has been simulated excepted for the 33 μm diameter carbon wire above 100 MeV , where the signal will be 0 if a polarization is applied.

Energy [MeV]	$I = 70mA$		$I = 40mA$	
	carbon	tungsten	carbon	tungsten
50	-1.8428	-2.2330	-1.0530	-1.2760
57	-1.8428	-2.2330	-1.0530	-1.2760
79	-1.8428	-2.2330	-1.0530	-1.2760
86	-1.8428	-2.2330	-1.0530	-1.2760
100	-1.8428	-2.2330	-1.0530	-1.2760
115	0.044	-2.2330	0.025	-1.2760
129	0.040	-2.2330	0.023	-1.2760
145	0.039	-2.2330	0.022	-1.2760
160	0.036	-2.2330	0.021	-1.2760

Table 4.7: Intensity on the central wire (polarized with 100 V) for a 33 μm carbon wire and a 40 μm tungsten wire (result in mA), when considering the maximum and the nominal beam current.

The results for a 33 μm carbon wire and a 40 μm tungsten wire are shown in Table 4.7. As expected, at low energies, the signal is constant and depends only on the wire cross section, with a larger diameter the tungsten provided larger signal (in absolute). Above 100 MeV , the carbon wire signal changes polarity and becomes 40 times smaller, therefore a larger wire must be used to have enough signal for the measurement. For tungsten wires the signal stays constant.

Energy [MeV]	$I = 70mA$		$I = 40mA$	
	carbon	tungsten	carbon	tungsten
50-160	-5.5810	-5.5810	-3.1890	-3.1890

Table 4.8: Intensity on the central wire (polarized with 100 V) for a 100 μm carbon or tungsten wire (result in mA), when considering the maximum and the nominal beam current.

When considering 100 μm polarized wires (see Table 4.8), the signal depends on the beam intensity but not on wire material and beam energy. The difference

of the signal between 40 μm and 100 μm tungsten wires can be seen on Fig. 4.13 (beam sizes o 1 $mm \times 2 mm$).

Without bias, the signal is reduced from 5.3 % to 12 % (depending on the beam energy) in case of tungsten wire and less than 3.5 % for a carbon wire. The signal is also reduced by few percent due to the emission of δ rays for tungsten wire (40 an 100 μm wire) at all energies and carbon wires (33 μm diameter wire) for energies below 110 MeV and increased above this energy.

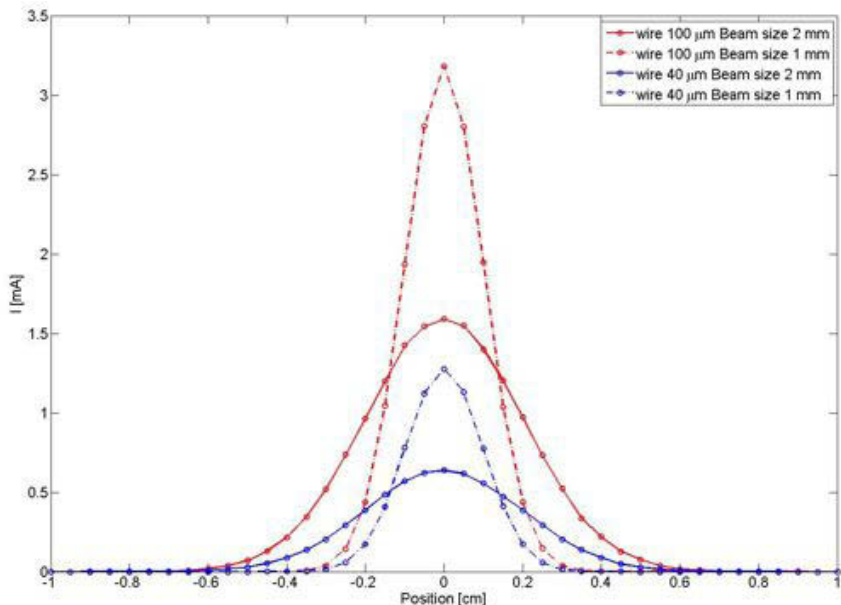


Figure 4.13: Absolute current for a 40 and 100 μm wire diameter and a beam size of 1 and 2 mm whitout considering electron backscattering.

Effect of backscattered electrons on the signal

So far, the effect of backscattering electrons on the signal has not been considered. Appendix A shows in detail the different studies done in order to estimate this effect. For SEM grids the backscattering of stripped electrons leads to a decrease of the absolute signal and a negligible effect on the beam profile reconstruction. The results for the 50 MeV and 160 MeV cases are presented in Table 4.9.

Polarized wires have been considered in order to avoid SE and use the wires as a Faraday cup for extra electrons of H^- ions.

For tungsten wires, the signal is reduced by about a factor 2 with respect to the case neglecting electron scattering, such reduction is almost constant for all the LINAC4 energies.

H^- energy [MeV]	e^- energy [keV]	$I = 70mA$		$I = 40mA$	
		carbon	tungsten	carbon	tungsten
50	27	-1.52	-1.02	-0.86	-0.58
160	90	-0.095	-0.98	-0.054	-0.56

Table 4.9: Intensity in mA on the central wire (polarized with 100 V) for a 33 μm carbon wire and a 40 μm tungsten wire (result in mA), when considering the maximum and the nominal beam current (1 mm rms beam size).

For carbon wires, at low energy (50 MeV) the signal is reduced by about 20 %. At high energy, Monte Carlo simulations evidences that a small amount of electrons are stopped in the wire, even with a 33 μm wire diameter. The SE caused by backscattered electrons is of the same order of magnitude of the SE generated by the protons with the same $\beta\gamma$. This is not a problem for beam energies below 100 MeV when biasing the wires suppresses the SE and the signal is given by charge of electrons absorbed in the wire. On the other hand, for higher beam energies and unpolarized wire the balance between the SE generated by the particles crossing the wire and the electrons absorbed in the wire may result in an almost null signal.

Therefore, the best way to measure H^- beams above 100 MeV with a 33 μm carbon wire is to bias the wires and expect the signals of Table 4.9.

In conclusion, according to these simulations (at 50 and 160 MeV beam energy), tungsten wires guarantee enough signal at all LINAC4 energies, whereas carbon wires may give little signal at energies above 100 MeV.

The consideration on the signal level on the SEM grid can be applied for the WBS. The design from LPI has to be changed, the two wires have to be separated to avoid cross talk and coupling in the measurement of the beam profile in the both planes.

It is interesting to note that the values found for the backscattering coefficient are compatible with the experimental data [35], [36].

4.4.3 Expected wire temperature

In order to estimate the maximum wire temperature it was assumed that the central wire does not move for 10 LINAC4 pulses, while considering three different beam currents and beam pulse lengths combinations. The simulations was performed for a 1 mm \times 2 mm RMS beam sizes and using Eq. 4.6 and Eq. 4.8. the results for a 33 μm carbon and 40 μm tungsten wires are shown in Table 4.10, the one for 100 μm wires in Table 4.11.

The two tungsten wires (40 and 100 μm) would not stand the full beam length,

E [MeV]	$I = 70mA, t = 400 \mu s$		$I = 40mA, t = 400 \mu s$		$I = 70mA, t = 100 \mu s$	
	carbon	tungsten	carbon	tungsten	carbon	tungsten
50	3944	10390	2518	6350	1430	3100
57	3619	9500	2331	5842	1346	2880
79	2946	7900	1943	4768	1165	2410
86	2800	7490	1859	4527	1124	2303
100	2567	6806	1723	4136	1060	2131
115	2376	6242	1612	3814	1005	1990
129	2235	5822	1528	3574	964	1884
145	2105	5435	1328	3352	926	1786
160	2006	5136	1393	3182	897	1710

Table 4.10: Maximum temperature in Kelvin for a $33 \mu m$ carbon wire and a $40 \mu m$ tungsten wire, when the wire stays at beam core from 10 LINAC4 pulses and with $1 mm \times 2 mm$ beam.

E [MeV]	$I = 70mA, t = 400 \mu s$		$I = 40mA, t = 400 \mu s$		$I = 70mA, t = 100 \mu s$	
	carbon	tungsten	carbon	tungsten	carbon	tungsten
50	4215	10868	2781	6550	1672	3300
57	3887	9990	2591	6042	1581	3078
79	3212	8110	2198	4968	1390	2605
86	3065	7692	2120	4728	1347	2500
100	2830	7007	1972	4336	1277	2326
115	2636	6443	1857	4014	1218	2184
129	2493	6023	1772	3773	1173	2077
145	2362	5635	1693	3552	1131	1978
160	2261	5337	1631	3380	1098	1902

Table 4.11: Maximum temperature in Kelvin for a $100 \mu m$ carbon and tungsten wire, when the wire stays at beam core from 10 LINAC4 pulses and with $1 mm \times 2 mm$ beam.

when the beam intensity is $70 mA$, for which the melting point of tungsten would be exceeded at all the instrument positions. When the beam intensity is reduced to $40 mA$, the melting point is not reached only for high energy beams, but the maximum temperature remains very close to the melting temperature.

In case of a carbon wire, the maximum temperature is far below the sublimation point with the nominal beam, whereas with the commissioning beam the temperature is above the sublimation point at 50 and 57 MeV.

Emitted current due to thermionic emission

Table 4.12 shows the maximum emitted current due to thermionic emission for a 100 μm diameter wire.

E [<i>MeV</i>]	<i>I</i> = 70 <i>mA</i> , <i>t</i> = 400 μs		<i>I</i> = 40 <i>mA</i> , <i>t</i> = 400 μs		<i>I</i> = 70 <i>mA</i> , <i>t</i> = 100 μs	
	carbon	tungsten	carbon	tungsten	carbon	tungsten
50	sublim.	melt.	1.10E-05	melt.	1.90E-11	melt.
57	sublim.	melt.	2.40E-06	melt.	2.90E-12	2.60E-05
79	1.76E-04	melt.	5.00E-08	melt.	2.60E-14	7.11E-06
86	7.42E-06	melt.	1.80E-08	melt.	7.50E-15	2.24E-07
100	1.54E-06	melt.	2.77E-09	melt.	8.31E-16	8.75E-08
115	3.50E-06	melt.	5.00E-10	melt.	1.00E-16	3.17E-09
129	1.03E-06	melt.	1.18E-10	melt.	2.00E-17	8.27E-10
145	3.00E-07	melt.	2.80E-11	melt.	3.71E-18	2.11E-10
160	1.00E-07	melt.	8.30E-12	melt.	9.00E-19	6.73E-11

Table 4.12: Thermionic current emitted from the wire(values in Ampere)

In the worst case for both tungsten and carbon wires, the maximum thermionic current ranges from 1 % to 10 % of the expected current, depending on the beam parameters. For a carbon wire the emitted current is not an issue for the measurements above 60 *MeV* for the nominal beam, and is negligible at all beam energies for the shortest pulse length. In case of a tungsten wire, the measurement is not perturbed above 80 *MeV*.

As discussed above the thermal electrons have low energy and are repelled to the wire by a bias voltage of the order of 100 *V*. With such a bias, thermionic emission can be avoided for all instruments independently of the wire material.

4.5 Chopper line Wire Beam Scanner

The beam sizes at the two wire scanner locations are summarized in Table 4.13.

	Wire scanner 1	Wire Scanner 2
σ_x [<i>mm</i>]	3.52	3.77
σ_y [<i>mm</i>]	3.07	1.77

Table 4.13: Nominal beam sizes at the wire beam scanner location in the chopper line

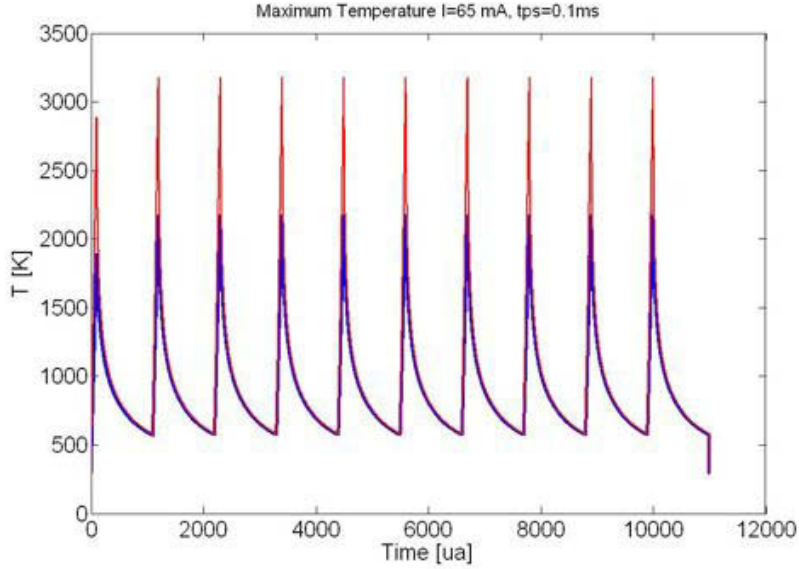


Figure 4.14: Maximum temperature on a carbon wire for the WBS1 (blue curve) and WBS2 (red curve) in case of a beam pulse length of $100 \mu s$ and a beam intensity of $65 mA$.

From previous results, due to the better signal at $3 MeV$ and the lower thermal load, $33 \mu m$ diameter carbon wire has been chosen for the both WBS.

4.5.1 Wire heating

Different pulse length and beam intensity have been simulated, the results are shown in Table 4.14. Fig. 4.14 and Fig. 4.15 show the evolution of the temperature on the wire along several pulses for a pulse length of $100 \mu s$ and a beam intensity of $65 mA$.

Intensity [mA]	65	65	65	40	40
Pulse length [μs]	50	100	400	100	400
Tmax wbs 1 [K]	1359	2175	6983	1550	4520
Tmax wbs 2 [K]	1871	3178	div	2174	7000
$I_{therm.}$ wbs 1 [A]	1.00E-14	4.10E-08	subl.	1.50E-12	subl.
$I_{therm.}$ wbs 2 [A]	6.80E-10	1.70E-04	subl.	4.30E-08	subl.

Table 4.14: Temperature in Kelvin on the wire on the two WBS of the chopper line

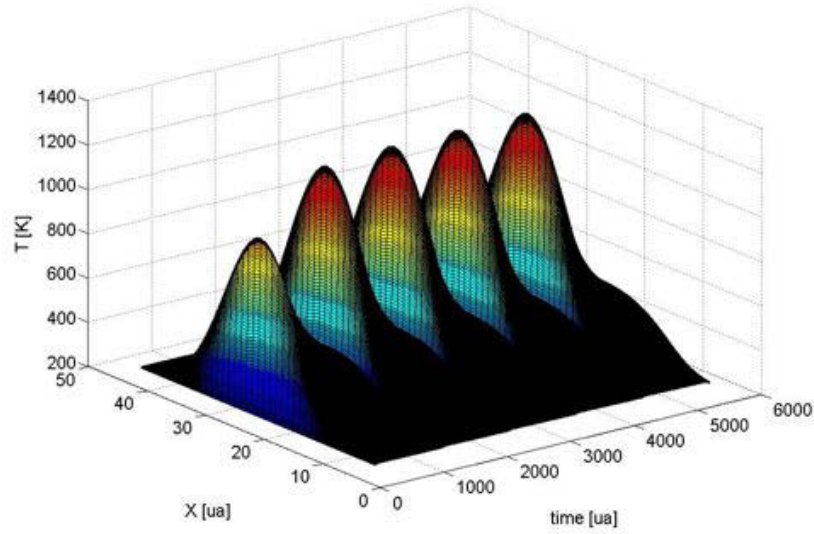


Figure 4.15: Temperature profile along wire for several beam pulse on a the carbon wire of the WBS1 (beam pulse length of $100 \mu s$ and a beam intensity of $65 mA$).

The equilibrium is reached after 3 pulses and the temperature decrease to 600 K between two pulses. The maximum temperature after the third cooling period is almost constant for all the scenarios without damage to the wire. At this energy, the wire will destroy with the full pulse length. In order to preserve the wire integrity, the pulse length must to be reduced to $100 \mu s$, nevertheless, for the wire beam scanner 2 the temperature is close to the sublimation point and in case of $65 mA$ and $100 \mu s$ pulse length beam, the sublimation rate of the wire is important for the wire beam scanner 2. At $3200 K$, from Eq. 4.15 the time needed to sublimate $1 \mu m$ of carbon is around 100 seconds; the wire will be destroyed in a few minutes. The intensity should be reduced to $40 mA$, to preserve the wire .

The thermionic emission is negligible for the two scenario, which can be used for the integrity of the wire ($65 mA$ an $50 \mu s$ beam pulse or $40 mA$ and $100 \mu s$ beam pulse), in the worst case the emitted current is around $43 nA$. Nevertheless a polarization can be applied on the wire and avoid this effect and increase the signal.

4.5.2 Expected current

The charge deposition on a $33 \mu m$ diameter carbon wire has been calculated for the SEM grid of the emittance meter. For these monitors, a bias voltage on the wire cannot be applied, for the two wire scanner the polarization is available

Intensity [mA]	40	65
I max wbs 1 [mA]	-0.35	-0.571
I max wbs 2 [mA]	-0.6	-0.97

Table 4.15: Maximum expected signal at WBS1 and WBS2.

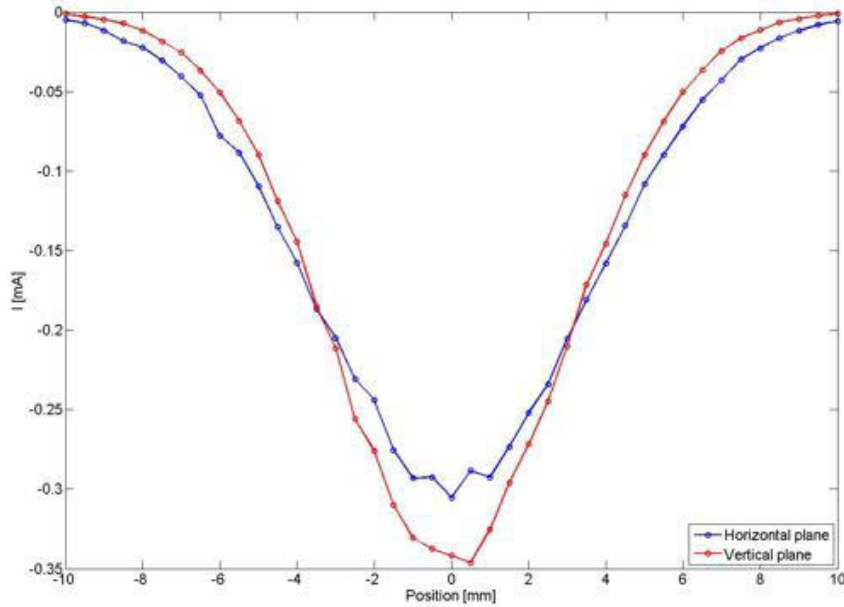


Figure 4.16: Simulation of beam profile measurement with the WBS1.

and the charge deposition will be equal to -2. With the beam parameters given in Table 4.13, the maximum intensity can be calculated, the results are shown in Table 4.15.

The maximum current is far from the noise level, the profile could be reconstructed with a good accuracy. The wire scanner is moved by the stepping motor, the resolution can be increased with a smaller step of the motor, the limit is the wire diameter. Fig. 4.16 and Fig. 4.17 show a simulation of a scan from -10 to 10 mm (with respect to the beam axes) with 0.5 mm step for the two wire scanner.

The simulations have been done with Gaussian beam. A step size of 0.5 mm is enough to reconstruct with a good precision both transverse profiles at the wire beam scanner 1 and the profile of the horizontal plane for the other scanner. The step should be reduced for the measurement at the wire beam scanner 2. The range of the scan is too short. For a real measurement the range should be increased to measure the tail of the beam.

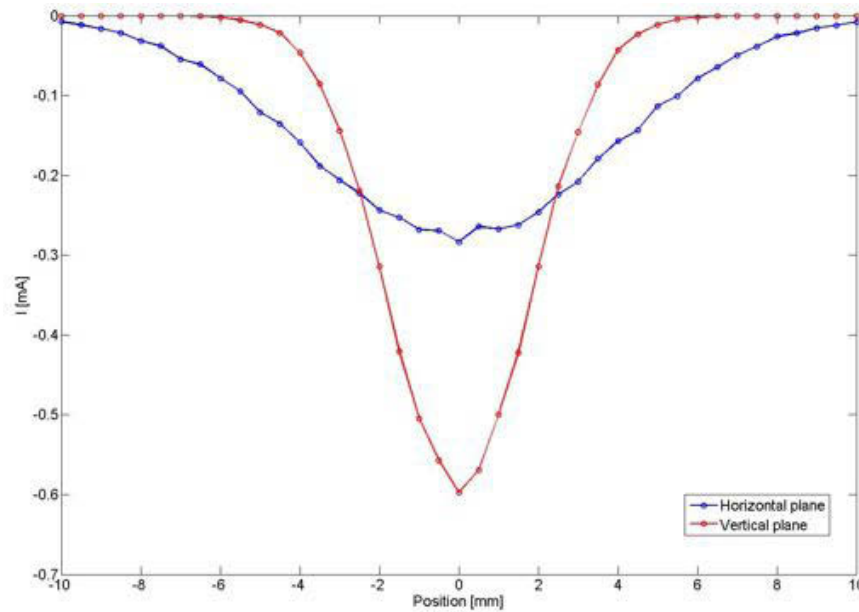


Figure 4.17: Simulation of beam profile measurement with the WBS2.

4.6 Conclusion

For the SEM grid installed in the test bench, the increase in temperature is not an issue, most of the beam power will be stopped in the slit. The calculations show a higher signal for a carbon wire at 3 MeV, this material is also well suited for the measurement at 12 MeV. In the case of tungsten wire, the signal is too low at 3 MeV, and the emittance reconstruction or the measurement of the energy spread could be difficult with a large error on the results.

In the linac, the results show a major problem with the temperature increase. In order to have enough signal for profile measurement and prevent any damage, a carbon wire with a diameter of 100 μm is the only solution to measure the full beam intensity with enough signal. But carbon wires with this diameter are not available, the signal provided by 33 μm diameter carbon wires decreases strongly at high energy (above 100 MeV). tungsten wires are not able to stand the full LINAC4 beam power, this solution will provide an accurate measurement of the beam profiles with a good signal over noise ratio at all LINAC4 energies. Two solutions can be proposed:

- Use tungsten wires in all the linac and operate at lower power (40 mA and 100 μs).
- Use carbon wires below 100 MeV with full beam power and tungsten wires

above this threshold at low power.

It is interesting to measure the full pulse length at low energy and for the commissioning phase, the second solution is possible if there is no conflict with the machine protection system.

In the chopper line, the thermal load is even higher, carbon wires can only stand one fourth of the total beam power at this position, these two equipments must be commissioned carefully to avoid any breaking wire and determine the limits.

Chapter 5

Emittance measurement with a slit and grid system

5.1 Method

The transverse phase-spaces describe the distribution of particles in x and x' (y and y'), where x (y) is the position of the particles and x' (y') the angle between the transverse position of the particle and the longitudinal coordinate (z).

For low energy linear accelerators, a typical method for measuring the transverse emittance consists in a slit and grid system, as schematically shown in Fig. 5.1 and Fig. 5.2. For each slit position, the narrow aperture allows the passage of a beamlet populated by particles that have an almost equal position x and a certain angular distribution. Due to the phase space rotation in the following drift space, the beamlet angular distribution is transformed into a position distribution and sampled using a profile monitor, in our case a wire grid. Therefore, the profile measurement gives the angle x' (y') for a certain position x (y) and by scanning the slit across the beam, the whole phase-space can be reconstructed.

In order to sample both transverse planes, two slits and two grids are needed. The angular resolution of the system is determined by the profile monitor resolution (e.g. the wire distance) and the drift length, which modifies the phase space rotation.

The slit geometry and material affect the measurement accuracy. A number of particles will be scattered on the slit aperture edges and the slit aperture width biases the phase space sampling by introducing an angular cut. The larger the aperture, the smaller the cut.

At low energies, the space charge effect (see Chapter 2) has a strong influence on the beam dynamics. In particular, along each drift space the space charge forces induce an emittance increase.

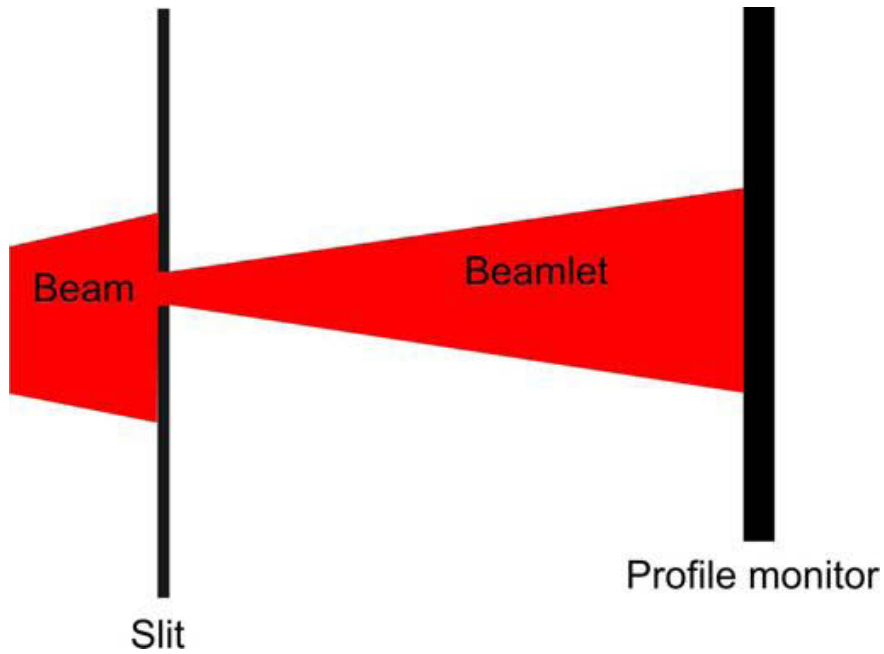


Figure 5.1: Slit and grid system schematic diagram

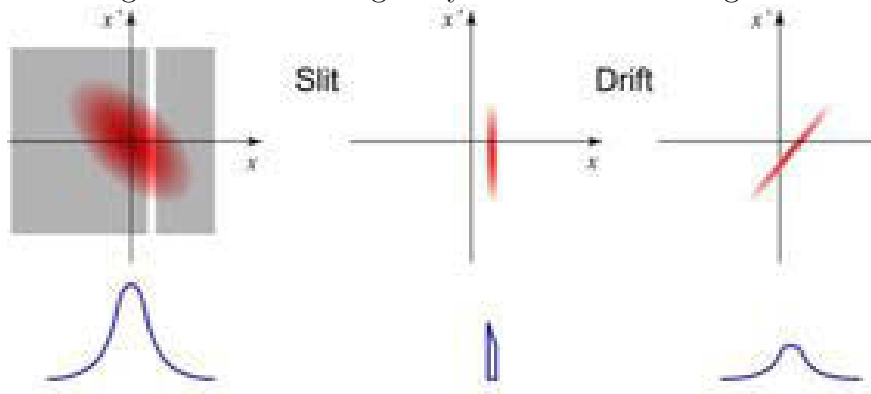


Figure 5.2: Phase-space sampling using a slit and grid system (sampling of the beam divergence after the beamlet rotation in phase space along the drift from the slit to the profile monitor)

All these aspects, related to the slit and grid emittance measurement resolution and accuracy, will be discussed in the next sections considering the design of the LINAC4 test bench emittance meter that will be equipped with:

- Two slits (1 per plane) movable with stepping motors
- Two grids with 48 wires each, installed 3.5 m from the slits, also movable

with stepping motors. The wire distance will be $750 \mu m$ and the beamlet profile monitoring resolution will be enhanced by scanning several grid positions for each slit position.

The emittance meter will be used at 3 commissioning stages:

- RFQ at a beam energy of $3 MeV$
- MEBT at a beam energy of $3 MeV$
- DTL at a beam energy of $12 MeV$

5.2 Effect of the slit design parameters on the emittance measurement accuracy

5.2.1 Slit aperture

For each transverse coordinate (i.e. x and y), the particles distribution in phase space (x, x') is described by the Courant-Snyder invariant (or Twiss parameters) $\epsilon, \alpha, \beta, \gamma$ (see Chapter 3 for more details). The phase space distribution and the values defined by the Twiss parameters are represented in Fig. 5.3.

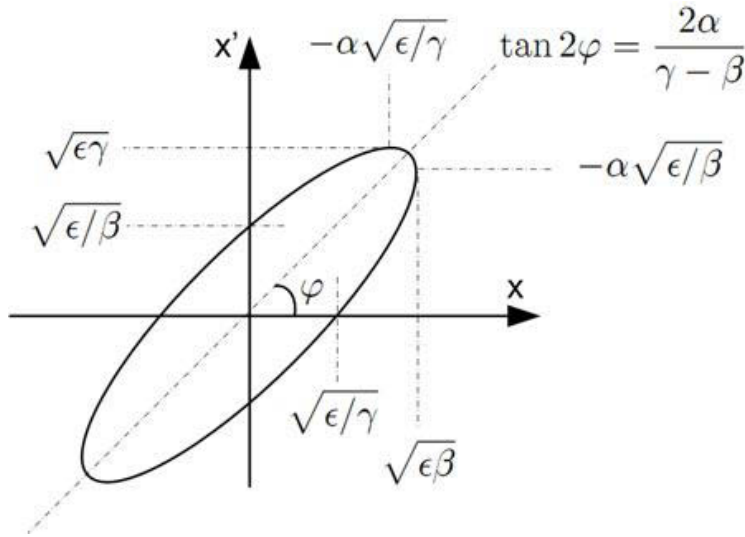


Figure 5.3: Phase space ellipse and Twiss parameter meaning.

The emittance can be calculated by :

$$\epsilon = \gamma x^2 + 2\alpha x x' + \beta x'^2 \quad (5.1)$$

In addition, α , β , γ are related by:

$$\gamma = \frac{1 + \alpha^2}{\beta} \quad (5.2)$$

As discussed in Chapter 2, in an adiabatic system, ε is not constant at the different linac locations, only the normalized emittance $\varepsilon_{norm} = \beta_{rel}\gamma_{rel}\varepsilon$ is constant. At $x=0$ the beam divergence is $\sqrt{\frac{\varepsilon}{\beta}}$. The finite slit aperture $\Delta x > 0$ leads to an increase of the beamlet divergence, that can be calculated from Eq. 5.2 and Eq. 5.3 results:

$$\frac{\Delta x'}{\Delta x} = \frac{-\alpha}{\beta} \quad (5.3)$$

Consequently, for a slit aperture $\Delta x = e$, the error on the divergence is $\Delta x' = \frac{-\alpha e}{\beta}$. The emittance error can be derived from Eq. 5.1 and reads:

$$\frac{\Delta \varepsilon}{\varepsilon} = \Delta x' \frac{1}{\sqrt{\frac{\varepsilon}{\beta}}} = \frac{-\alpha e}{\beta} \frac{1}{\sqrt{\frac{\varepsilon}{\beta}}} \approx \frac{\alpha e}{\sqrt{\beta \varepsilon}} \approx \frac{\alpha e}{\sigma} \quad (5.4)$$

Where $\sigma = \sqrt{\beta \varepsilon}$ is the RMS beam size. The equation shows that the error scales to the ratio $\frac{\alpha}{\sigma}$.

The values of the Twiss parameters at the slit locations foreseen for the three LINAC4 test bench stages are shown in Table 5.1. The last row of the table, indicates the predicted emittance error due to a slit aperture $e=200 \mu m$.

Location	RFQ		MEBT		DTL	
	H	V	H	V	H	V
Plane						
α	-0.58	0.02	1.35	-0.13	-0.39	-0.26
β [m/rad]	17.65	2.17	3	2.2	0.63	1.23
$\varepsilon_{norm.}$ [$\pi.mm.mrad$]	0.26	0.27	0.3	0.31	0.3	0.31
ε [$\pi.mm.mrad$]	3.25	3.27	3.50	3.87	1.87	1.93
Beam width [mm]	17	6	10	6.5	3.6	3.5
$\frac{\Delta \varepsilon}{\varepsilon}$ [%]	1.2	0.1	7.41	0.70	6.40	2.80

Table 5.1: Typical beam parameter expected during the commissioning phase of the low energy part of the LINAC4 (up to 12 MeV).

For each location the horizontal plane is the most critical. At the MEBT and DTL locations, the predicted error is above 6 %. With a slit aperture $e=100 \mu m$, the error would be below 3.7 %, but such a small gap would worsen the signal over noise level at the wire grids. It has to be noted that this method of error calculation gives a maximum error.

5.2.2 Slit thickness

Also the slit thickness along the beam trajectory coordinate (z) affects the measurement accuracy, due to the angular cut that is introduced. Fig. 5.4 shows the maximum particle angle θ_{cut} after the slit as function of the slit thickness (for a slit aperture of $100\ \mu\text{m}$), as calculated with the simple formula:

$$\theta_{cut} = \frac{\text{half aperture}}{\text{slit thickness}} \quad (5.5)$$

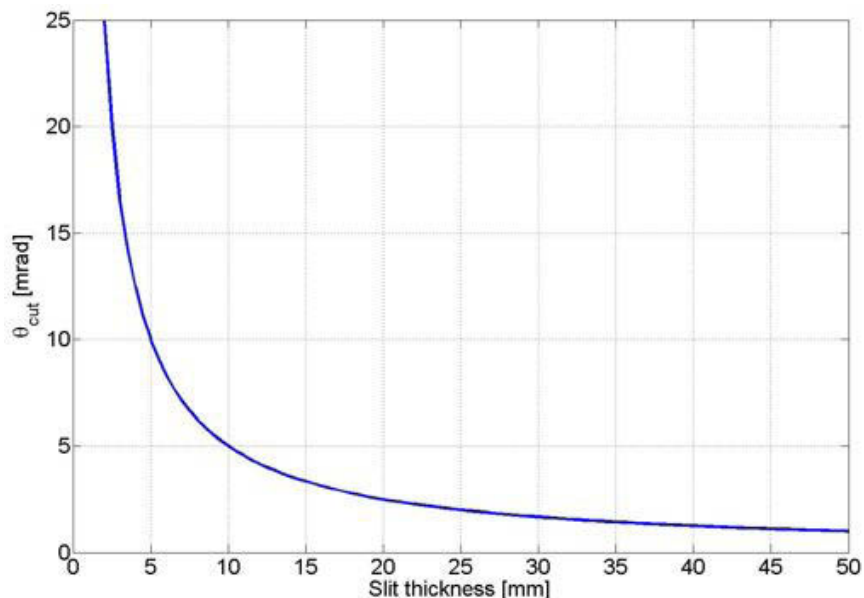


Figure 5.4: Angle vs slit thickness

Since during the commissioning phase a maximum beamlet divergence of $8\ \text{mrad}$ is expected, the slit thickness must be less than $5\ \text{mm}$, allowing a measurement of angles up to $10\ \text{mrad}$. The minimum thickness depends on the slit material, a thickness of two times the range of protons inside the slit material is a conservative choice. Graphite has been chosen for the slit material. The various studies that have led to this choice are described in Chapter 6. Since the range of a $12\ \text{MeV}$ proton beam in Graphite is around $1\ \text{mm}$, a minimum thickness of $2\ \text{mm}$ is convenient.

5.3 Profile Monitor resolution

As already mentioned above, for each transverse plane a SEM grid monitor (see Chapter 4) will be used as profile detector. The monitor will be installed

3.5 *m* downstream of the slit and the 48 wires will be separated by 750 μm . Each SEM grid is moved by a stepping motor and for every slit position, the emittance measurement resolution can be improved by moving the grid by small steps around the position of the slit aperture.

The particle tracking code PATH [33] has been used to simulate the system, by tracking the particle beamlet from the slit to the grid for different combinations of the slit and grid transverse positions necessary to complete an emittance measurement.

Beam distribution at the SEM grid (Hor. ε measurement)			
	RFQ	MEBT	DTL
Δx (5 rms) [mm]	± 4	± 11	± 17
Δx (5 rms) [mm]	± 13.5	± 17	± 15
Beam distribution at the SEM grid (Vert. ε measurement)			
	RFQ	MEBT	DTL
Δx (5 rms) [mm]	± 22	± 10	± 20
Δx (5 rms) [mm]	± 10	± 12	± 12

Table 5.2: Full beam width at the SEM grid location in case of emittance measurement with the slit inserted in the beam pipe.

Table 5.2 summarizes the values of the vertical and horizontal beam width, calculated as 5 times the RMS of the projected distributions.

Given the 48 wires separated by 750 μm , the sensitive area of SEM Grids in the measurement plane is 36 mm. Therefore, from the values in the table, it can be inferred that a single grid position is not enough to measure the full beamlet divergence. Two grid positions at each slit location, with a step of 36 *mm* to avoid overlapping, results in an equivalent sensitive area of 72 *mm* and solve the problem. The wire length is 80 *mm* and covers the full sensitive area in the non-measurement plane. As can be seen from Table 5.2, this is enough in all cases.

Ideally, a Gaussian distribution can be reconstructed by sampling 2 points per sigma [37] and applying the proper fit. The distributions that will be measured at the LINAC4 test bench, will not be necessarily Gaussian and the beamlets divergence, will be calculated as the RMS of the measured profiles. We consider that enough accuracy will be guaranteed if at least 3 wires per RMS width will give a signal.

In almost all the test bench cases, this criterion is verified since the number of wires per RMS width varies from 5 to 9 depending on the slit position and the measurement plane. The only exception is the horizontal measurement after the RFQ, for which only 2 wires per RMS width are hit by the beamlet particles, when

considering the nominal beam parameters. The resolution must be improved, by moving the SEM grid with small steps. A dedicated simulation proved that with $250\ \mu\text{m}$ SEM grid steps, it is possible to achieve 6 hit wires per RMS width.

What presented so far refers to the case with the slit at the central position, when the beamlet divergence is maximal. As the slit moves to the beam tails, the beamlet divergence and the signal over noise ratio decrease. As a consequence, a number of grid steps for each slit position are required to achieve enough resolution and accuracy. In addition, on the tails the average beamlet divergence is different from zero and this requires additional grid steps in order to provide an equivalent grid sensitive area of $108\ \text{mm}$.

5.4 Effect of the space charge on emittance reconstruction

5.4.1 Method

A beam size increase due to space charge effects along the drift from the slit to the grid can perturb the emittance reconstruction. Since the space charge effect is proportional to beamlet current, the larger the slit aperture, the bigger the measurement perturbation. The space charge effect is also proportional to the particle density, smaller beam sizes result in a higher beamlet intensity through the slit and consequently a higher emittance increase along the drift.

Such an effect has been simulated with the particle tracking code PATH [33], starting from the beam parameters shown in Table 5.1, from where it can be seen that, with respect to the beam size, the worst case is for the measurements at the MEBT. For this reason the MEBT case was simulated with two different particle densities. As shown in Table 5.3, the nominal beam parameters have been used in the setting MEBT, while for the other setting, MEBTII, the β is smaller. Only the results for the horizontal plane will be presented in this chapter, but all results can be applied to the vertical plane as well.

PATH has been used to generate perfectly Gaussian distributions at the slit location, considering 2.5×10^6 particles for the RFQ, MEBT and DTL cases and 10^6 for the MEBT II case. PATH has been setup with a perfect slit (no scattering, no angular cuts), the $3.5\ \text{m}$ drift space and a scoring plane at the grid location. Two slit apertures have been simulated ($e=100\ \mu\text{m}$ and $e=200\ \mu\text{m}$) for all the cases, except for the RFQ position, where only the larger aperture has been simulated in order to avoid statistical bias due to the small number of particles reaching the profile detector. The slit scans have been simulated by displacing the beam at the slit location. With 21 steps, it was guaranteed to have at least 4 slit positions per sigma. For each slit position, the beamlet has been tracked and scored at

Setting	MEBT	MEBTII
α	1.35	1.35
β [m/rad]	3	1.15
Norm. ε_{rms} [$\pi.mm.mrad$]	0.28	0.28
ε_{rms} [$\pi.mm.mrad$]	3.5	3.5
Beam width [mm]	10	6

Table 5.3: Beam parameters used for the PATH simulations at 3 MeV. The Twiss parameters used for vertical plane are shown in Table 5.1

the grid location with and without space charge effects, which allows determining the ultimate precision of the measurement without perturbation from scattering processes. Regardless of the number of tracked particles, PATH simulates space charge according to the total beam intensity that is given as an input, 65 mA for these studies. The beamlet distributions scored at the grid location have been fed to a MATLAB routine designed to reconstruct the RMS emittance according as:

$$\varepsilon_{rms} = \sqrt{\langle x^2 \rangle \langle x'^2 \rangle - \langle xx' \rangle^2} \quad (5.6)$$

where x is the slit position and x' is calculated from the particle position on the screen.

5.4.2 Phase space reconstruction with an infinite resolution monitor

In addition to the position of particles on the screen, PATH provides the angle of trajectory. These values have been used to reconstruct the beam emittance, instead of sampling the beamlet profile, in order to achieve a simulation of the measurement with a quasi perfect angular resolution for the monitor. As discussed above, a maximum slit aperture of 200 μm allows keeping the emittance reconstruction error due to angular cuts below 10 %. The study has been carried out for the RFQ, MEBT and DTL cases (see Table 5.1) and for the MEBT II case (see Table 5.3), only considering the horizontal emittance measurement.

The simulations results with and without space charge effects are summarized in Table 5.4 and Fig. 5.5. For each case, the reconstructed emittance is compared to the reference value. Such a reference value corresponds to the normalized RMS emittance as calculated from the particle distributions generated at the slit location.

Without space charge, the emittance reconstruction error is below 0.3 % for all cases. For the MEBT case the effect of doubling the slit aperture is within

ε_{ref} [π .mm.mard]	RFQ	MEBT	DTL	MEBTII				
	0.26	0.28	0.3	0.28				
Without space charge								
slit aperture [μ m]	ε	$\frac{\Delta\varepsilon}{\varepsilon_{ref}}$ [%]						
100	–	–	0.28	0	0.30	0.1	0.28	0.07
200	0.26	0.11	0.28	0	0.30	0.23	0.28	0.18
With space charge								
slit aperture [μ m]	ε	$\frac{\Delta\varepsilon}{\varepsilon_{ref}}$ [%]						
100	–	–	0.29	3.71	0.30	1.9	0.29	3.07
200	0.28	6.20	0.30	7.43	0.31	3.53	0.30	6.18

Table 5.4: Emittance reconstruction values as simulated with and without space charge for 4 different beam parameters and two slit apertures.

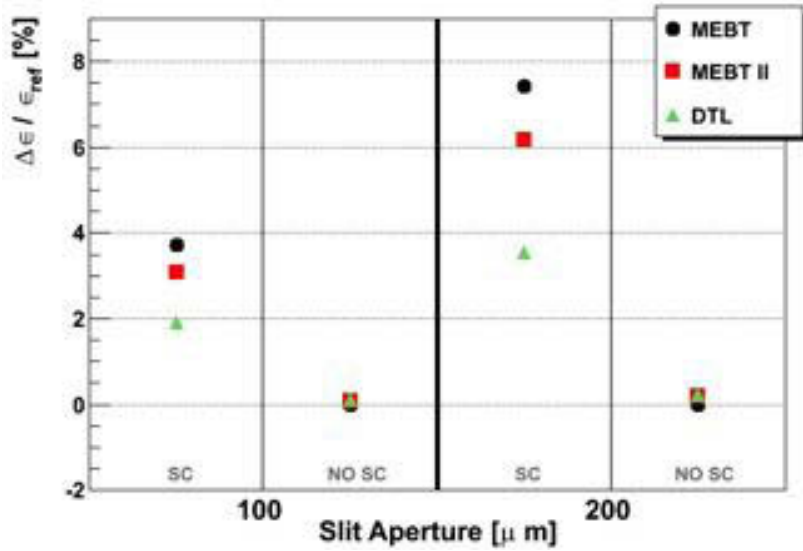


Figure 5.5: Emittance reconstruction error due to space charge, considering two slit apertures (data from table 5.4).

the statistical error of the simulations (the emittance for $e=100 \mu m$ is larger than the one for $e=200 \mu m$). For the DTL case, doubling the aperture results in a double emittance error, as predicted by Eq. 5.4, even though the absolute value is different from the analytical calculations. The rotation of the beamlet in phase space induced by the long drift is around 45° and the beamlet size is larger than $20 mm$ (full width). In these cases, the effect of the slit aperture on the

measurement is reduced by the large difference between the slit aperture and the beamlet size and by the beamlet rotation (when the rotation is 90° , the error due to the aperture is 0).

These simulations show that the slit aperture has a linear influence on the error, increasing the slit aperture by a factor 2 implies also an increase of the error by a factor 2. In the worst case, at 3 MeV the error on the emittance reconstruction is about 7.5 %.

A dedicated tracking simulation without space charge activated has been done to estimate the beamlet particles density along the drift space and consequently the space charge forces at 3 MeV . The sources have been generated with 5×10^5 particles and the same beam parameters as above. The slit is positioned at the center of the beam to reduce the statistical error, the horizontal position of the particle beamlet has been scored every 50 cm from $z=0$ (slit position) to $z=350\text{ cm}$ (profile detector position). The results are shown in Fig. 5.6.

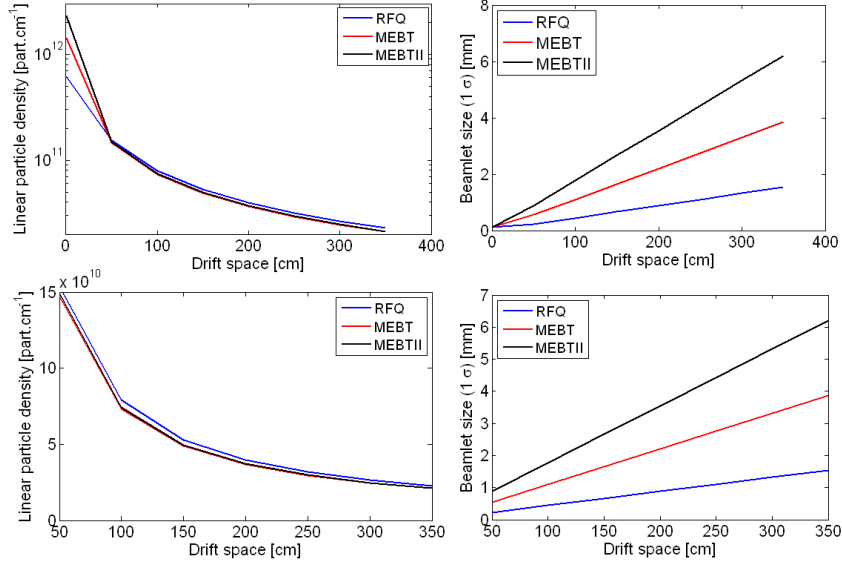


Figure 5.6: Linear particle density and beamlet size along the drift space between the slit and the profile monitor for the 3 MeV cases

At the slit position, compared to the RFQ case, the particle density for the MEBT and MEBTII cases is a factor 1.6 and 3.8 larger. In the drift space the densities are almost the same, even more the highest particle density is obtain in the RFQ case.

As the emittance remains almost constant in these cases, reducing the beam size implies an increase of the beam divergence. With the larger beam size, the RFQ beam has also the smallest divergence (the standard deviation of the particle angular distribution is around 0.44 mrad).

The opposite is obtained in the MEBTII case ($\sigma_{x'} = 1.8 \text{ mrad}$). Therefore the beamlet size increases quickly in the case of the MEBTII during the drift between the slit and the profile monitor, while in RFQ case, this growth is reduced by a factor 4 (w.r.t. the MEBTII case), which corresponds to the difference in density at the slit location. Similar conclusions can be done for the MEBT case. The space charge forces are proportional to the particle density that is similar in all the cases and leads to a similar error for the emittance reconstruction.

The beamlet divergence is almost independent of the slit aperture for apertures smaller than $300 \mu\text{m}$. Increasing the slit aperture leads to an increase in the beamlet particle density without increasing the beamlet sizes.

For the DTL, even though the beam energy is higher (space charge diminishes with energy), the higher particle density yields to a space charge emittance increase in the order of 2 % and 3.5 % for the two slit apertures respectively.

5.4.3 Effect of the monitor resolution on the phase space reconstruction

In the next sections, the RFQ case has not been studied. The small amount of particles passing through the slit and the sampling used for the different studies lead to a statistical error larger than the systematic effects. Nevertheless the results presented above allow us to extrapolate the result for RFQ from the two 3 MeV cases.

Until now, the profile monitor was assumed to have infinite resolution. This section discusses the uncertainties related to the finite sampling of the transverse distribution by means of a SEM wire detector. In the simulation, the particles scored at the monitor location are grouped in bins with width and distance equal to the wire diameter and distance. The particles angle in phase space x is then calculated using the bin (wire) center position x according to:

$$x' = \frac{x}{d} \tag{5.7}$$

where $d=3.5 \text{ m}$ is the distance between the slit and the monitor. The following binning configurations were simulated:

- $50 \mu\text{m}$ wide bins, one contiguous to the other, covering the all profile
- $50 \mu\text{m}$ wide bins separated by $250 \mu\text{m}$
- $50 \mu\text{m}$ wide bins separated by $750 \mu\text{m}$

In case of poor resolution (i.e. few wires hit per RMS beam size) it is possible to have systematic errors due to the relative transverse position between beam and SEM grid. For this reason, starting from the same initial distribution (from

reconstructed emittance without space charge						
MEBT				MEBTII		
pitch [μm]	mean ε	$\frac{\Delta\varepsilon}{\varepsilon}$ [%]	$std(\varepsilon)$	mean ε	$\frac{\Delta\varepsilon}{\varepsilon}$ [%]	$std(\varepsilon)$
50	0.28	0.1		0.28	0.14	
250	0.28	0.1	7.510^{-4}	0.28	0.14	610^{-4}
750	0.28	0.1	10^{-3}	0.28	0.14	10^{-3}
reconstructed emittance with space charge						
MEBT				MEBTII		
pitch [μm]	mean ε	$\frac{\Delta\varepsilon}{\varepsilon}$ [%]	$std(\varepsilon)$	mean ε	$\frac{\Delta\varepsilon}{\varepsilon}$ [%]	$std(\varepsilon)$
50	0.29	3.9		0.29	3.1	
250	0.29	3.9	3.210^{-4}	0.29	3.1	6.710^{-4}
750	0.29	3.9	0.910^{-3}	0.29	3.1	1.410^{-3}

Table 5.5: Reconstructed emittance at 3 MeV for different SEM grid pitch and a slit aperture of 200 μm .

PATH) and using the same 50 μm binning, the simulations have been repeated varying the selected bins. For example, in the case of a grid with 250 μm pitch:

- The first bin has been placed at -50 mm.
- to simulate the grid, 1 every 5 bins have been considered starting from the first bin.
- The same calculation has been done starting from the second bin and so on until the first bin corresponds to the second wire in the first iteration.
- This process has been redone starting with the first bin at -49.99 mm, until a complete bin has been covered.

The same has been repeated for a grid pitch of 750 μm , for which 1 bin every 15 has been considered. The present design of the LINAC4 measurement bench wire grids foreseen 33 to 40 μm diameter wires separated by 750 μm .

The results of the simulations in terms of reconstructed emittance are shown in Table 5.5, Table 5.6 and Fig. 5.7, when considering a slit with 200 μm aperture, with and without space charge. The error $\frac{\Delta\varepsilon}{\varepsilon}$ is with respect to the nominal emittance and the standard deviation $std(\varepsilon)$ results from the iterations described above (sampling uncertainty).

The error due to the pitch is negligible, as expected from the geometrical calculation. Compared to a perfect monitor, the emittance reconstruction with space charge is not well reconstructed, the error due to sampling is about 4 %. Compared to the previous simulation, the angle is calculated from the center of the

reconstructed emittance without space charge			
pitch [μm]	mean ε	$\frac{\Delta\varepsilon}{\varepsilon}$ [%]	$std(\varepsilon)$
50	0.30	0.27	
250	0.30	0.27	7.410^{-4}
750	0.30	0.27	1.310^{-3}
reconstructed emittance with space charge			
pitch [μm]	mean ε	$\frac{\Delta\varepsilon}{\varepsilon}$ [%]	$std(\varepsilon)$
50	0.31	1.93	
250	0.31	1.90	6.710^{-4}
750	0.31	1.90	1.210^{-3}

Table 5.6: Reconstructed emittance for the DTL case for different SEM grid pitch and a slit aperture of $200 \mu\text{m}$.

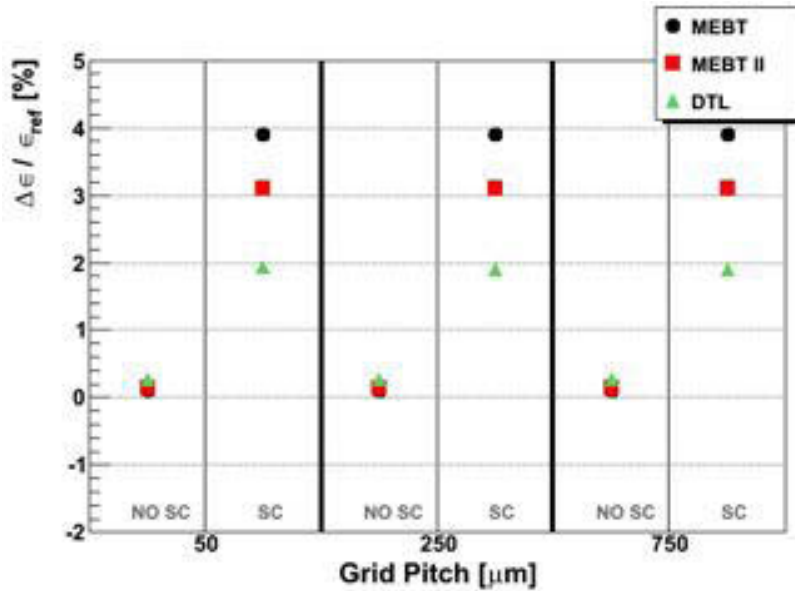


Figure 5.7: Emittance reconstruction error due to space charge, considering three SEM grid pitch (data from table 5.5).

bin and the particles within this bin have considered with the same angle. This implies that a small displacement on the screen (deviation less than $25 \mu\text{m}$, i.e. an angle of $7 \mu\text{rad}$) due to space charge force is not detected by the grid.

As shown in the section about the perfect monitor, reducing the aperture of the slit by a factor 2 leads to a reduction of the error by the same factor. For a slit aperture of $100 \mu\text{m}$, the errors on the reconstructed emittance are:

- $\approx 2\%$ for the MEBT case.
- $\approx 1\%$ for the DTL case.
- $\approx 1.5\%$ for the MEBTII case.

5.5 Effect of scattering and stripping at the slit

5.5.1 Signal

The Monte Carlo simulation package FLUKA [32] has been used to study the effect of particles scattering along the slit aperture. The same particle distributions as the ones used for the tracking studies above have been fed to the FLUKA model, consisting of a graphite slit with an aperture of 100 or 200 μm and a thickness of 3 mm . The FLUKA output scoring on the screen has then been used for the emittance reconstruction, more details about FLUKA simulations are presented in Chapter 6.

Due to the low H^- energy, all scattered particles reaching the profile monitor can be considered as fully stripped. This is relevant, since at 3 and 12 MeV , the H^- signal on the wires is dominated by the charge deposition of the two electrons, for which scattered particles do not contribute.

In fact, for 3 MeV ions, the average kinetic energy of the scattered particles is about 2 MeV and the protons are stopped in the carbon wire. In this case the wire signal is given by secondary emission at the surface and direct charge deposition of the proton. The charge creation is +1.75 electrons per proton hitting the wire (for an H^- ion the charge is -1.20 e). The signal has an opposite polarity compared to the signal generated by a non scattered H^- ions, and almost the same absolute value.

At 12 MeV , the average energy of the scattered particles is around 8.5 MeV and the protons have good probability of exiting the wire. In this case, the wire signal is only given by secondary emission. The signal is positive, with absolute value 6 times smaller than the signal generated by an H^- (the charge is +0.29 per proton instead of -1.80 for an H^- ion).

These considerations have been used to give a weight to each particle reaching the profile monitor, in order to properly simulate the expected wire signal that was used to reconstruct the emittance. The weights are:

- 1 for non-scattered particles
- -1 for particles scattered at 3 MeV

- -0.2 for particles scattered at 12 *MeV*

5.5.2 Emittance reconstruction

The emittance reconstruction results, as simulated for the 3 and 12 *MeV* cases, for two slit apertures and for different profile monitor resolutions, are summarized in Table 5.7 and Fig. 5.8. For the emittance reconstruction, the values below 0 have been removed from the calculation.

Slit aperture [μm]	Grid pitch [μm]	MEBT		DTL	
		ε	$\frac{\Delta\varepsilon}{\varepsilon}$ [%]	ε	$\frac{\Delta\varepsilon}{\varepsilon}$ [%]
100	50	0.27	-2.10	0.30	1
100	250	0.27	-2.11	0.30	1.5
100	750	0.27	-2.09	0.30	-0.3
200	50	0.27	-0.60	0.30	0.6
200	250	0.27	-0.60	0.30	1.06
200	750	0.28	-0.60	0.30	0.1

Table 5.7: Simulation of the scattering effect on the emittance measurement for the MEBT and DTL case (with nominal beam parameters).

At 3 MeV, the measured emittance results 2.1 % and 0.6 % smaller than the reference emittance for slit aperture of 100 μm and 200 μm . As shown in Chapter 6, the scattered particles are randomly distributed on the screen. Their effect has more importance on the tail of the distribution, where the number of scattered and non scattered particles is almost the same.

The difference between the two slit apertures can be explained by the different ratio of scattered and non scattered particles in the beamlet. The number of scattered particles is almost independent of the slit aperture, but the number of particles passing through the slit without interaction is proportional to the slit aperture.

The reconstruction of beam emittance at 12 *MeV* shows a large dispersion on the values. In order to avoid statistical effects, from the same FLUKA output files, the emittance has been reconstructed with different weight for scattered particles:

- -0.2, the results has been used for estimation of scattering effect.
- 0, used to calculate a reference emittance.

the errors for the different slit apertures and grid pitch are shown in Table 5.8.

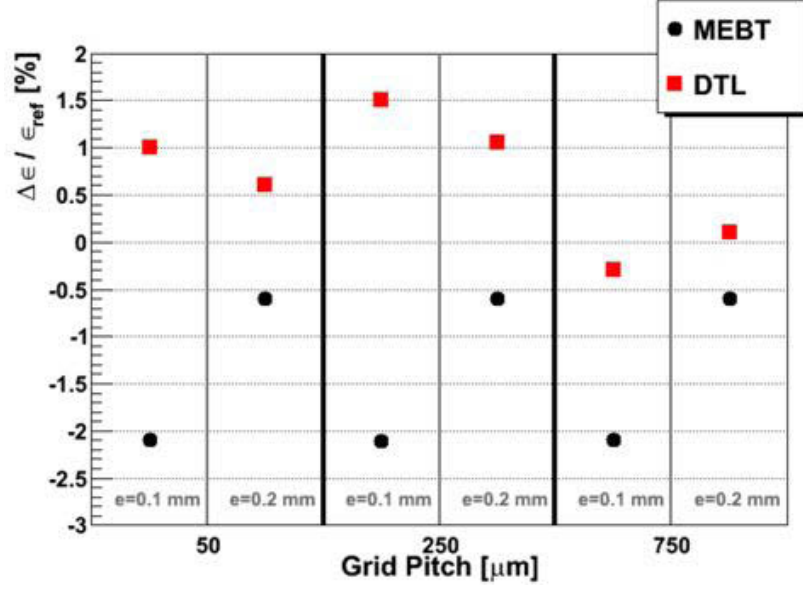


Figure 5.8: Emittance reconstruction error due to scattering at the slit, for two slit apertures, three wire distances and no space charge effects.

Slit aperture [μm]	Grid pitch [μm]	$\frac{\Delta\epsilon}{\epsilon}$ [%]
100	50	-0.20
100	250	-0.16
100	750	-0.20
200	50	-0.10
200	250	-0.10
200	750	-0.10

Table 5.8: Simulation of the scattering effect on the emittance measurement for the DTL case .

From the results of Table 5.8, even though at 12 MeV, the percentage of scattered particles is larger, the influence of scattering is lower. The signal of the scattered particles is 6 times smaller than H^- ions and most of the scattered particles are lost in the vacuum chamber before reaching the profile monitor. The proportion of scattered particles reaching the grid is almost the same for 3 and 12 MeV (see Chapter 6). After scoring the scattered particles with weight equal to -1, the error on the reconstructed emittance is similar to the 3 MeV case. For both the 3 and 12 MeV cases, since the scattered particles are uniformly distributed on the monitor, a simple background subtraction could be used to reduce the measurement error below 1 %.

5.5.3 Comparison proton/ H^-

Since FLUKA is not able to track H^- ions and all the simulations above have been done with protons. The same simulations outputs can be used for the reconstruction of a proton beam by using the same weight for scattered and non scattered particles. For this study, the resolution of the monitor has been considered as perfect (no sampling of the particles distribution on the screen).

Location	MEBT		DTL	
Slit aperture [μm]	100	200	100	200
Norm. ε [$\pi\cdot\text{mm}\cdot\text{rad}$]	0.32	0.31	0.32	0.32
$\frac{\Delta\varepsilon}{\varepsilon}$ [%]	13.46	10.57	7.63	7.30

Table 5.9: Emittance reconstruction assuming a proton beam instead of H^- beam.

As shown in Table 5.9, the scattering of particles on the slit edges induces an increase of the reconstructed emittance. In this case the tails of the particles distribution on the profile monitor are larger than a purely Gaussian distribution. Compare to the previous study, the reconstructed emittance is slightly bigger in all the case, the same effect of the slit aperture can be observed but with a smaller effect.

5.5.4 Geometry aspect

The simulations above have been done with a slit thickness of 3 mm. Another simulation has been performed in the DTL case with a slit thickness of 1 cm. In order to estimate the pure geometrical effect, the weight of the scattered particles has been set to 0. The comparison between the two slit thickness cases for the two slit apertures is shown in Table 5.10.

With a thickness of 3 mm, the slit aperture effect is below 3 % on the reconstructed emittance. If the thickness is increased to 1 cm, an aperture of 0.1 mm is too small to preserve the angular distribution of the particles. The reconstructed emittance is smaller, and the error is around 5 %. By increasing the aperture the angular cut disappears and the emittance is well reconstructed.

5.6 Conclusions

The error due to scattering is small for slit aperture equal or greater than 200 μm , for smaller apertures the error is larger, but a rather simple background subtraction can correct the error. The emittance increase due to space charge

3 mm Slit thickness				
	100 μm Slit aperture		200 μm Slit aperture	
Grid pitch [μm]	ε	$\frac{\Delta\varepsilon}{\varepsilon}$ [%]	ε	$\frac{\Delta\varepsilon}{\varepsilon}$ [%]
50	0.31	2.73	0.30	0.6
250	0.31	3.2	0.30	0.4
750	0.30	1.2	0.30	0.13
1 cm Slit thickness				
	100 μm Slit aperture		200 μm Slit aperture	
Grid pitch [μm]	ε	$\frac{\Delta\varepsilon}{\varepsilon}$ [%]	ε	$\frac{\Delta\varepsilon}{\varepsilon}$ [%]
50	0.28	-5.2	0.30	0.6
250	0.28	-5.3	0.30	0.5
750	0.28	-6.6	0.29	-1.9

Table 5.10: Reconstructed emittance for different slit thickness at the DTL position.

forces cannot be corrected by using the same background subtraction. The only way to reduce the error is to reduce the slit aperture to 100 μm . Assuming the fact that the data analysis can keep the error due to scattering around 1 %, the systematic error on the measurement is expected to be :

- ≈ 3 % for the 3 MeV cases.
- ≈ 2 % for the 12 MeV case.

These values are all within the emittance meter specification.

The smaller aperture value reduces the error and should be used for the measurement. Nevertheless, the possibility of changing the slit aperture is interesting for the early phase of the commissioning in order to increase the transmission of the beam through the slit and give a larger signal.

Chapter 6

SLIT design for the 3 and 12 MeV Test stand

As discussed in Chapter 1 and Chapter 5, a Slit and Grid system will be used to measure beam transverse emittance at 3 and 12 MeV in the diagnostic test bench. An emittance meter, equipped with a stainless steel slit, is already used for the emittance measurement in the LEBT and after the source at 45 keV beam energy. However this slit is not suitable for the LINAC4 commissioning at 3 and 12 MeV, because the slit thickness is shorter than the range of 12 MeV protons in Steel and, as it will be demonstrated in the next section the slit would not stand the thermal load induced by the beam. For these reasons, it was necessary to design a new slit.

The parameters relevant for the slit design are shown in Table 6.1 [31].

	Commissioning scenario	Nominal beam parameter		
Pulse length [μs]	50-100	400		
Rep Rate [Hz]	1	1		
I_{max} [mA]	65	65		
I (after chopping) [mA]	40	40		
Commissioning stage	RFQ	MEBT	DTL	
σ_x at the slit location [mm]	9.13	3.6	1.21	
σ_y at the slit location [mm]	3.46	3.1	1.8	
Energy [MeV]	3	3	12	

Table 6.1: Beam parameters relevant for the slit design.

During the commissioning phase, the beam power is reduced by at least a factor 8 with respect to the normal conditions. Even in this case, due to the low energy

of the beam, the thermal load could be an issue for the intercepting devices. As shown in Table 6.1, the slit should intercept slightly different beams. The ratio between the largest and the smallest beam sizes is almost 8 and there is a factor 4 difference in the energies.

6.1 Thermal effect on the 45 keV slit

The design of the emittance meter used for emittance measurement in the LEBT is shown on the Fig. 6.1.

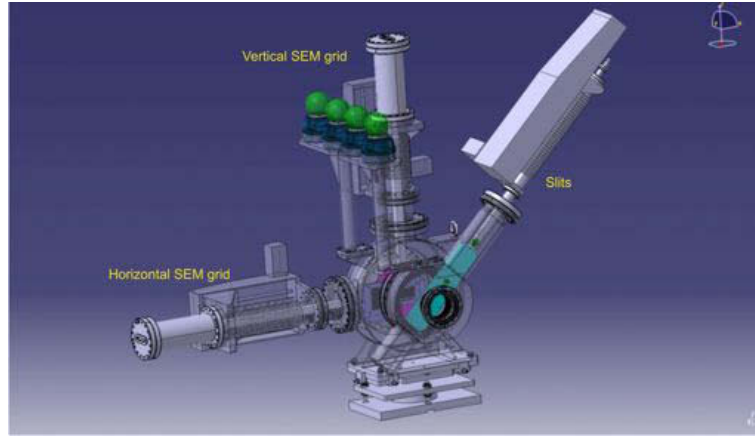


Figure 6.1: Drawing of the emittance meter positioned after the LINAC4 source.

Two slits (for horizontal and vertical scans) are in the same stainless steel blade. Each slit has an aperture of $100 \mu\text{m}$ and a thickness of $200 \mu\text{m}$. Three stepping motors drive the blade and the two SEM grids independently, this slit and the SEM grids are mounted in 2 separate vacuum chamber. More details about this emittance meter can be found in Chapter 7.

It is foreseen to use the same SEM grids for emittance measurement on the 3-12 MeV test bench. The slit could be also used at 3 MeV if the thermal loads are below the limits of stainless steel, but a new slit is needed for the 12 MeV case since the range of protons at this energy in stainless steel is larger than the slit depth.

In order to estimate the thermal stresses on the slit, the temperature increase for one beam pulse induced by a beam on a stainless steel blade is calculated with Eq. 4.6. The hypotheses used for the calculation are:

- Constant specific heat capacity ($C_p = 0.46 \text{ J.g}^{-1}.\text{K}^{-1}$).
- Maximum particles density at $(x, y) = (0, 0)$.

- Maximum of the energy deposition (value of the Bragg peak) calculated with SRIM [34]:
 - 240 MeV.cm².g⁻¹ at 3 MeV.
 - 125 MeV.cm².g⁻¹ at 12 MeV.
- Electron energy deposition neglected.

The result of the calculation for the different commissioning scenarios is shown on the Table 6.2.

Beam energy	3 MeV (RFQ)		3 MeV (MEBT)		12 MeV (DTL)	
I [mA]	40		40		40	
<i>tps</i> [μ s]	50	100	50	100	50	100
Δ T [K]	615	1229	1472	2944	4455	8910
I [mA]	65		65		65	
<i>tps</i> [μ s]	50	100	50	100	50	100
Δ T [K]	820	1639	1963	3925	5940	11880

Table 6.2: Analytical calculation of the temperature increase in case of a stainless steel blade, *tps* is defined as the beam pulse length.

The same calculation has been done for Graphite with a realistic C_p (see equation in section 6.2.1). The result for the maximum beam intensity (100 μ s and 65 mA) during the commissioning phase is shown in Table 6.3.

Material	RFQ	MEBT	DTL	$T_{melt. \text{ or } T_{subl.}}$
Graphite	1359 K	2673 K	4669 K	3773 K
stainless steel	1639 K	3925 K	11880 K	1640 K

Table 6.3: Maximum temperature in the case of a graphite and stainless steel blade for a beam with maximum power during the commissioning phase.

Table 6.2 and Table 6.3 show that, even though carbon behaves better than steel, due to its lower density and higher C_p , the maximum temperature can exceed the sublimation point of the material. Even when the maximum temperature is below such a limit, thermo-mechanical simulations not discussed here indicate that the mechanical stresses reach values that are not acceptable.

The energy deposition density can be reduced by designing the slit with an angle with respect to the beam direction. Fig. 6.2 shows the effect of the slit angle on the maximum temperature.

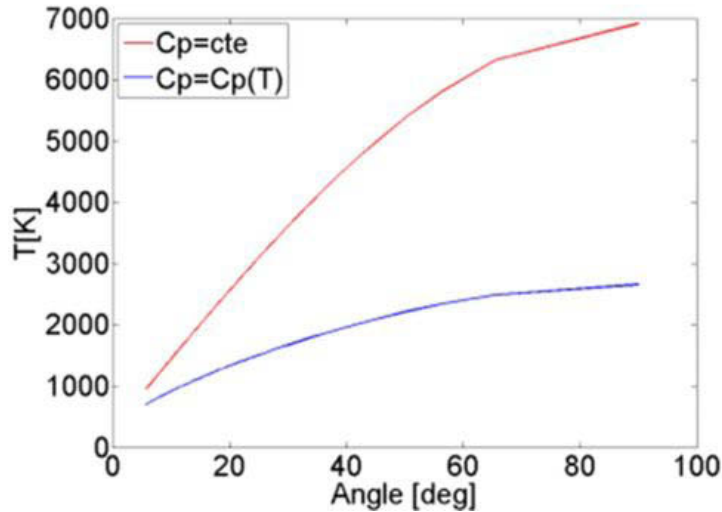


Figure 6.2: Maximum temperature on a graphite slit as function of the angle for the MEBT case, when using a constant $C_p = 0.7 J/(g.K)$ (red) and a variable $C_p(T)$ (blue).

For the MEBT case with a 15 degree slit angle the maximum temperature drops to about 1200 K. The figure also shows the difference in the maximum temperature when approximating the C_p with a constant value, with respect to a more accurate and realistic $C_p(T)$ model.

6.2 FLUKA simulations

The increase in temperature has been also calculated using energy deposition maps given by the FLUKA Monte Carlo code, starting from the expected particles distributions at the slit. The FLUKA output has been used as input for thermo-mechanical calculations with the ANSYS code that yield to the final slit design. The model consisted of a single blade considering different materials and different blade angles with respect to the beam axis.

In the Cartesian mesh, the bin size in x and y have been chosen in order to reduce the statistical error and to keep the particle density almost constant in the bin. Along the z -axis, the bin size must be shorter than the width of the Bragg peak. This resulted in $dx = dy = 200 \mu m$, $dz = 1 \mu m$ for the 3 MeV case and $dx = dy = 100 \mu m$, $dz = 2.5 \mu m$ for the 12 MeV case.

Analytical results show that the worst case is at the DTL position, because the beam at this location is very small and the energy of the beam is deposited in a very small volume. In order to obtain enough statistics the simulation has been

performed using 10^8 particles distributed according to the beam transverse sizes of Table 6.1. No initial divergence and energy spread have been considered.

Fig. 6.3 shows an example of the maximum energy deposition for a beam energy of 3 MeV along the longitudinal of graphite slit with three different angles with respect to the beam axis.

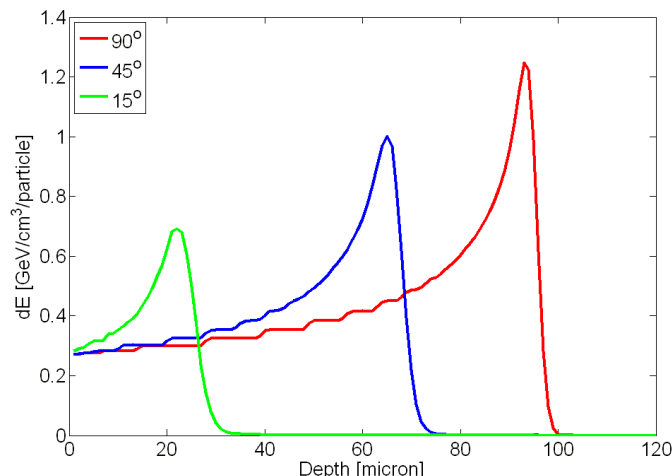


Figure 6.3: Energy deposition along the z axis for three slit angles at 3 MeV (MEBT), in case of a graphite slit.

For a slit with a 15° angle, the energy deposition peak is half the one for a 90° slit. Comparing the two cases, the peak width (in the z direction) is also reduced and the energy deposition is diluted over $100 \mu\text{m}$ instead of $30 \mu\text{m}$.

6.2.1 Material choice

The figures of merit for determining the best slit material are melting (or sublimation) temperature, heat capacity and thermal conductivity. graphite, tungsten and tantalum can be considered for their high melting point (above 3000 K), while beryllium and again graphite for high specific heat capacity. Copper has low melting point and C_p , but the thermal conductivity of this element is the highest among the transition metals, and can be beneficial for cooling. Given these general remarks, the slit material choice was based mainly by analytical estimations of the temperature increase. For the different considered materials, the following $C_p(T)$ models have been considered:

$$\begin{aligned}
C_{p_{\text{tantalum}}}(T) &= 134.64 + 2.88 \times 10^{-2}T - 1.6 \times 10^{-5}T^2 + 5.8 \times 10^{-9}T^3 \\
C_{p_{\text{graphite}}}(T) &= 12.7 + 2.9T - 1.4 \times 10^{-3}T^2 + 3.1 \times 10^{-7}T^3 - 2.4 \times 10^{-11}T^4 \\
C_{p_{\text{copper}}}(T) &= 381.12 + 0.61T - 1.09 \times 10^{-4}T^2 \\
C_{p_{\text{tungsten}}}(T) &= 116.37 + 7.119 \times 10^{-2}T - 6.5828 \times 10^{-5}T^2 \\
&\quad + 3.2396 \times 10^{-8}T^3 - 5.45 \times 10^{-12}T^4 \\
C_{p_{\text{beryllium}}}(T) &= 606.91 + 5.3382T - 4.172 \times 10^{-3}T^2 + 1.27 \times 10^{-6}T^3
\end{aligned} \tag{6.1}$$

The model are represented in Fig. 6.4.

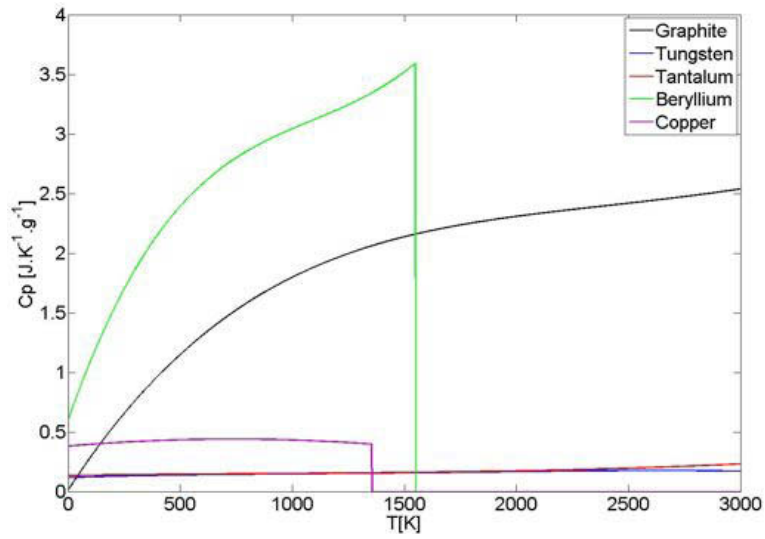


Figure 6.4: Specific heat capacities as function of the temperature, for the different materials used in the FLUKA simulations.

Neglecting, thermal conductivity and other cooling processes. Table 6.4 shows the result for a slit geometry with an angle of 30° and different beam intensities. The other beam parameters stay constant for the calculation. Since the DTL position seems to be the worst case in terms of thermal load, only this case has been simulated for the 5 materials.

The results show that materials with higher density are not well suited for the slit, the melting point is reached in 3 scenarios for tungsten and tantalum, and in all cases for copper. For these materials the energy of the beam is deposited in the first few hundred micrometers. Moreover, these materials have a low Cp . Even if the cooling by thermal diffusivity could be important for copper, it is expected that a copper slit would be damaged. On the other hand, graphite and beryllium have a higher Cp , and the energy deposition per unit of volume is smaller. For

I=65 mA, pulse length=50 μs				
Material	T_{surf} [K]	T_{max} [K]	Bragg peak depth [μm]	density [$g.cm^{-3}$]
beryllium	631	1398	537	1.85
graphite	908	1939	513	1.90
copper	1690	3659	147	8.96
tantalum	2661	3941	103	16.65
tungsten	2979	3659	92	19.35
I=65 mA, pulse length=100 μs				
Material	T_{surf} [K]	T_{max} [K]	Bragg peak depth [μm]	density [$g.cm^{-3}$]
beryllium	907	2148	537	1.85
graphite	1327	3143	513	1.90
copper	3091	7028	147	8.96
tantalum	4076	5368	103	16.65
tungsten	5660	7028	92	19.35
I=40 mA, pulse length=50 μs				
Material	T_{surf} [K]	T_{max} [K]	Bragg peak depth [μm]	density [$g.cm^{-3}$]
beryllium	513	1026	537	1.85
graphite	717	1430	513	1.90
copper	1152	2364	147	8.96
tantalum	1848	2940	103	16.65
tungsten	1945	3384	92	19.35
I=40 mA, pulse length=100 μs				
Material	T_{surf} [K]	T_{max} [K]	Bragg peak depth [μm]	density [$g.cm^{-3}$]
beryllium	697	1601	537	1.85
graphite	1012	2290	513	1.90
copper	2014	4437	147	8.96
tantalum	3070	4372	103	16.65
tungsten	3560	6477	92	19.35

Table 6.4: Maximum temperature increase for the DTL case for several material blade and different commissioning scenario. The angle of the w.r.t. the beam axis is 30 °.

graphite, the sublimation point is never reached, but the maximum temperature for the worst scenario case is closed to this point. The melting point of beryllium is reached in two scenarios and the temperature is close to this point for the two other cases, causing large mechanical stresses. Moreover, beryllium presents some safety problems due to its high toxicity and needs special machining and dedicated operations to prevent any beryllium dust production. Due to these

Angle [deg]	SRIM	FLUKA		
	90	90	45	15
RFQ	1359	1342	1216	937
MEBT	2673	2613	2065	1696
DTL	4669	4594	3931	2790

Table 6.5: Maximum in temperature for the three commissioning stages, as estimated by analytical model (SRIM) and numerical simulations (FLUKA) when considering a 65 mA, 100 μs pulse.

different problems, this material was not considered for the slit and graphite was chosen for the slit material.

6.2.2 Slit geometry

The maximum slit temperature in the case of 100 μs 65 mA pulse calculated from the energy deposition maps is shown in Table 6.5.

Despite having a higher value for the Bragg peak (900 $MeV.cm^{-1}$ at 3 MeV , 400 $MeV.cm^{-1}$ at 12 MeV), the maximum temperature is smaller at 3 MeV , due to the lower transverse particle density at the RFQ and the MEBT position. For the 90° case, the table shows both the results from the full analytical method based on Eq. 1 and SRIM and the ones arising from FLUKA energy deposition. The agreement is rather good and both methods confirm that a slit perpendicular to the beam direction would not survive a single beam pulse.

Also in the case of a slit with an angle of 45°, the temperature increase is above the sublimation point of graphite for the 12 MeV case and this configuration can thus not be used either. In the case of 15°, the temperature increase is below the sublimation point of graphite, thermo-mechanical calculations (see next sections) indicate that at 12 MeV , the thermal load would induce unacceptable mechanical stresses. Since a slit with angles less than 15° would not fit in the available space on the diagnostic test bench, it was decided to move the whole bench by 1 meter downstream of the original position at the DTL exit. In this case both σ_x and σ_y increase by a factor 1.5. With this difference in the particle density, the FLUKA simulations show a maximum temperature of about 1530 K , which is acceptable.

6.3 Finite Element Analysis

The studies presented so far considered a single beam pulse on the slit and neglected any internal or external cooling process. The energy map deposition for the

two worst cases (MEBT and DTL) have been used as input for thermo-mechanical analysis based on the Finite Element Method (FEM); numerical simulations have been performed using commercial code ANSYS [38]. the aim of the FEM studies is to assess thermo-structural behavior of the SLIT; the transient thermal analysis provides detailed results about temperature profiles of graphite blades submitted to several beam pulses. Each beam pulse gives origin to an intense thermal shock, then a dynamic structural analysis is necessary to evaluate dynamic thermal stresses. Finally an analytical study of the thermal fatigue has been performed to verify the lifetime of the graphite blades [39]. In particular ANSYS can simulate the effect of conductive cooling and of the repetition rate, the radiation cooling has been neglected, this is a conservative assumption.

Fig. 6.5 shows the model used for the DTL case with the beam sizes increase by a factor 1.5 with respect to the beam sizes in Table 5.1 and for the full beam power (65 mA and $100\ \mu\text{s}$).

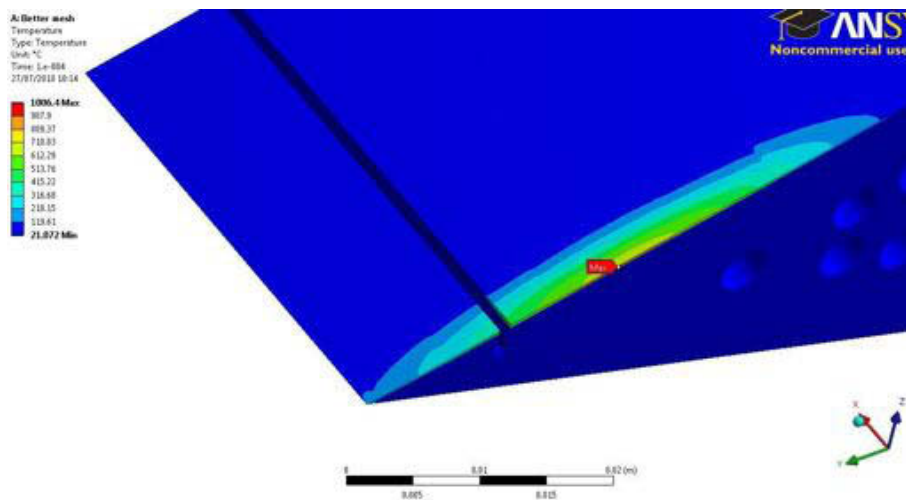


Figure 6.5: Temperature profile on graphite plate with a cooling circuit in copper for DTL case for one beam pulse with conductive cooling activated. (Courtesy of A. Dalocchio and F. Carra).

The color code indicates the temperature increase and shows that at the end of a single pulse, the temperature is about 1270 K . Without cooling effect during the pulse, the temperature is close to the temperature calculated with the analytical model (see Table 6.5). The effect of conductivity reduces the temperature by 250 K , even in $100\ \mu\text{s}$. The same simulations have been done for several pulses without additional cooling, the evolution of the maximum temperature is represented in Fig. 6.6.

After 10 s , the lower temperature on the slit is about 700°C and the maximum

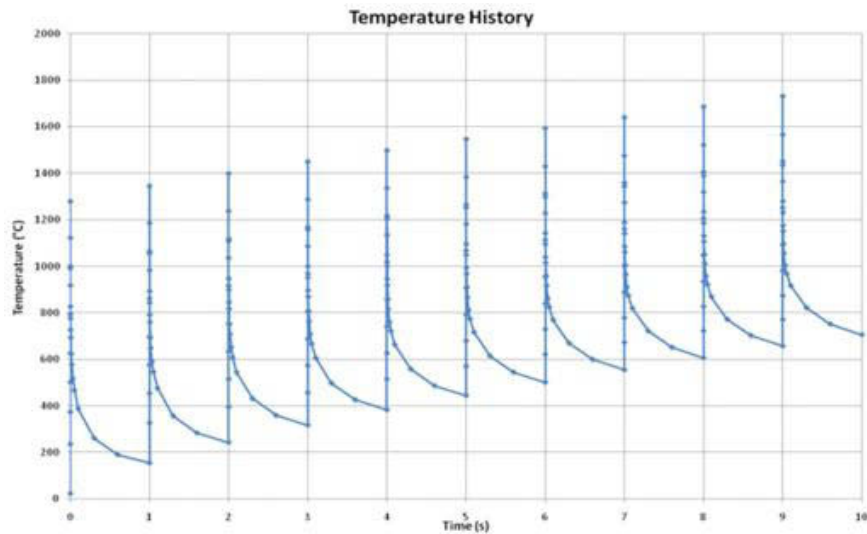


Figure 6.6: Evolution of the temperature with internal cooling by conductivity only, on a graphite plate at 12 MeV . (Courtesy of A. Dalocchio and F. Carra).

reaches $1700^{\circ}C$, above the mechanical limits of graphite.

The same simulation has been done with cooling system consisting of a copper blade with water cooling clamped behind the graphite plate. In order to have more realistic simulation, a thermal resistance has been used between the copper and the graphite. Fig. 6.6 shows the evolution of temperature for 30 s. The equilibrium is reached after only few pulses and the temperature is about 1320 K. This means remaining below the thermo-mechanical limits. More details can be found in [39].

6.4 Final Slit Design

As a component of a slit-grid system, the slits must be designed to sample the beam transverse distributions for each beam position within the beam pipe acceptance. When the slit samples the tail of a beam in vicinity of the beam pipe wall, the slit must absorb all other particles. As a consequence the minimum width of a single slit blade is equal to the beam pipe diameter and the full slit movement stroke must cover at least 2 times the pipe diameter. This is shown in Fig. 6.8 that displays the three slit positions relevant for defining the minimum slit blade and tank dimensions.

The width of the gap between the two slit blades is determined by the accuracy and resolution. For instance, the smaller the gap the lower the space charge effects on the beamlet traveling to the profile monitor. The larger the gap, the better the signal-to-noise ratio at the profile monitor. In order to cover all commissioning

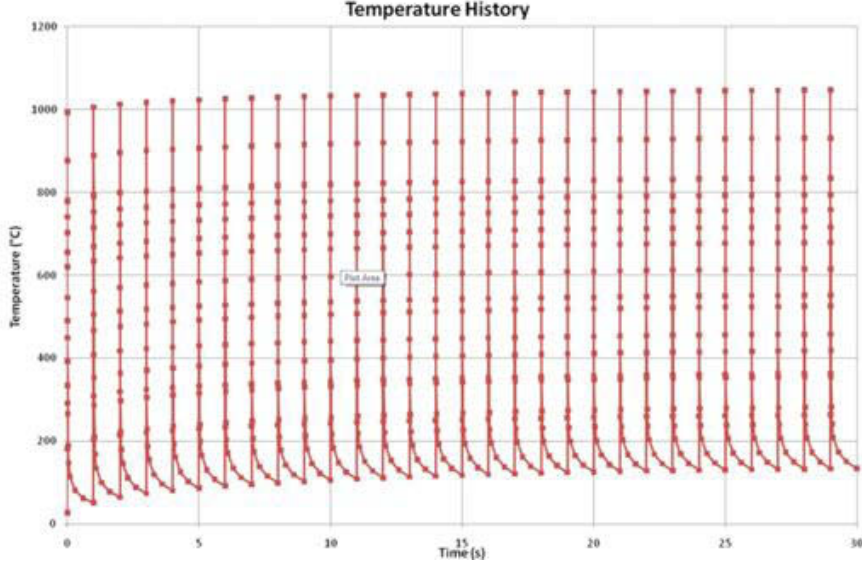


Figure 6.7: Evolution of the temperature with internal and external cooling on graphite plate at 12 MeV . (Courtesy of A. Dallocchio and F. Carra).

scenarios, it is required to have a gap width of 100 μm , adjustable to 200 μm during assembly. Tolerances on the gap width are discussed in the next section. The slit blade thickness (along the beam direction) has to be large enough to stop all H^- particles hitting the blade blocks, and small enough to minimize scattering (and stripping) of H^- particles passing through the gap and traveling to the profile monitor.

	3MeV	12 MeV
H^- range in graphite [mm]	0.1	1
Min/Maximum Slit thickness [mm]	2	5
Min single blade width [mm]		67
Min single blade height [mm]		67
Min slit full stroke		134
Blades distance all along the slit thickness [μm]	100	adjustable to 200

Table 6.6: Parameters relevant for the geometrical and mechanical slit design.

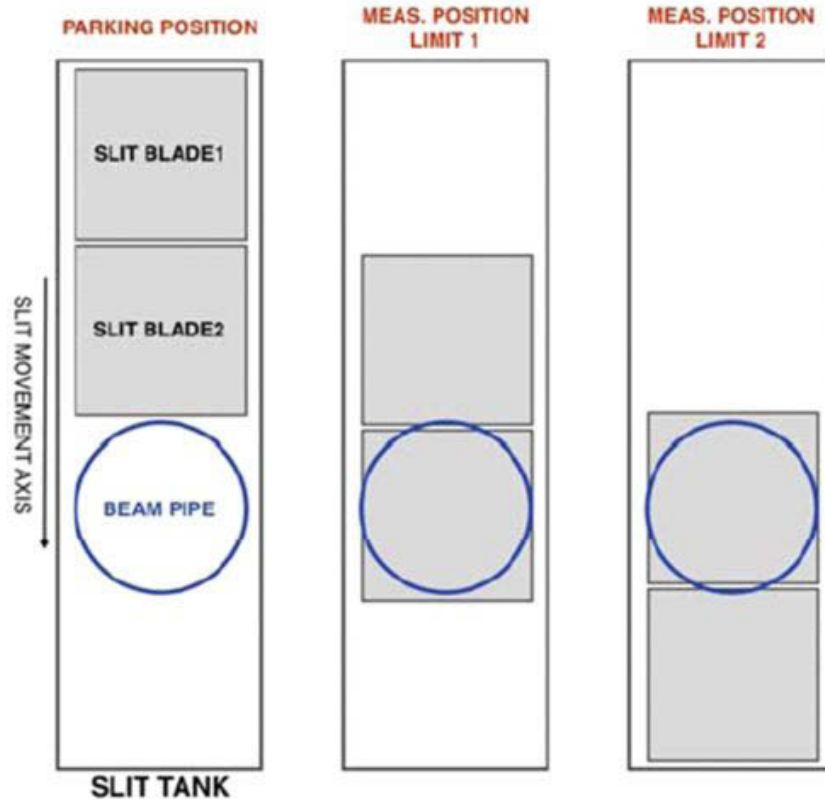


Figure 6.8: Slit geometric constraints.

6.4.1 Slit geometry

All relevant parameters concerning the slit geometry and movement range are shown in Table 6.6. Concerning the slit height, it must be noted that it refers to the blades projection on the transverse plane, considering that a design with inclined blades for diluting the energy deposition is foreseen. In the previous section, the distance between the slit blades (slit gap) has been determined to be $100 \mu m$, adjustable to $200 \mu m$. When considering a surface defined by:

- the full blade thickness along the beam direction.
- four times the maximum expected transverse beam size at the slit, all along the transverse dimension of the blades.

A tolerance of 10 % is required on the slit gap. Such a tight tolerance is necessary to avoid that an excessive portion of the beamlet particles passing through the gap is absorbed or scattered by the blade surfaces. This tolerance must be

respected considering:

- the blade surfaces flatness
- the blades parallelism at the stage of assembly into a slit block
- the slit block assembly on the movement mechanics into the slit tank
- the slit tank external alignment w.r.t. the reference beam transverse and longitudinal coordinates.

For the gap equal to $200\ \mu m$, the tolerance on the parallelism is required to be $\pm 20\ \mu m$. For the assembly with a gap of $100\ \mu m$ the required tolerance is $0 \pm 20\ \mu m$, to avoid a gap smaller than $100\ \mu m$ that could reduce too much the number of particles passing through the gap and therefore an unacceptable small SEM grid signal. Such tolerances, together with the possibility of adjusting the tilt as described below, are intended to guarantee a good enough parallelism with respect to the ideal plane defined by the longitudinal and horizontal (vertical) coordinates.

Each slit must be mounted in a way to allow 2 independent rotation movements by means of dedicated screws outside the vacuum. One rotation axis will be parallel to the beam axis and the other perpendicular (by projection). By means of such rotational alignment after installation and given the flatness and parallelism tolerances specified above, it will be possible to align the horizontal and vertical slit gaps with enough accuracy with respect to the beam coordinates. If necessary, one can also envisage beam based alignments by optimizing the SEM grid signals while tuning with the external screws the slit tilt with respect to the beam longitudinal and transverse axes.

The tolerances of all the assembly parts (tank, bellows, etc...) and of the assembly procedure itself must be such that the maximum misalignments with respect to the transverse and longitudinal beam axes can be corrected by means of the external screws. To allow the coarse slit alignment when the slit is installed on the diagnostics bench, the slit tank must be equipped with 2 survey targets and tilt reference surfaces.

6.4.2 Motorization and actuation system

The overall accuracy on the emittance reconstruction depends on the knowledge of the absolute longitudinal and transverse distances between the slits and the grids. After the system installation, once the survey has guaranteed the required alignment tolerances, it is not necessary that the slit (and grid) movement system provides a step-by-step high precision positioning of the device, as soon as the slit and grid position are accurately measured. Consequently, the slit positions must be monitored by a potentiometer .

Electrical end switches are necessary to set the slit travel limits and to reset the slit zero position. Mechanical stops must avoid the slit movement outside the travel limits, in case of any switch failure. The slit position measurement must be part of an interlock system that forbids the removal of the horizontal (vertical) slit from the parking position when the vertical (horizontal) slit is not in its parking position.

It is highly recommended to have bellows with a compensation for vacuum pressure. In addition, the slit tank design must include a viewport that allows the passage of laser beam when both slits are in the parking position. This detail is related to R&D work for a laser stripping device (see Chapter 8).

6.4.3 Mechanical design.

Assuming slit blades inclined with respect to the beam axis and given the limited longitudinal space, it was decided to segment the slit in several blades, as shown in Fig. 6.9.

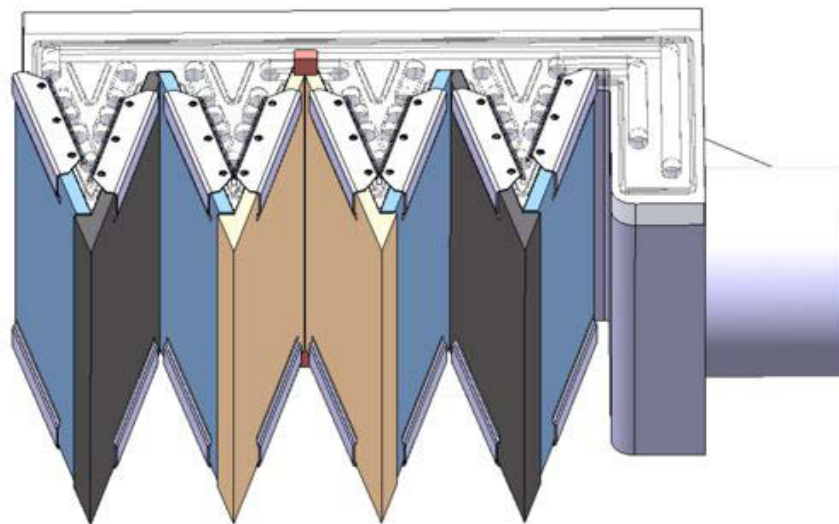


Figure 6.9: Drawing of one slit arm after assembly (courtesy of D. Steyaert and E. Berthome).

The external cooling will consist in a copper block placed behind the graphite. A metal spacer allows choosing the slit aperture during the assembly. More details can be found in [40].

Fig. 6.10 shows the slit assembly with the actuator and the compensation systems.

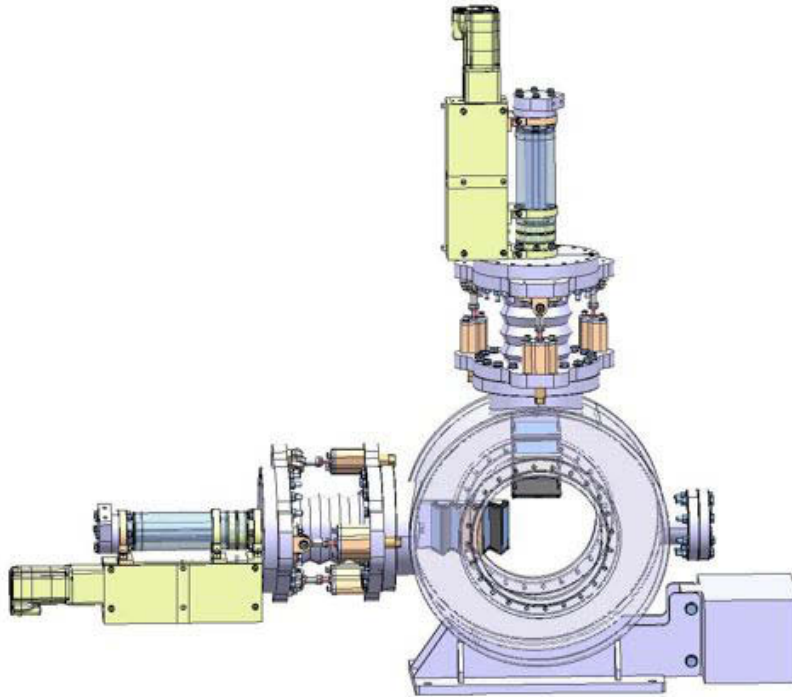


Figure 6.10: Diagram of the slit tank for the emittance meter (courtesy of D. Steyaert and E. Berthome).

6.5 Multiple scattering effects

6.5.1 Simulation model

Particles scattered on the edges of the slit can perturb the sampling of the distributions and lead to errors in the calculation of the emittance. The geometry of the slit and its material must be carefully selected in order to minimize this effect. The effect of multiple scattering has been simulated for different beam energies using the FLUKA Monte Carlo code. This code does not allow to track H^- , all the simulations have been done with protons.

The geometry and the material of the slit have been chosen following the results of by the studies of the thermal effects. The slit model (see Fig. 6.11) consist of two carbon blades, arranged symmetrically to the z axis with an angle of 15° . The aperture of the slit is $100\ \mu\text{m}$ or $200\ \mu\text{m}$ and the slit thickness is $3\ \text{mm}$, as shows in Chapter 5, these values are optimal for measurement resolution. The particle distributions used as input for FLUKA have been generated using the Twiss parameter of Table 6.7.

Due to the large beam size at the RFQ position, the number of particles passing

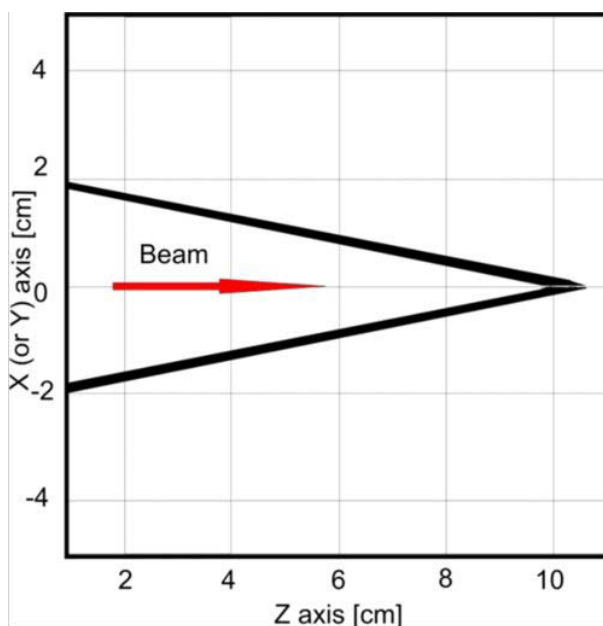


Figure 6.11: Diagram of the slit.

through the slit is low and large statistical errors appear, this case is not presented in this thesis.

6.5.2 Amount of scattered particles

Table 6.8 and Table 6.9 show the percentage of scattered particles reaching the detector (an area of $7.2 \times 7.2 \text{ cm}^2$ positioned 3.5 m downstream the slit) for several position of the slit in the horizontal transverse plane at 3 MeV (MEBT) and 12 MeV for a slit aperture of 100 μm .

The proportion of scattered particles after the slit is larger than 7 % for the

Location Plane	MEBT		DTL	
	H	V	H	VE
α	1.35	-0.13	-0.39	-0.26
β [m/rad]	3	2.2	0.63	1.23
Norm. ϵ_{rms} [$\pi \cdot \text{mm} \cdot \text{mrad}$]	0.3	0.31	0.3	0.31
ϵ_{rms} [$\pi \cdot \text{mm} \cdot \text{mrad}$]	3.5	3.875	1.875	1.93
Beam width [mm]	7.3	6.5	2.5	3.5

Table 6.7: Beam parameter at the three locations of emittance measurement.

Slit Position [mm]	Particles after the slit	Scattered particles [%]	Particles reaching the grid and scattered [%]
-3.5	925	99.892	0
-2.8	2316	49.698	3.1588
-2.1	7768	23.893	2.7152
-1.4	19211	17.058	2.5086
-0.7	33024	15.08	2.8645
0	40087	14.424	2.6145
0.7	32971	15.444	2.8302
1.4	19235	16.725	2.638
2.1	7685	23.305	2.8515
2.8	2355	48.493	3.4236
3.5	877	99.886	0

Table 6.8: Results of FLUKA simulations for different slit position at the DTL location. The beam source contains 10^6 particles and the slit aperture is $100 \mu m$.

Slit Position [mm]	Particles after the slit	Scattered particles [%]	Particles reaching the grid and scattered [%]
-10	1667	92.681	3.937
-8	3264	50.521	2.1212
-6	7830	25.032	2.4917
-4	16336	13.522	1.7526
-2	25802	8.3637	1.191
0	30361	7.1012	0.92384
2	26266	8.5814	1.2258
4	16498	12.68	1.5378
6	7915	23.752	2.0133
8	1775	6.7606	2.4175
10	1720	92.791	3.125

Table 6.9: Results of FLUKA simulations for different slit position at the MEBT location. The beam source contains 2.5×10^6 particles and the slit aperture is $100 \mu m$.

MEBT and 14 % for the DTL in the better case, this proportion goes up to 93 % at 3 *MeV* and almost 100 % at 12 *MeV*. At 3 *MeV* the proportion of scattered particles reaching the SEM grid varies from 0.5 % to 4 % depending on the slit aperture and its position. At larger energy, for slits position between -3 and 3 the percentage of scattered particles is almost constant around 1.25 % with a 200 μm slit aperture and twice this value for a 100 μm slit aperture. Most of the scattered particles are lost in the drift space

Fig. 6.12 and Fig. 6.13 shows the percentage of scattered particles reaching the detector for the MEBT and DTL case with 100 μm and 200 μm slit aperture.

As shown in Fig. 6.14 and Fig. 6.15 the scattered particles are randomly distributed at the screen location. Except at the center of the distribution, the effect of the scattered particles on the signal will be almost constant on the detector. The large variation on the distribution is a statistical effect due to the low number of particles in simulation.

The same simulations have done for the vertical plane, with similar results.

6.5.3 Energy distribution of scattered particles

The energy of scattered particles has been also scored, and show that the H^- ions scattered on the slit edges will be stripped. The mean energy of these particles is 1.78 *MeV* at 3 *MeV* and 7.5 *MeV* at 12 *MeV*. If we measure the mean energy of particles reaching the grid, the mean energy is 2.8 *MeV* for the MEBT case and 10.9 *MeV* for the 12 *MeV* case. The energy distributions of the scattered particles are shown in Fig. 6.16 to Fig. 6.19.

The particles with higher energy losses are more deviated and dont reach the SEM grid. Most of the particles reaching the profile detector have an energy close to the initial energy, however, the distributions show a long tail and the minimum energy is around 15 % of the initial energy in the DTL case. In first approximation, the average energy of the particles reaching the SEM grid can be used to calculate the SEY of these particles and determinate the effect on the emittance measurement.

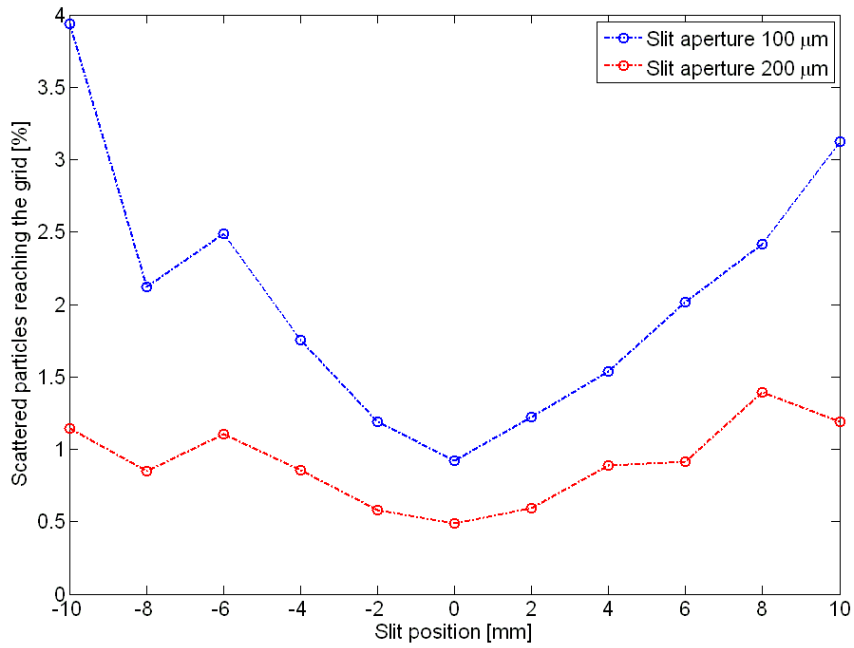


Figure 6.12: Percentage of particles scattered reaching the profile detector ($7.2 \times 7.2 \text{ cm}^2$) in function of the slit position, for the MEBT case.

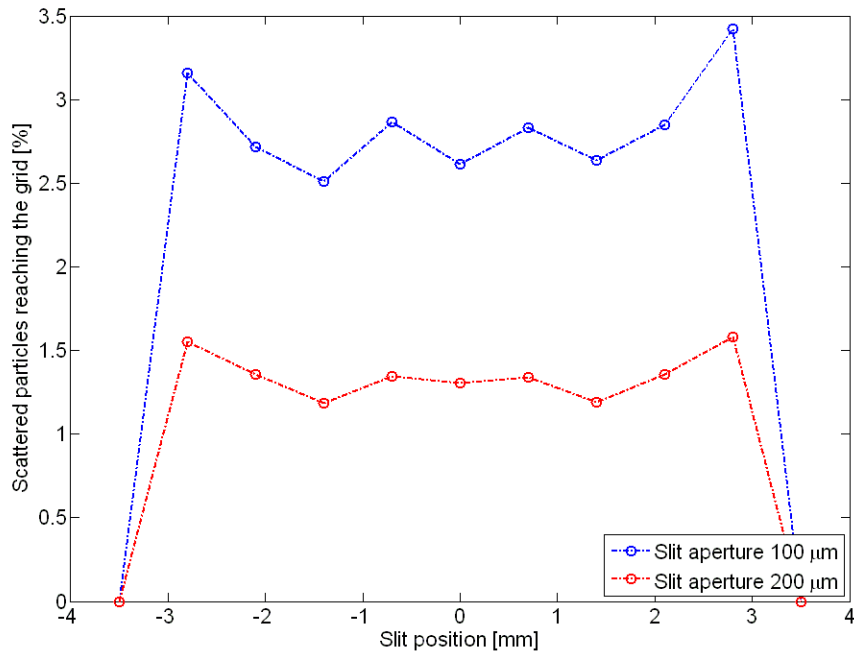


Figure 6.13: Percentage of particles scattered reaching the profile detector ($7.2 \times 7.2 \text{ cm}^2$) in function of the slit position, for the DTL case.

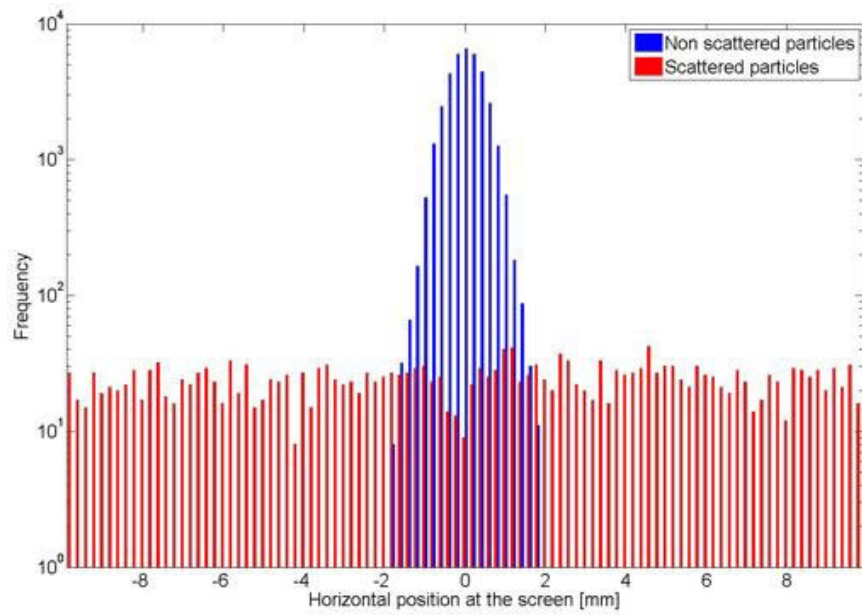


Figure 6.14: Particle distribution on the profile detector for the slit in position $x=0$ (MEBT). In blue, the non scattered particles, in red, the distribution of scattered particles (logarithmic scale).

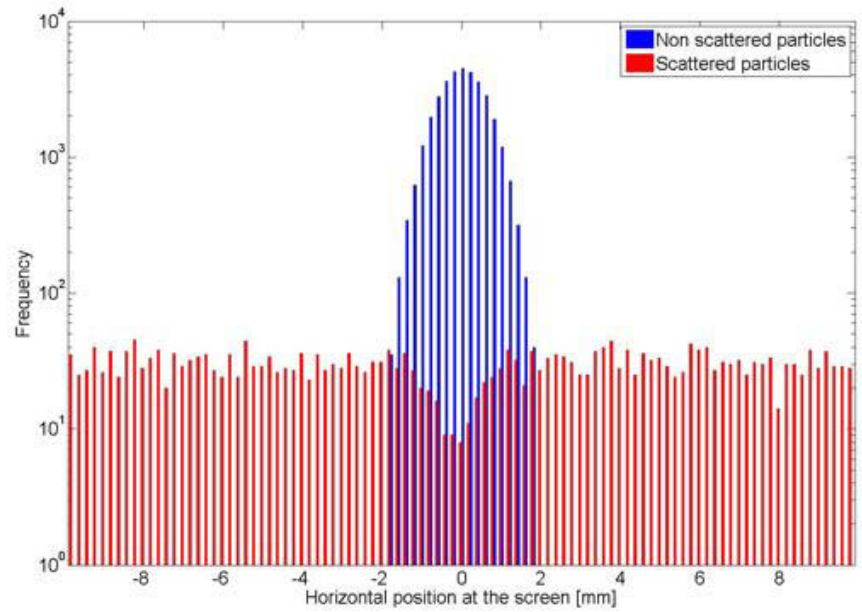


Figure 6.15: Particle distribution on the profile detector for the slit in position $x=0$ (DTL). In blue, the non scattered particles, in red, the distribution of scattered particles (logarithmic scale).

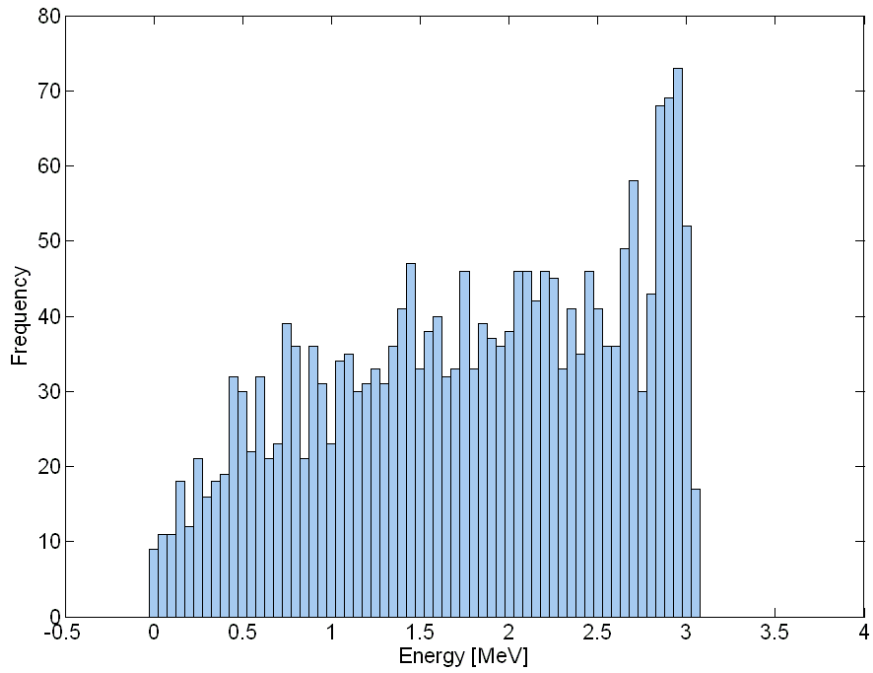


Figure 6.16: Energy spectrum of scattered particles after the slit (for the slit in position $x=0$ (MEBT)).

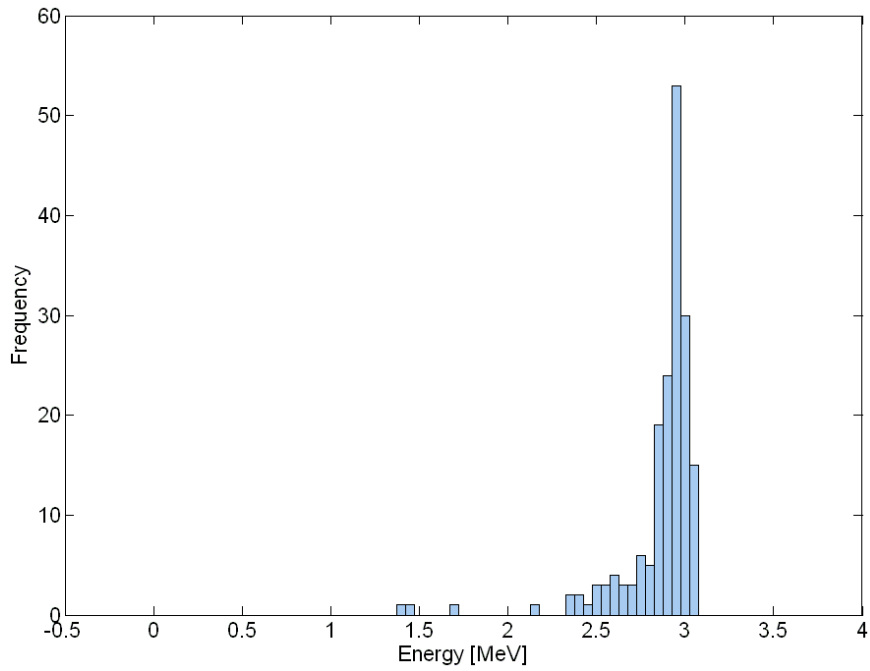


Figure 6.17: Energy spectrum of scattered particles reaching the SEM grid (for the slit in position $x=0$ (MEBT)).

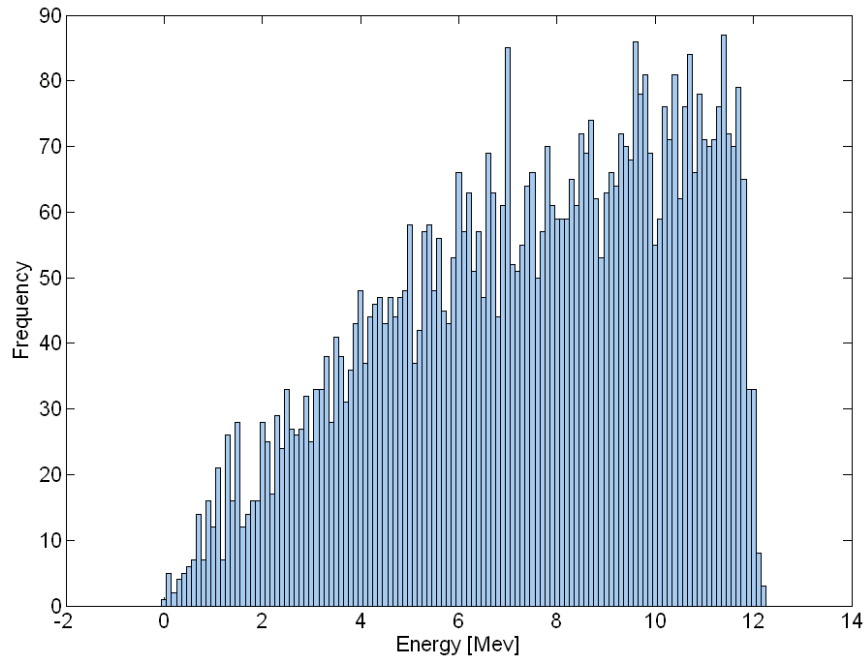


Figure 6.18: Energy spectrum of scattered particles after the slit (for the slit in position $x=0$ (DTL)).

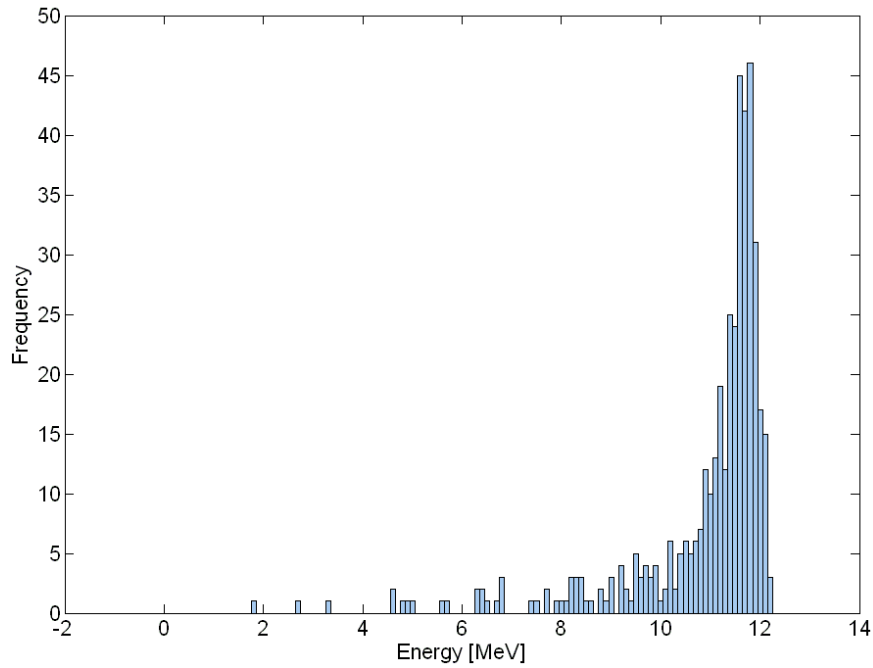


Figure 6.19: Energy spectrum of scattered particles reaching the SEM grid (for the slit in position $x=0$ (DTL)).

6.6 Conclusion

The LINAC4 Test bench slit has to stand the full beam commissioning power without deformation and damages. The slit design was achieved by combining energy deposition and thermo mechanical simulation. The design consists in graphite blades inclined of 15° with respect to the beam trajectory clamped to copper block hosting the external cooling.

Despite the design optimization, the commissioning of the Chopper line and the DTL tank 1 should start with reduced power in order to avoid any problem due to quadrupole fault and small beam sizes at the slit.

Chapter 7

LINAC4 and SNS transverse emittance measurements

7.1 Beam emittance and beam profile measurement at the LINAC4 source front end

The H^- source and the low energy beam transport (LEBT) line will determine to a large extent the performance of LINAC4. Up to now only the source and LEBT are installed. First measurements have been performed using a Faraday Cup to measure the total source intensity, a slit and grid emittance meter for transverse emittance measurements and a spectrometer for energy spread measurements.

7.1.1 Commissioning of the LINAC4 LEBT

As shown in Fig. 7.1, the LINAC4 LEBT consists of two solenoids, a diagnostic box and two steerers. The aim of the LEBT is to provide the beam matching from the source to the RFQ and to monitor the source performance. Due to the small RFQ acceptance, the commissioning of the LEBT is crucial to ensure good beam transmission.

Emittance measurements have been done at three different stages:

- after the source
- after the first solenoid
- after the second solenoid, i.e at the RFQ input.

In addition, profile measurements at the RFQ input have been done using the emittance meter slit and a Faraday cup. Energy spread measurements have been performed after the first solenoid. A systematic comparison between measurements

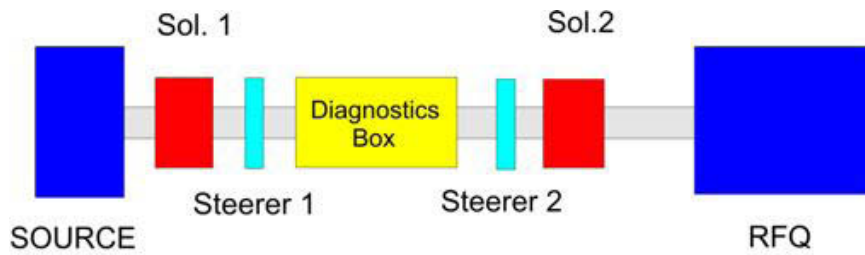


Figure 7.1: Diagram of the LINAC4 LEBT.

and beam dynamics simulations has been done for the two last stages.

7.1.2 LINAC4 low energy emittance meter

A picture of the emittance meter developed for the source front-end and the LEBT is shown in Fig 7.2.

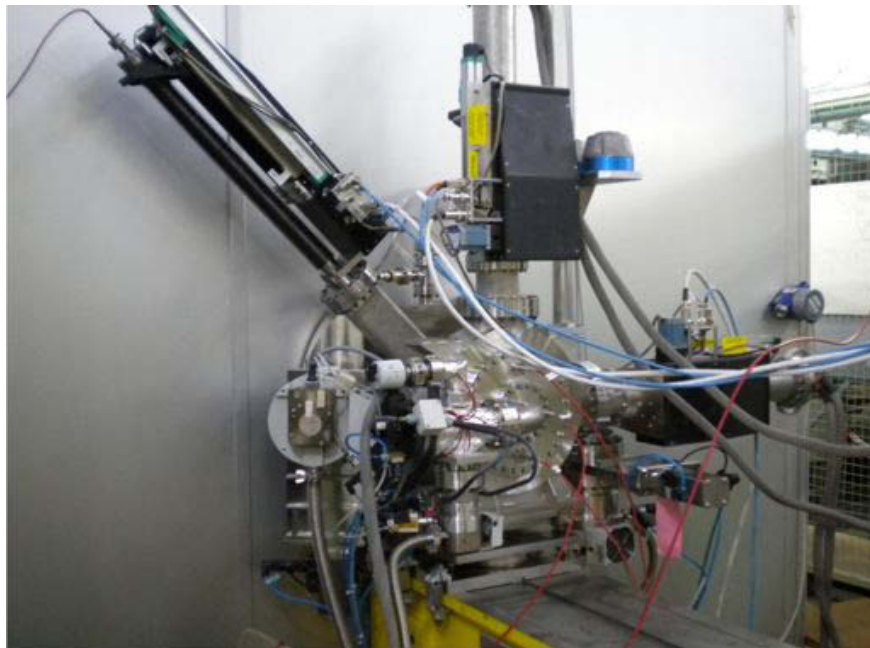


Figure 7.2: LINAC4 source emittance meter.

The system consists of two SEM-grids and one stainless steel blade inclined at 45 degrees relative to the vertical axis. The blade is 1 *mm* thick and two 100 μm gaps have been machined, one parallel to the horizontal axis, the other parallel to the vertical axis. The thickness of the blade is reduced to 200 μm around the

gaps. The two SEM grids are positioned 20 *cm* downstream the slit, each monitor can be moved separately. The grids consist of 40 tungsten wires separated by 750 μm . The diameter of the wires is 40 μm . Each wire is connected to a separate acquisition channel and sampled at 160 *kHz*. Both the blade and the SEM grids are moved using stepping motors. For each slit position, the corresponding grid can be moved with steps of 50 μm in order to improve the overall resolution. A schematic diagram of the system for one transverse plane is presented in Fig. 7.3.

A Faraday cup is positioned 8 *cm* downstream the SEM grid in order to monitor the current of the beamlet during the emittance measurement and to measure the full beam current when the slit is out to perform beam profile measurements by scanning the beam with the slit and measuring the beamlet current.

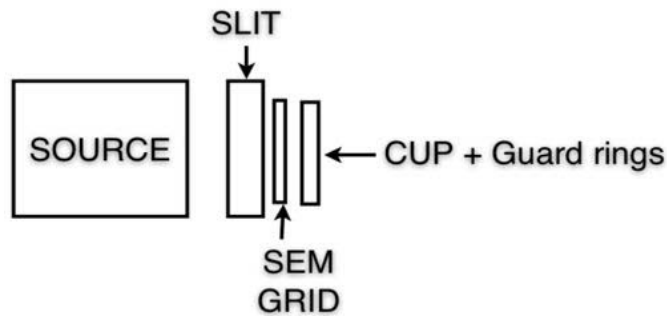


Figure 7.3: Diagram of the emittance meter.

In between the SEM grids and the cup, two polarization guard rings have been installed to minimize the recoil of secondary electrons from the cup to the wires, as avoid electrons to escape the cup and falsify the measurement result in the cup.

7.1.3 Determination of emittance meter polarization setting

Effect of the guard rings polarization on the current measurement

According to the Sternglass theory (see Chapter 3) describing secondary emission (SE), about 3 electrons are produced for each 35-45 *keV* H^- ion impinging on a tungsten or stainless steel surface. Secondary emission of electrons is expected from the slit, from the Faraday cup and in general from any location where H^- are lost (beam pipe, guard rings, etc). The energy range of the electrons is about $10\text{eV} \pm 5\text{eV}$. As shown in Fig. 7.4 the Faraday cup consists of a measurement plate and two guard rings (P1 and P2). These three parts are all made of stainless steel and can be polarized independently.

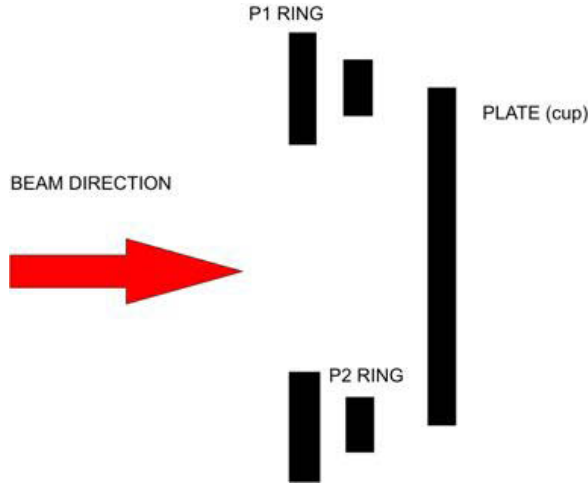


Figure 7.4: Diagram of the Faraday cup.

The effect of the guard rings polarization has been studied with the CST Microwave Studio suite [41] by simulating the tracks of the secondary electrons in the polarization electrical field. The secondary emission has been simulated by two electron sources, one located at the surface of the plate, the other at the surface of the P1 ring. The source consists of electrons with $E_k = 10 eV \pm 10eV$ and isotropic angular distribution. For the measurement of the full beam current, when the slit is out, a negative voltage on the P2 ring repels secondary electrons back to the cup, thus minimizing the measurement errors. One simulation example is shown in Fig. 7.5.

Effect of the guard rings polarization on the emittance measurement

During emittance measurements, it is necessary to minimize the recoil of electrons from both P1 and the cup. A configuration allowing the measurement of both the beam current and the emittance was initially considered, with $V_{P1} > 0$ and $V_{P2} < 0$. In this configuration a large number of electrons from the cup can reach the wire grid, as shown in Fig. 7.6a. Indeed, $V_{P1} > 0$ minimizes the emission of electron from P1, but also modifies the field generated by P2 alone and vanishes the effect on the electrons generated at the cup.

The only solution found so far for an unperturbed wire signal consists in polarizing P1, P2 and the cup with a positive voltage (Fig. 7.6b). This has the inconvenience of not allowing the simultaneous measurement of the beamlets current.

In addition, two polarization rings are positioned on the SEM grid frame to collect secondary electrons from the wire and minimize cross talk between wire

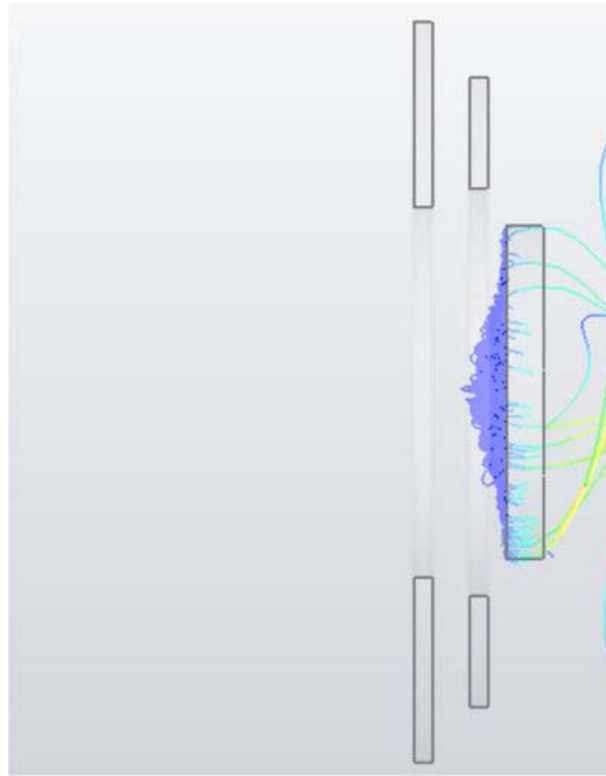


Figure 7.5: Trajectories of the electrons emitted by the cup with $V_{P2} = -500V$ (Microwave Studio simulations).

signals. As for the Faraday cup and the guard rings the influence of the bias voltage has been simulated. The results show a weak field at the center of the SEM grid due to the symmetry. At this location, the field is not sufficient to collect secondary electron and the measurement can be perturbed.

Nevertheless, the SEM grids are close to the guard ring during emittance measurements, and the electrical generated by the Faraday cup and the two guard rings polarization is sufficient to collect the electrons. To avoid perturbations from the electrical field generated by the grid polarization, this one should not be biased.

7.1.4 Emittance meter commissioning

In a first commissioning phase, the LINAC 4 source has been delivering a 35 keV and 20 mA H^- beam. During this phase it was possible to commission and validate the emittance meter. Different measurement sessions were dedicated to:

- benchmark the simulations presented in the previous section and establish

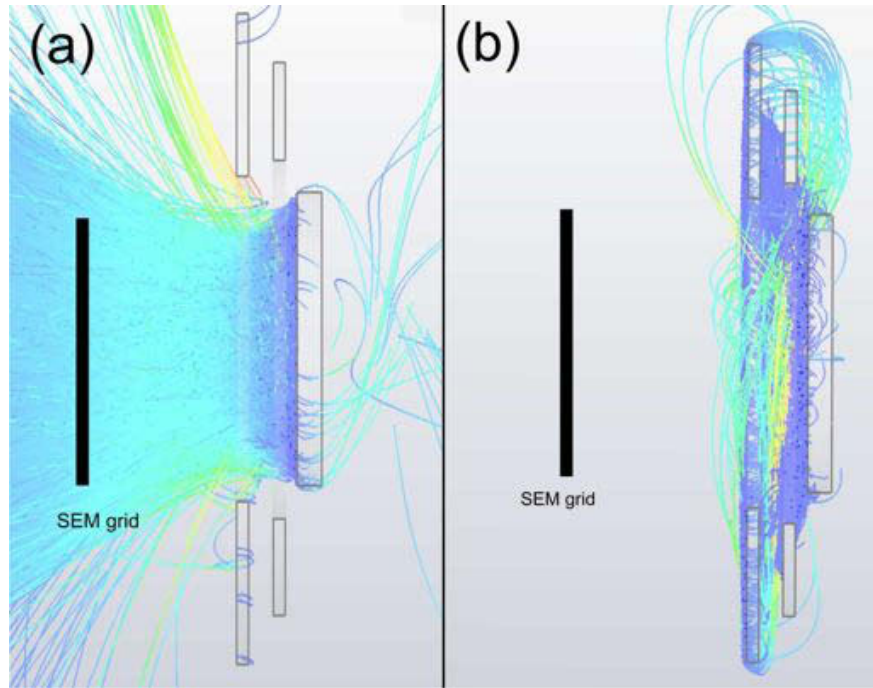


Figure 7.6: Trajectories of the electrons emitted by the cup with $V_{P1} = +500V$ and $V_{P2} = -1200V$ (a) and trajectories of secondary electrons emitted by the cup and the P1 guard ring for $V_{P1} = V_{P2} = V_{CUP} = +500V$ (b).

- the best bias voltages for the beam current and emittance measurement
- characterize the beam emittance, even though the source was delivering a reduced power compared to the design value ($45 keV$ and $80 mA H^-$ beam) (see next section).

Fig. 7.7 shows the result of a beam current measurement (with the slit in the parking position) by monitoring the charge collected at the Faraday cup, with $V_{P1} = V_{P2} = V_{CUP} = 0$ (red line) and with $V_{P1} = V_{CUP} = 0, V_{P2} = -1500$ (blue line). The measurement is in perfect agreement with the simulations presented above: with no bias on P2 a large number of electrons escape from the cup, on which a positive charge is measured. The measurement also shows a typical example of the source beam current evolution during the $400 \mu s$ pulse. This kind of measurement can be used to tune the source parameters in order to optimize the transmission up to the cup.

With the slits scanning the transverse beam distributions, several measurements were performed with different combinations of the three bias voltages, while measuring the beamlet distribution with the wire grid. Fig. 7.8 refers to a scan in

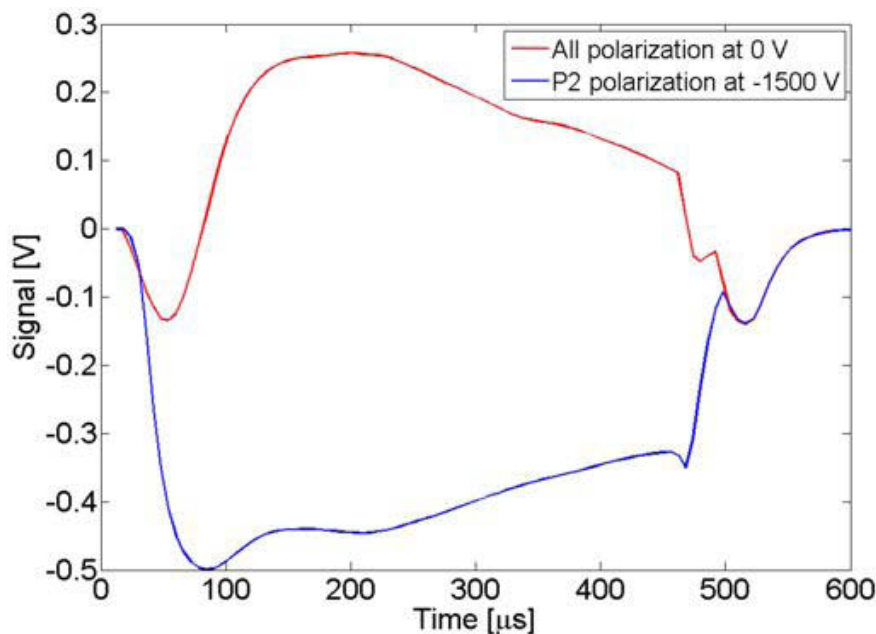


Figure 7.7: Current measurements on the cup for two P2 polarization.

the vertical plane and shows the signals of the wires when the slit is positioned at the center of the beam. For each wire the average between 100 and 300 μs from the beam pulse start is plotted. The negative signals on the wires not directly hit by the beamlet when $V_{P1} = V_{P2} = V_{CUP} = 0$ (blue line) indicate secondary electrons backscattered from the cup.

The same effect is evident when $V_{P1} = 400, V_{P2} = -1300, V_{CUP} = 0$ (red line). This confirms the simulation results, that is: $V_{P1} > 0$ modifies the electric field pattern generated by $V_{P2} < 0$ so that a large fraction of the secondary electrons generated at the cup hit the wires. With all biases at +300 V (black line on the plot), all secondary electrons generated at the cup (and possibly on P1) are kept on the plate, and the signals from the wires are unperturbed as predicted.

7.1.5 Beam emittance and beam profile results

From the measurement, the Twiss parameters and emittance values have been determined with a first approximation algorithm, based on the calculation of the RMS distributions (in position and angle) after eliminating all wire signals below a threshold calculated from the maximum signal value.

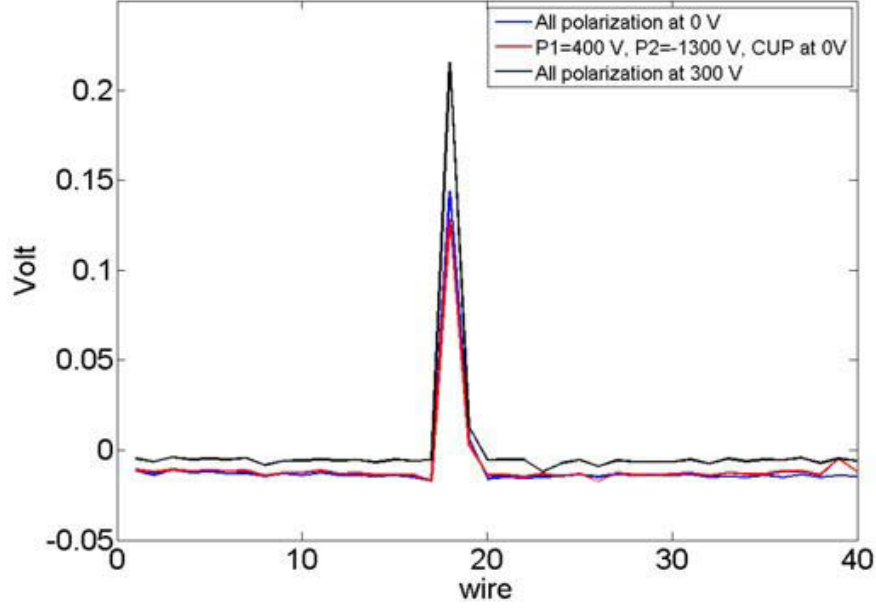


Figure 7.8: Average signals on the SEM grid wires for 3 polarization settings.

Emittance measurement after the source

During a first source commissioning phase an H^- ion beam at an extraction voltage of 35 kV , a pulse length of 400 μs and a RF power of 20 kW has been measured. In this configuration the source provides 20 mA beam current and the emittance meter has been used to characterize its transverse distribution. The first measurements showed that the angular resolution of the SEM grid was not sufficient due to the large distance between two wires (750 μm). In order to increase the angular resolution, 7 steps of 100 μm have been used for the SEM grid, for each slit position. Examples of measurement results are shown in Table 7.1. The agreement with the expected values for the LINAC4 source [42] is remarkable.

	$\varepsilon_{rms}[\pi.mm.mrad]$	α	$\beta[mm/\pi.mrad]$
Measured value	0.26	-35.8	6.24
Nominal value	0.25	-24.4	4.3

Table 7.1: Nominal and measured beam parameters of the source for the vertical plane (with 1 % threshold on the data).

After this phase, the extraction voltage was upgraded to 45 keV . Unfortunately this caused problems with electron currents of too high power destroying the electron dump and it was decided to switch the source to proton mode and continue

the commissioning of the source and the LEBT with proton beam. New emittance measurements have been done after the source with an extraction voltage of 45 kV and different RF power.

Table 7.2 shows the reconstructed Twiss parameters with 3 RF power settings with a threshold set at 10 %.

Horizontal plane			
RF Power (kW)	$\varepsilon_{rms}[\pi.mm.mrad]$	α	$\beta[mm/\pi.mrad]$
20	0.07	-54.97	9.47
40	0.19	-44.77	7.96
60	0.29	-45.73	8.25
Vertical plane			
RF Power (kW)	$\varepsilon_{rms}[\pi.mm.mrad]$	α	$\beta[mm/\pi.mrad]$
20	0.06	-65.09	10.9
40	0.19	-44.77	7.96
60	0.29	-45.73	8.25

Table 7.2: Twiss parameter calculated with a threshold at 10 % and variable RF power.

The emittance increases with RF power. With the largest value, aperture limitation due to the beam pipe appears (see Fig. 7.9).

A comparison between the results on the emittance reconstruction for protons and H^- with the source running at 20 kW are shown in Fig. 7.10.

The emittance is smaller for the proton beam. This can be explained by the lower space charge effects at 45 keV . These results have been used as initial values for beam dynamics simulations of the LEBT.

Emittance and intensity measurement after the first solenoid

Once the measurements on the source were terminated the emittance meter was moved after the first solenoid, which separates different particle types coming from the source. The current in the solenoid was varied from 0 to 1000 A . Fig. 7.11 shows the result of such a measurement which clearly displays 4 different species of ions coming from the source. As expected, the result shows that heavier ions are less focused by the solenoid and are separated in phase space from the protons. Simulations allowed identification of the particle types that are also indicated in Fig. 7.11.

Beam dynamics simulations and measurements show a remarkable agreement As shown in Fig. 7.12.

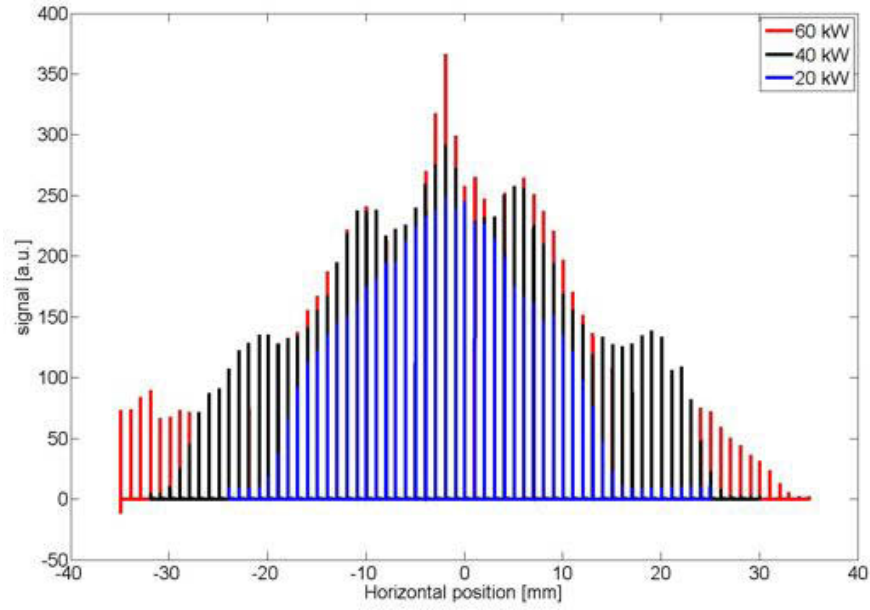


Figure 7.9: Beam profile measured at different RF power, note the aperture limitation for the 60 kW cases.

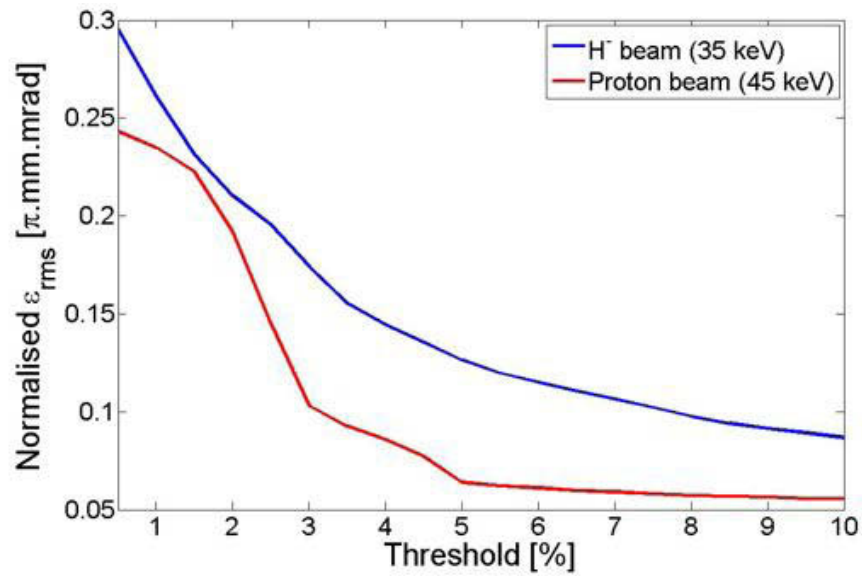


Figure 7.10: Normalized emittance measured for a proton beam at 45 keV and H^- beam at 35 keV as a function of the threshold applied to the data.

Different solenoid currents have been tested and for each setting the emittance has been measured in both planes. The beam current as a function of the solenoid

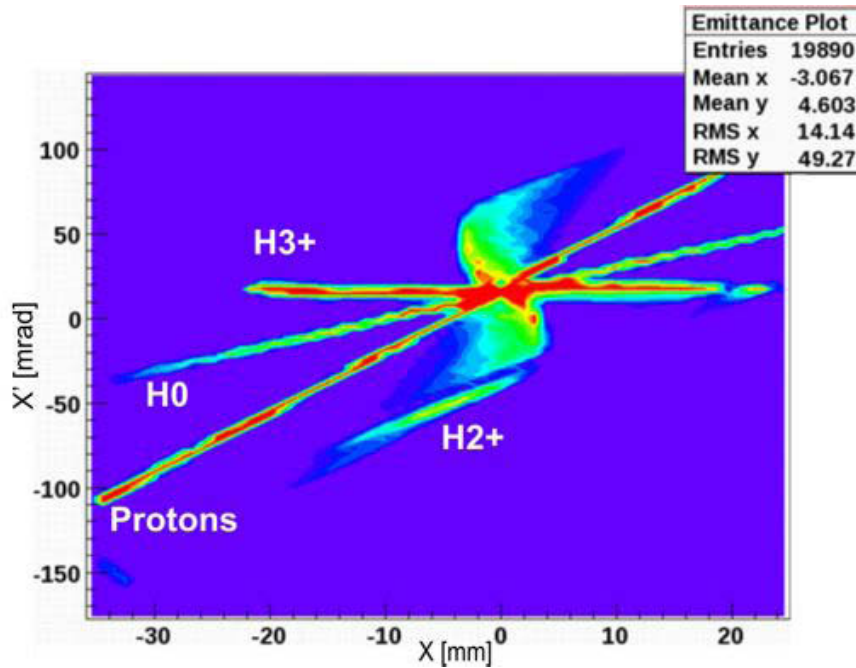


Figure 7.11: Different particle types separated by solenoid.

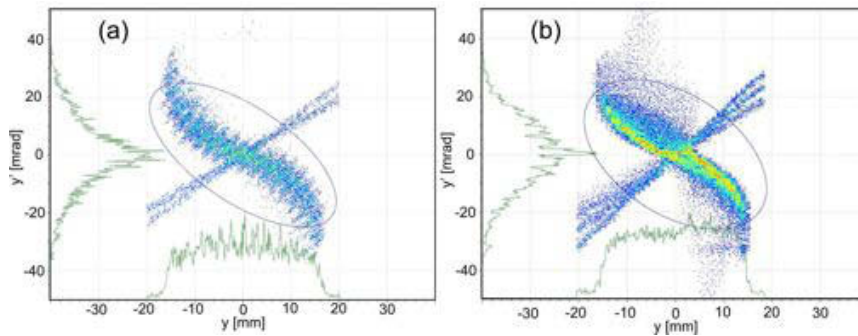


Figure 7.12: Simulated (a) and measured (b) phase space after the first solenoid, for $I_{sol1}=600$ A (Courtesy of J.B. Lallement).

current has also been measured with the Faraday cup positioned at the rear of the emittance meter. The results show that a current of 600-700 A maximizes the transmission of the particles onto the Faraday cup. It also shows that the current increases linearly with the RF power between 20 kW and 40 kW. The current difference between 40 and 60 kW is negligible and is due to beam losses on the solenoid. A solenoid current of 600 A is needed to match the beam parameters to the RFQ acceptance and will be used as reference for the rest of the commissioning phase. Due to the separation of the particles, the emittance analysis is difficult (at

this time, the calculation of the emittances of the different species has not been completed).

Beam profile at the RFQ input

Finally, emittance measurements have been done with the complete LEBT. The current on the second solenoid was varied from 250 A to 400 A. The different scans show that the beam is moving with the second solenoid current. Excursions of 11 mm in the horizontal plane and 4 mm in the vertical plane have been calculated. This showed that the beam was not centered in the second solenoid and had to be steered.

The emittance meter slit and the Faraday cup have been used to make profile measurements with the solenoid off. This has been done in order to calibrate the steerers in the LEBT. The results show that the kick in the horizontal plane given by the steerers is -5.4 mrad/A in both planes. An example of beam profiles obtained with the slit and Faraday cup is shown in Fig. 7.13.

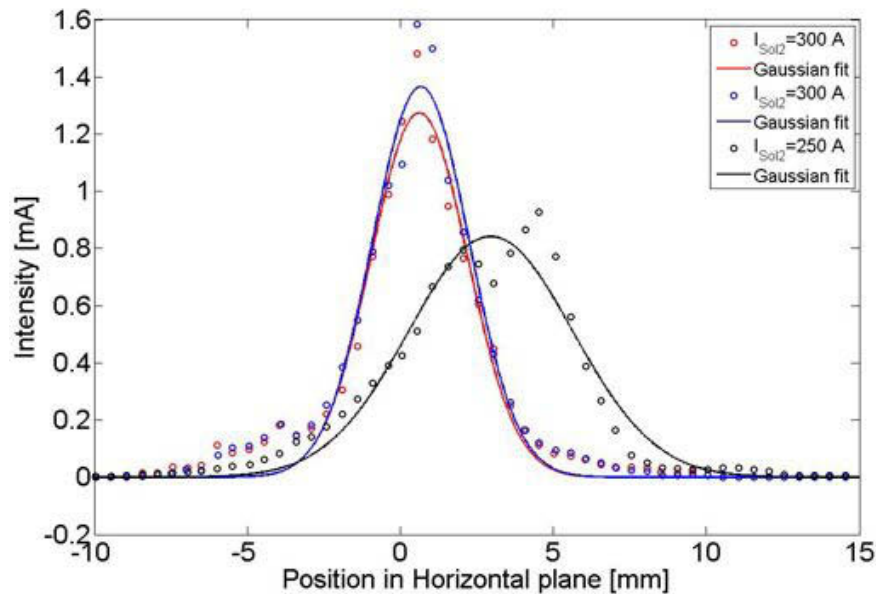


Figure 7.13: Beam profiles 8.3 cm downstream the RFQ input for two solenoid settings. The beam displacement arises from the beam offset with respect to the solenoid center.

Fig. 7.13 also demonstrates the good source stability, the two plots at 300 A solenoid current have been measured few weeks apart.

These values have been used to find the setting of the steerers. .

Emittance measurement at the RFQ input

After centering the beam trajectory through the solenoids, the next step of the commissioning was to determine the matching parameters for the RFQ injection. This phase is still under completion, and Fig. 7.14, shows the results of an emittance scan for a given solenoid setting.

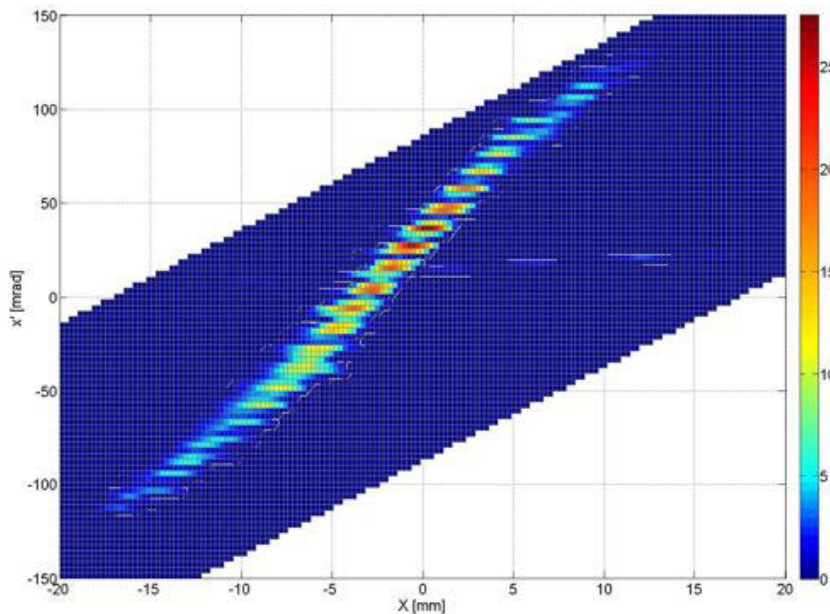


Figure 7.14: Emittance profile 8.3 *cm* downstream the RFQ input when the two solenoid indicated in Fig. 7.1 are 685 A and 375 A respectively.

The heavier species are not focused by the LEBT and, most of them are lost in the vacuum pipe, the signal is low compared to the proton signal.

7.1.6 Energy spread and intensity measurements

Determination of the source energy spread

The energy spread has been measured with a spectrometer and a grid system. A slit is positioned downstream the first solenoid, its aperture can be modified from 1 *mm* up to 5 *mm*. The particles passing through the slit are then bent by a dipole magnet and measured by a SEM grid, installed in the following spectrometer line.

At the grid location the beam size is determined by:

- The energy spread of the beam.
- The space charge effects after the slit.

- The divergence of the beam.

The slit is used to reduce the effect of the space charge and the beam divergence. The slit and the grid are positioned at the focal point of the optic. the slit has no influence on the profile reconstruction.

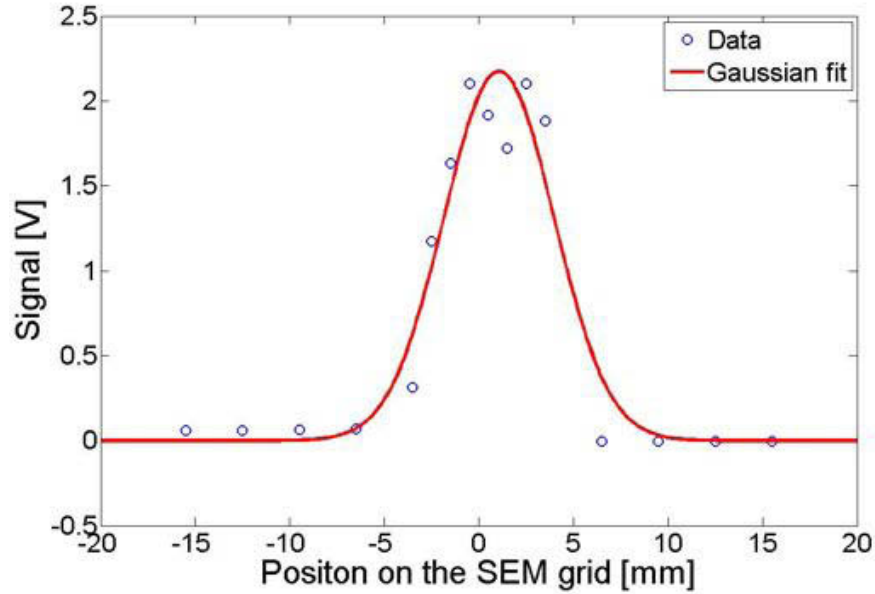


Figure 7.15: Reconstructed profile and Gaussian fit at the end of the spectrometer line.

Fig. 7.15 shows the reconstructed profile with a slit aperture of 4 mm. The calibration factor found by decreasing the extraction voltage by 500 V is $50 \text{ eV} \cdot \text{mm}^{-1}$. With this factor, the energy spread interpolated is $\pm 170 \text{ eV}$.

Beam transmission in the LEBT

The two Faraday cups allow us calculating the beam transmission through the LEBT as function of Solenoid 1 current. At the moment of writing the maximum transmission (90 %, resulting in 27 mA at the RFQ input) has been achieved with 600 A in the first solenoid. Unfortunately the transmission drops by about 50 % when applying the settings for matching the RFQ entry ($I_{sol1} = 680 \text{ A}$).

7.2 Beam emittance measurement at the Spallation Neutron Source (SNS) MEBT

The SNS facility is an accelerator-based neutron source in Oak Ridge (Tennessee, USA). The facility consists of a linear accelerator, a storage ring and a Mercury target. Eighteen neutron beam lines are available for the various users. The linac is divided in two parts:

- A normal conductive structure, which accelerates the beam up to 186 MeV .
- A super conductive structure, which accelerates the beam to the final energy (1 GeV).

The first part is similar to the LINAC4, with an H^- source, a LEPT, a RFQ, a MEPT and a DTL structure. This section describes a set of measurement taken in 2010-2011.

7.2.1 Description of the SNS emittance meter

As it is foreseen in LINAC4 during the commissioning phase, in the SNS MEPT, an emittance measurement is performed with a slit and grid system, a diagram of the device is shown in Fig 7.16 [43], [44].

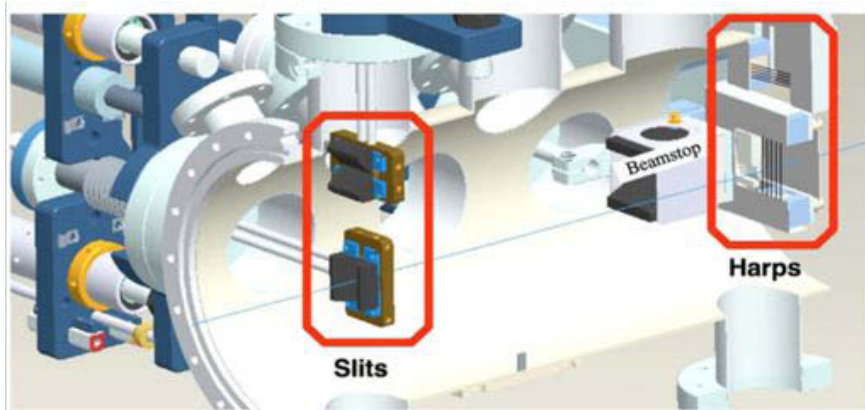


Figure 7.16: CAO drawing of the slit and grid system in the SNS MEPT.

Each slit is made of two Graphite blocks, fixed on a Copper piece, with a gap of $100\ \mu\text{m}$. The Graphite is machined in order to have a slit with an angle of 45° w.r.t to the beam axis. The SEM grids are positioned 352 mm downstream and consist in sixteen $100\ \mu\text{m}$ diameter Tungsten wires separated by 1 mm , that

are used for the profile reconstruction. In addition polarized wires are positioned between each signal wire.

7.2.2 Emittance measurement

During dedicated beam study periods, the beam power of the SNS linac is reduced in order to perform emittance scans in the MEBT . The pulse length is reduced from 1 *ms* to 50 μ s. A measurement example is shown in Table 7.3 with the LEBT chopper off. Similar to the LINAC4 measurements described in Section 7.1.5, the RMS emittance is calculated by thresholding the data.

Threshold [%]	Horizontal plane			Vertical plane		
	ϵ_{norm}	α	$\beta[mm/mrad]$	ϵ_{norm}	α	$\beta[mm/mrad]$
0	0.4967	1.148	0.8811	0.2825	-0.185	0.4922
1	0.2267	2.163	1.595	0.2152	-0.264	0.574

Table 7.3: Twiss parameters calculated for the nominal MEBT optic and bias polarization.

Chopper effect

The LEBT chopper can be switched off for the measurement. As shown in Fig 7.17, the chopper has a strong influence on the wire signal.

The wire signal is constant during the pulse when the chopper is off and a modulation appears when it is on. The modulation frequency is 250 *kHz*, equal to the chopper frequency. If the signal is integrated over a pulse, the emittance is 30 % larger with the chopper on. By reducing the integration window to 0.4 μ s (1/10 of the chopper frequency), the emittance is similar in both cases. With chopper on, the signal from two neighbor wires have a phase shift equal to π , that lead us to conclude that the emittance ellipse rotates as function of the chopper frequency.

Background signal.

As shown in Table 7.3, the threshold has a strong influence for the horizontal plane, because a constant background appears on the wires when the slit is close to the beam center. The effect is also evident in Fig 7.18.

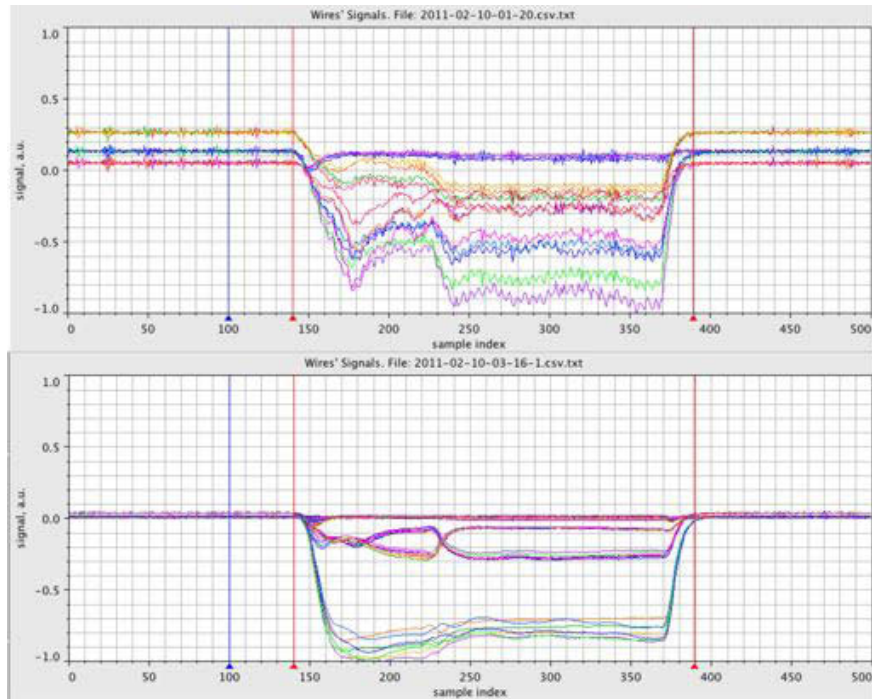


Figure 7.17: Influence of the LEBT chopper on the signal wire shape, on the top with chopper on and on the bottom when the chopper is off. Each sample is separated by $0.4 \mu s$.

Quadrupole scan

The optics of the MEBT line has been modified by changing the strength of a quadrupole. The values of the measured emittance, α and β parameters as function of the quadrupole current are shown in Fig 7.19.

The emittance is almost constant, as it should be, for quadrupole current between 25 and 31 A, and the nominal MEBT optics foresees 28 A. Some second order effect appears when the strength is too low or too high and leads to emittance blow up.

Polarization effect

The nominal bias polarization on every second wire is set at 300 V, and several emittance scan have been done in order to check the effect of such polarization on the measurement:

- A scan with V_{bias} at 300 V as reference.
- A scan with V_{bias} at 0 V.

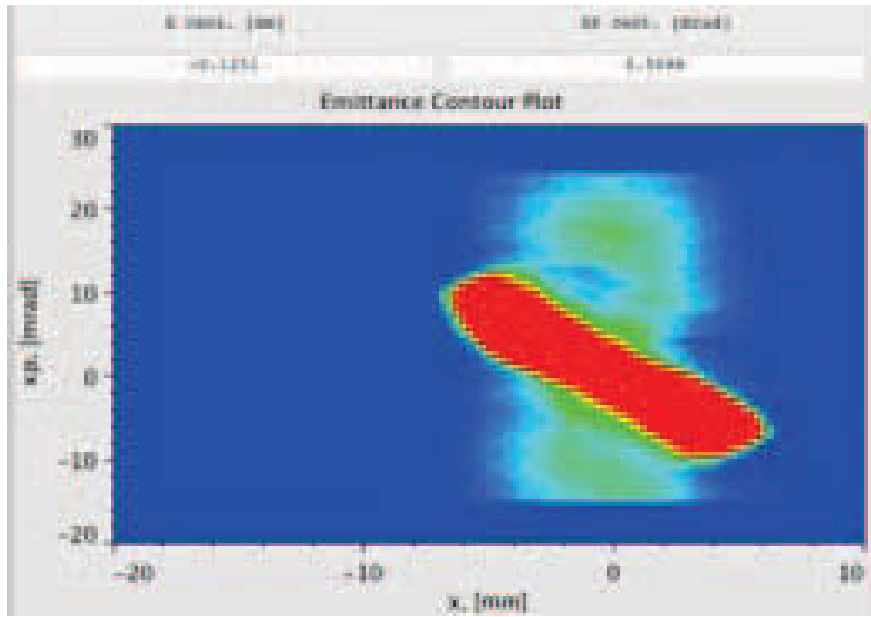


Figure 7.18: Coupling effect on the signal

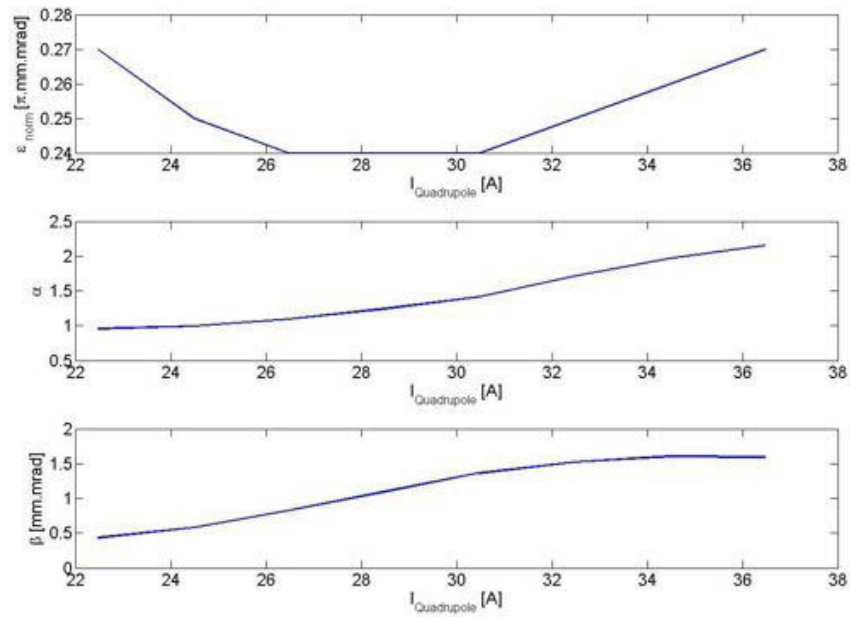


Figure 7.19: Variation of Twiss parameters as function of quadrupole strength (with a threshold on the data at 1 %)

- A scan with V_{bias} at - 300 V.

All the scans have been done in the vertical plane in order to avoid the background signal shown above and with the LEPT chopper off. The negative polarization is intended, to repel secondary electrons on the wire. In this case the dominant process for the signal generation should be the charge deposition (see Chapter 4) and the signal polarity is negative. The shape of the signal on the SEM grid is represented in Fig 7.20.

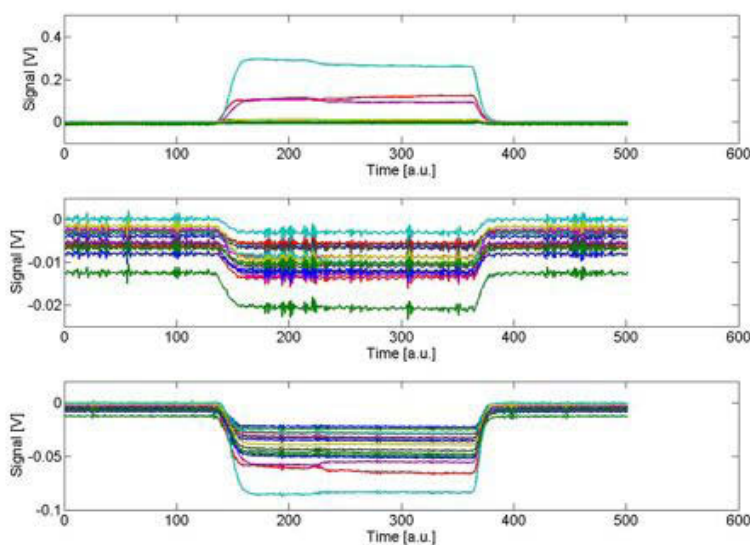


Figure 7.20: Effect of the bias polarization on the wire signals. On the top for $V_{bias} = 300\text{ V}$, on the middle for $V_{bias} = 0\text{ V}$ and on the bottom for $V_{bias} = -300\text{ V}$.

The results are:

- Very low background for a bias of 300 V.
- Signal close to zero when the polarization is switched off.
- Background with the same order of magnitude of the signal when the polarity is negative and for all the wires.
- Beamlet profile sizes comparable for the 300 V and -300 V.

When the polarization is set at 0 Volt, the signal is low compared to the nominal setting, a small signal (close to the noise level) appears on all the wires with opposite polarity with respect to the nominal setting. The SEY is close to the charge deposition in the wire, the net charge is about 0 and the emittance reconstruction is not possible with this data.

When the polarization is switched to -300 V , the net charge creation is negative and the signal polarity is inverted. As for the case without polarization all the wires provide a signal and the emittance reconstruction is difficult.

The beamlet profiles for the bias voltage of 300 , 0 and -300 V are shown in Fig. 7.21. A background subtraction, calculated with the first 100 samples in time domain, has been applied.

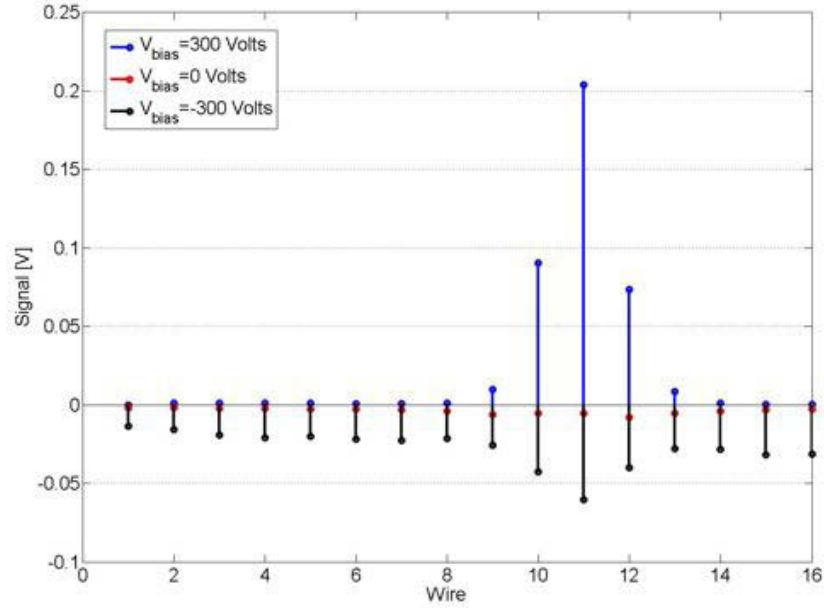


Figure 7.21: Beamlet profile reconstruction as function of the polarization bias.

Cross talk due to secondary emission seems excluded, and the origin of the background is not known at this time.

7.2.3 Multiple scattering effects on the emittance reconstruction

As shown in Table 7.3 and Fig. 7.18, the measurements in horizontal plane show a constant background on the SEM grid. The simulations done for LINAC4 (see Chapter 5 and 6) show similar results due to multiple scattering on the slit edges (see Fig. 6.14). The same simulations have been done with the SNS beam parameters in order to estimate the effect of multiple scattering on the emittance reconstruction. For this, as also described in Chapter 5 and Chapter 6, the FLUKA Monte Carlo simulation code and PATH have been used to simulate the slit geometry and the emittance measurement. The FLUKA simulations have been fed

with a particle source generated by PATH using the Twiss parameters shown in Table 7.3 (with a threshold of 1%).

By design, considering the tolerance of graphite machining, the slit thickness (see Fig. 7.22) is around few microns, below the range of 2.5 MeV protons in graphite. Unfortunately, such thickness is not well known and one of the aims of the simulations was to find the best model for matching the experimental results.

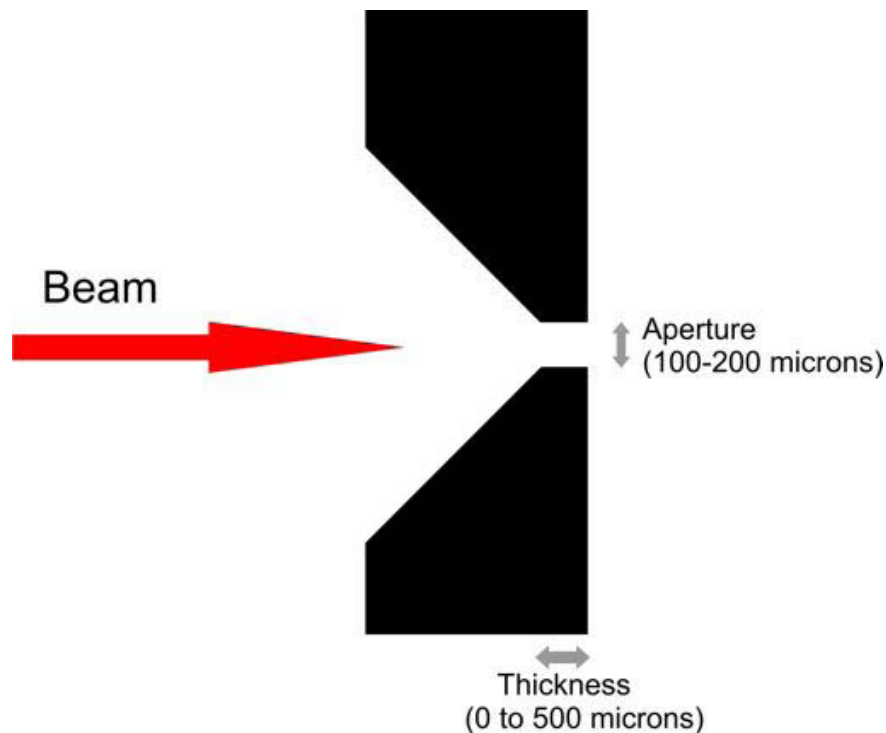


Figure 7.22: Schematic diagram of the slit used in the simulations.

At first, the influence of the slit thickness and the slit aperture on the particle distribution at the SEM grid has been estimated. Then, a full emittance scan for different slit thicknesses has been simulated in FLUKA and in PATH without space charge. The emittance has been reconstructed with different weight for the scattered particles in the FLUKA inputs.

Finally, the two emittance measurement simulations with a larger slit thickness (100 and 500 μm) have been performed and the emittances have been reconstructed with the weight for scattered particles found previously, in order to investigate improved slit geometries.

Effect of the slit thickness

The effect of the slit geometry on the particle distributions at the SEM grid has been studied for a slit in the central position, where the number of scattered and non scattered particles is high in order to reduce the statistical error. All the simulations have been done for a slit aperture of $100 \mu m$.

Fig. 7.23 to Fig. 7.26 and Table 7.4 summarize the distribution of scattered and non scattered particles for different slit thicknesses, starting from an ideal device with no thickness.

For the 3 smallest thicknesses ($0, 10$ and $50 \mu m$), the scattered particle distribution is constant at the grid. For a slit thickness of $100 \mu m$, the small fraction of scattered particles allows only concluding that the distribution is constant, with a large statistical error.

Slit thickness [μm]	Transmission of non scattered particles [%]	Percentage of scattered particles after the slit	Percentage of scattered of scattered particles reaching the grid
0	2.34	55.47	44.28
10	2.34	51.12	37.69
50	2.33	19.98	7.66
100	2.33	1.75	0.43
500	2.32	1.91	0.68

Table 7.4: percentage of non scattered and scattered particles for different slit thickness with a constant aperture of $100 \mu m$.

When the slit thickness is below the range of a $2.5 MeV H^-$ beam in graphite, the percentage of scattered particles after the slit is above 20 %. If the slit thickness is above the range, the number of scattered particles is reduced by a factor 20, the number of particles reaching the grid by a factor 100. This can be explained by the larger scattering angle due to the longer interaction in matter. The transmission of non scattered particles is almost the same for the 5 geometries; the angular aperture is large enough to accept a large amount of the beam divergence.

Effect of the slit aperture

With the same inputs, different slit apertures have been simulated ($40, 100$ and $200 \mu m$) with a constant slit thickness ($0 \mu m$). The results are shown in Table 7.5.

The transmitted particles increase linearly with the slit aperture, and the number of scattered particles after the slit is almost the same for the three apertures.

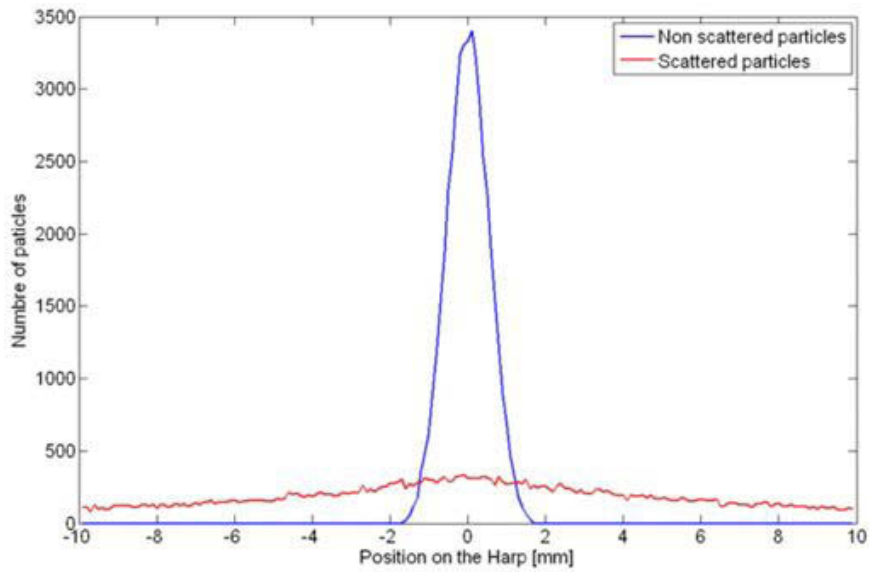


Figure 7.23: Simulated distribution of the particles at the SEM grid for a slit thickness equal to 0 and slit aperture equal to $100 \mu m$.

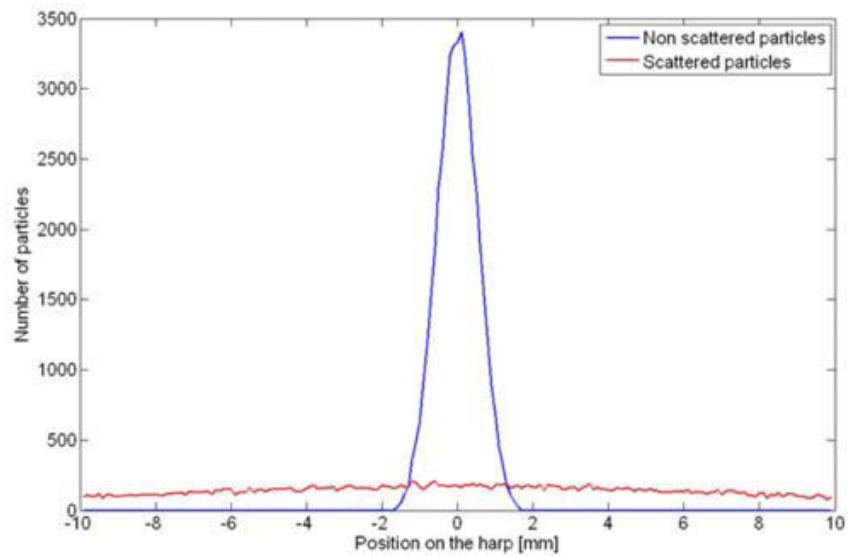


Figure 7.24: Simulated distribution of the particles at the SEM grid for a slit thickness equal to $10 \mu m$ and slit aperture equal to $100 \mu m$.

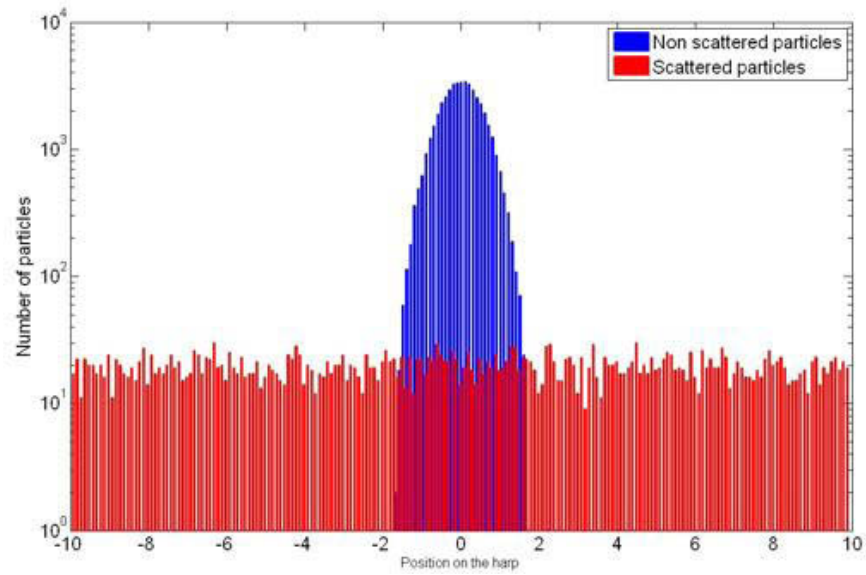


Figure 7.25: Simulated distribution of the particles at the SEM grid for a slit thickness equal to $50 \mu m$ and slit aperture equal to $100 \mu m$ (note the logarithm scale).

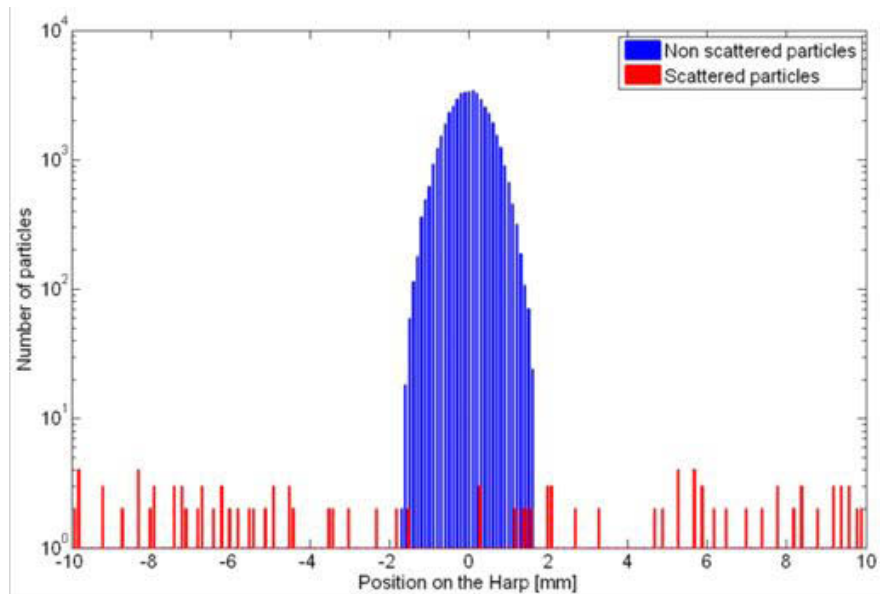


Figure 7.26: Simulated distribution of the particles at the SEM grid for a slit thickness equal to $100 \mu m$ and slit aperture equal to $100 \mu m$ (note the logarithm scale).

Slit thickness [μm]	Transmission of non scattered particles [%]	Percentage of scattered particles after the slit	Percentage of scattered particles reaching the grid
40	0.94	75.6	66.43
100	2.34	55.47	44.28
200	4.67	38.26	28.32

Table 7.5: Percentage of non scattered and scattered particles for different slit aperture with an ideal 0 μm thickness.

The percentage of scattered particles reaching the SEM grid is reduced by a factor 3 if the aperture is increased by a factor 5.

Form these results, it can be expected that the effect of the multiple scattering on the slit edges can be reduced by increasing the slit thickness and/or the slit aperture.

Determination of the slit thickness and scattered particles weight

As mentioned above, FLUKA has been used to simulated a full emittance scan, the parameters for the reconstruction are:

- 27 slits position per scan
- Weight of the non scattered particles equal to 1
- Variable weight for the scattered particles have been used (0,1,2,3,4,5 and 6).
- Design slit aperture (100 μm).

As mentioned in Chapter 5, the scattered particles are stripped and have a lower energy compared to the non scattered particles. The signal polarity is the same for non scattered and scattered particles.

Fig. 7.27, Fig. 7.28 and Fig. 7.29 show the effect of the threshold on the reconstructed emittance for 7 different weights, and 3 geometries. In addition, the reference emittance as reconstructed from the PATH input file is plotted.

- As expected, if the weight of the scattered particles is equal to 0, the emittance is well reconstructed in all the cases, the difference between the FLUKA with respect to the reference curve cannot be distinguished
- For the two cases with thicknesses of 0 and 10 μm
 - Probably not realistic
 - The effect of multiple scattering is very strong and disappears only for threshold above 5% in the better case

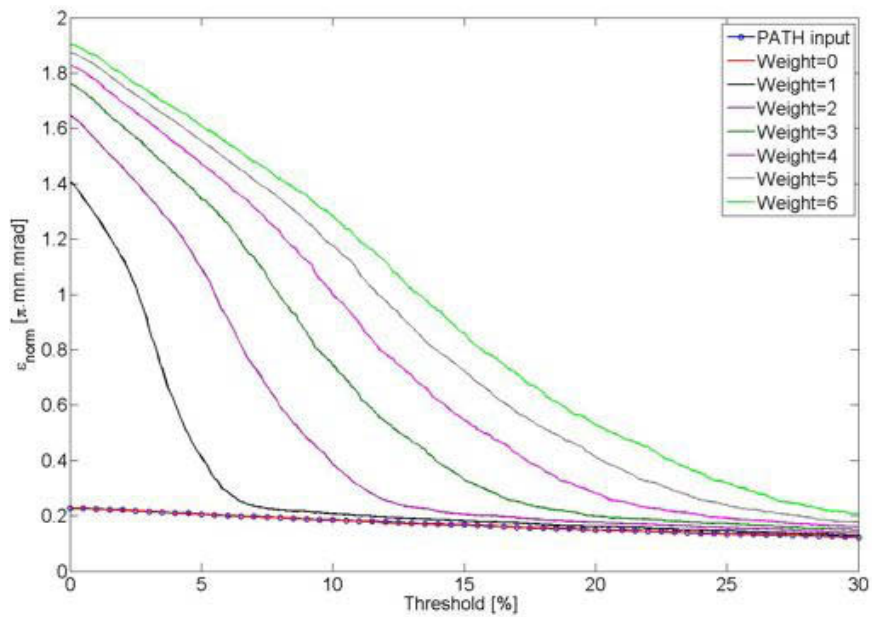


Figure 7.27: Reconstructed emittance as function of the data thresholding, for a slit with $100 \mu\text{m}$ aperture and ideal 0 thickness, when given different weights to the scattered particles.

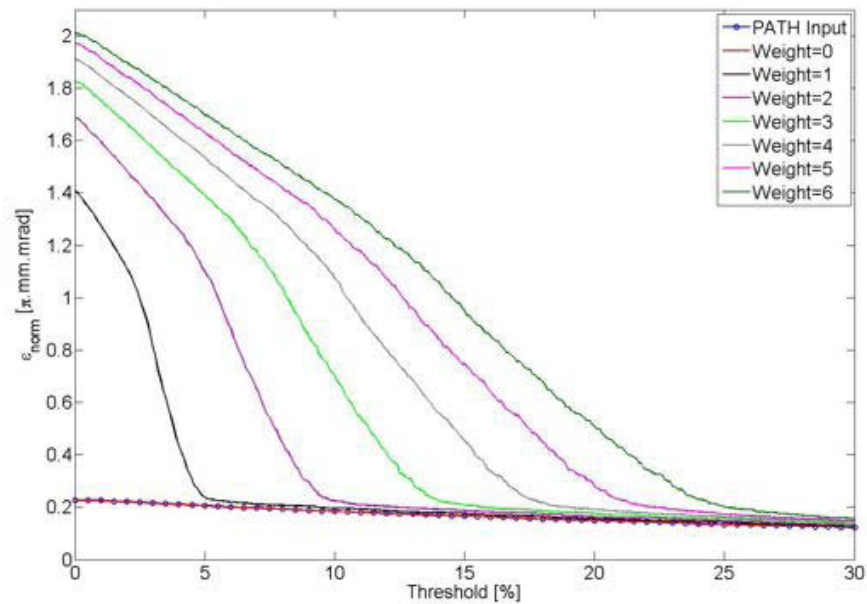


Figure 7.28: Reconstructed emittance as function of the data thresholding, for a slit with $100 \mu\text{m}$ aperture and $10 \mu\text{m}$ thickness, when given different weights to the scattered particles.

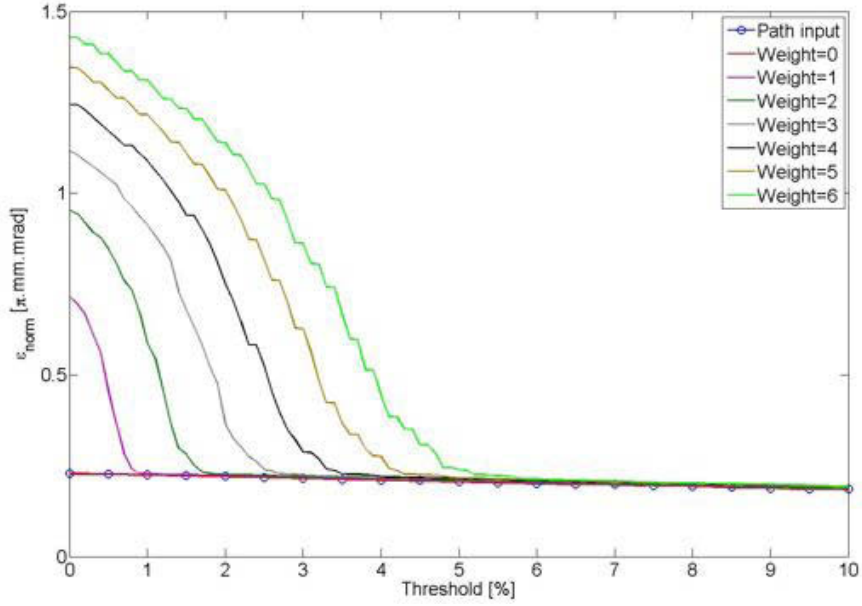


Figure 7.29: Reconstructed emittance as function of the data thresholding, for a slit with $100 \mu m$ aperture and $50 \mu m$ thickness, when given different weights to the scattered particles.

- The best agreement between measurements and simulations is when assuming a slit thickness of $50 \mu m$ and a weight equal to 1.

It was expected a larger signal for the scattered particles die to their lower energy, nevertheless the secondary emission process is probably saturated by the bias polarization (see Section 7.2.2), the charge creation is similar for scattered and non scattered particles, the weight of the scattered particles should be equal to 1.

Reduction of the background signal

Fig. 7.30 shows how the background from scattered particles is indeed expected to decrease by increasing the slit thickness to 100 or $500 \mu m$.

In this case the slit thickness is above the range of $2.5 MeV$ proton in graphite and the error on emittance reconstruction is much smaller. Table 7.6 shows the emittance calculated for a threshold equal to 0 and 1 % and different simulated thicknesses.

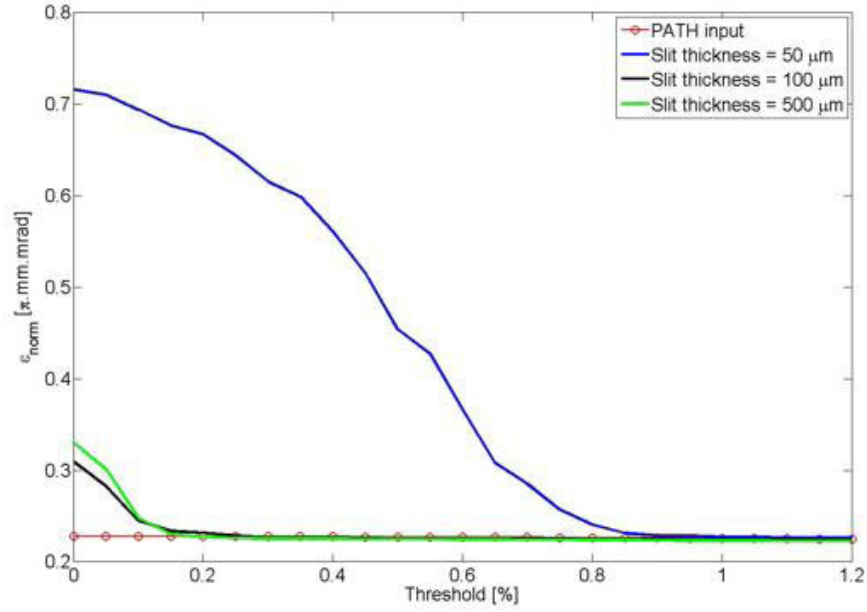


Figure 7.30: Reconstructed emittance for a $100 \mu m$ slit aperture, variable thickness and scattered particles weight equal to 1 as function of the data thresholding.

thickness [μm]	ε	Threshold [%]		ε	$\frac{\Delta\varepsilon}{\varepsilon}$ [%]
		0	1		
0	1.41	516.53	1.28	467.38	
10	1.41	517.36	1.28	465.16	
50	0.72	213.99	0.23	0.62	
100	0.31	35.77	0.22	-0.58	
500	0.33	44.72	0.22	-1.11	
PATH	0.23	0.00	0.23	0.00	

Table 7.6: Reconstructed emittance value for different slit thickness and the design aperture of $100 \mu m$.

Effect of the slit aperture on emittance reconstruction

For a slit thickness equal to 0, a scan has been simulated with a slit aperture of $200 \mu m$. A smaller aperture has not been simulated, the low number of particles passing through the slit would induce a large statistical error. Fig. 7.31 shows the effect of the threshold on the beam emittance for the 2 aperture and the same particle weight.

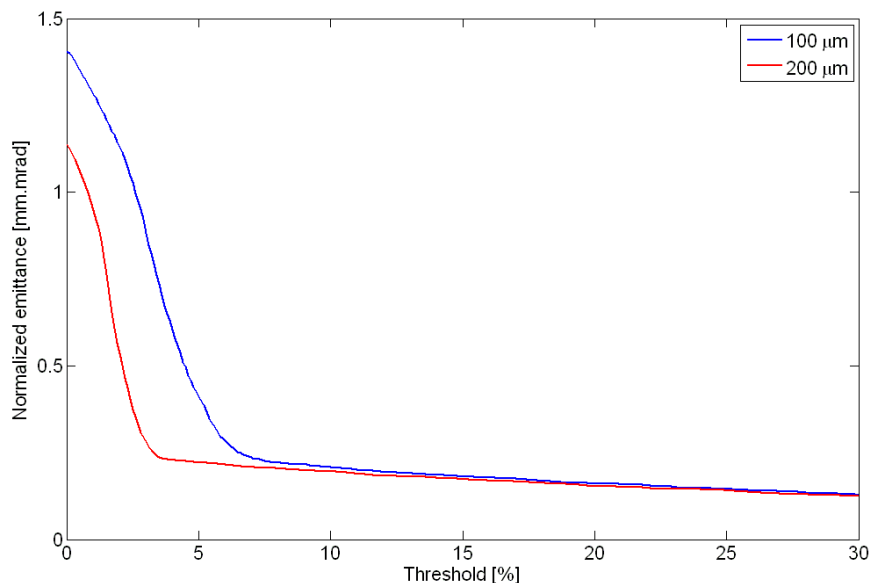


Figure 7.31: Threshold effect for different slit aperture.

The effect of the slit aperture appears clearly on this plot. As shown in Table 7.5 for only 1 slit position, the percentage of scattered particles reaching the SEM grid is reduced with the larger aperture, and so the effect on the reconstructed emittance. However a larger aperture should also induce a larger space charge effect on the emittance reconstruction.

7.3 Summary

LINAC4

The commissioning phase of the emittance meter was very successful with a good agreement between the simulations and measurements of the bias voltage effect. The transverse profile measurements done at the different LEBT commissioning stage was useful to determinate the beam parameters and to benchmark the beam dynamic simulations.

The source development is still in progress and dedicated periods are planned for the next months. In parallel, the commissioning of the LEBT is progressing. An iris and the LEBT chopper has been installed during the summer of 2011, the effect on beam dynamics of these devices will be investigate in fall 2011.

The year 2012 will be dedicated to the RFQ and MEBT commissioning, with the new slit and grid system described in Chapter 5 and Chapter 6.

SNS

Signal coupling can be explained by multiple scattering on the slit edges, but electromagnetic coupling or cross talk in the acquisition chain can not be excluded. The system can be improved by machining a thickness of 100-200 μm on the slit. As shown in Fig. 7.31, this improves the measurement by reducing the number of scattered particles after the slit. This could also be achieved by increasing the slit aperture. The simulations show also the large influence of the slit geometry on the results, the difference between measurements in horizontal and vertical plane can be explained by a larger thickness and/or a larger aperture of the slit in the vertical plane.

Chapter 8

Emittance measurement based on laser and H^0 detection

In order to optimize the injection into the PS booster and reduce the losses, emittance measurements are foreseen at the end of the LINAC4 and as close as possible to the injection region.

A slit and grid system similar to the device installed in the 3 *MeV* test bench is not a good solution for the measurement. At first due to the higher beam energy (160 *MeV*) the slit would have to be very thick (about 200 *mm*) in order to stop the particles. In addition, the thermo mechanical stresses would require a complex slit geometry. One other method is to use 3 screens [45], and reconstruct the emittance from 3 profiles. However, this method presents some issues:

- The pulse length must be reduced from 400 μs to 100 μs to prevent thermal load on the screen.
- A monitor with good resolution ($< 50 \mu m$) is difficult to achieve with standard Chromox screens
- The emittance blow-up in between the screen would be significant, due to the very high particle density needed for the measurement (beam sizes around 300 μm).

A laser wire can be used to neutralize a small amount of the beam as a slit samples the beam, and the beam divergence can be reconstructed by measuring the profile of the neutral beamlet. This solution is similar to a slit and grid system, with a good resolution and accuracy. The advantage is that the beam is not interacting with matter, and any mechanical problem due to thermal load is avoided. The beamlet is not affected by the space charge and the H^0 detector could have enough granularity for the measurement.

8.1 Laser wire-profile measurement.

8.1.1 Principle

Considering H^- ions, the binding energy of the outer electron is about 0.75 eV , and such electrons can be easily stripped with a low energy photon. A laser and an optical system can be used to produce a focused photon beam, which can interact with the H^- beam and scan the beam. After the interaction, the beam contains H^- , H^0 and electrons. A magnetic element can be used to separate the different species (see Fig. 8.1).

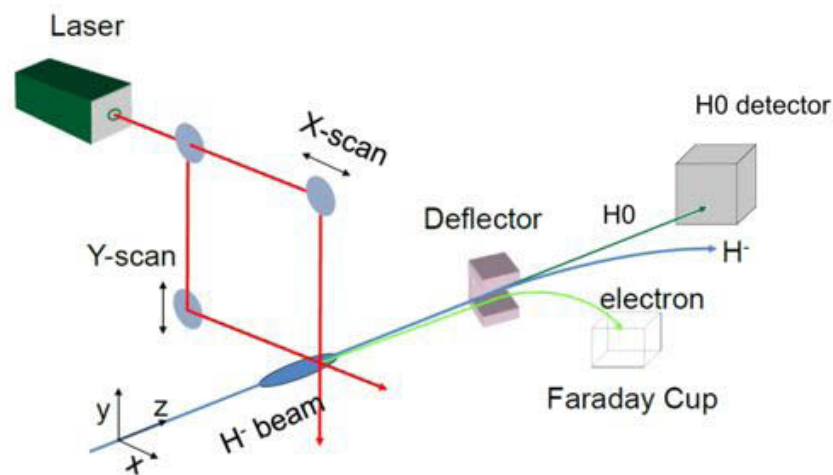


Figure 8.1: Principle of beam profile measurement with a laser wire.

Stripped electrons can be collected by a Faraday cup and beam profile can be reconstructed from the cup measurement. An H^0 detector can be positioned downstream the magnetic element and collect the neutral beam, the phase space rotation induced in the drift space allows to use the system laser+ H^0 detector for emittance measurement as a Slit&Grid system.

8.1.2 SNS laser wire beam profile system

Since few years, the beam profile in the SNS superconductive linac is measured by means of a Q-switched Nd:YAG laser with [46] :

- 10 ns pulse length
- Energy of the pulse 1 J
- Repetition rate 30 Hz

Saturation effects appear after few hundreds of mJ . A laser with a higher energy allows simultaneous measurements at different locations by using beam splitters. Fig. 8.2 shows a laser station for a beam profile at SNS.

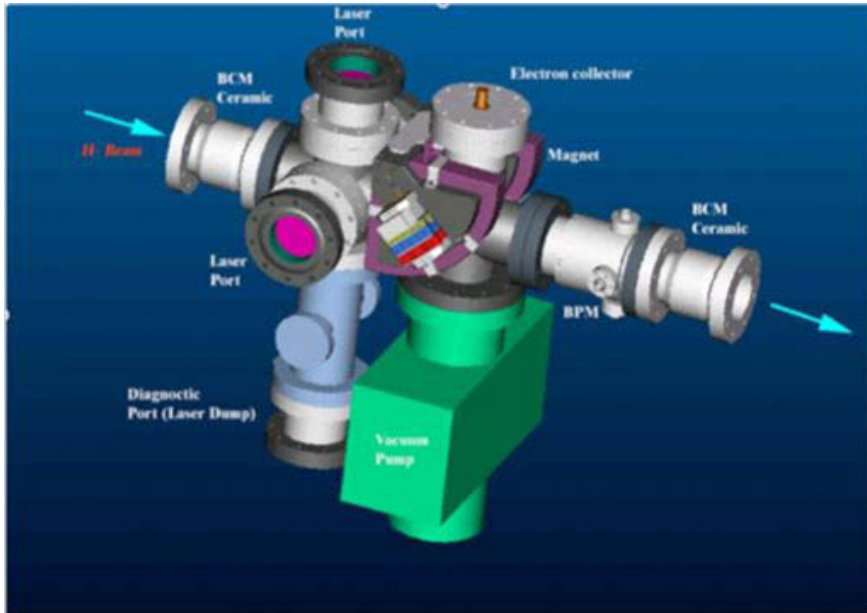


Figure 8.2: Laser profile station used at SNS up to 1 GeV .

The profile is reconstructed by measuring the stripped electrons with a Faraday cup. A small dipole magnet is positioned after the interaction chamber to separate and collect the electrons. A second magnetic element is positioned downstream to correct the orbit distortion induced by the dipole. In addition, a Beam Position Monitor (BPM) is installed on the laser station in order to have a crosscheck of the measurement.

Fig. 8.3 shows the diagram of the laser beam path in the laser station. The laser beam line is several hundred meter long (see Fig. 8.4), a first mirror is used to select the laser wire station (M on the diagram) and a second mirror (FM on the diagram) is used to select the plane of measurement.

With this optical system, the laser beam can be focused to a few tens of microns. The lenses and the mirrors are moved with stepping motors in order to focus the beam and perform the scan. In this configuration, the part of the beam interacting with the center of the laser beam is neutralized.

The laser line is about 250 m long and small variations on the beam jitter have a large effect on the laser position. The measurement accuracy depends strongly on the laser beam position stability. For this reason a feedback system has been developed by the SNS diagnostic group.

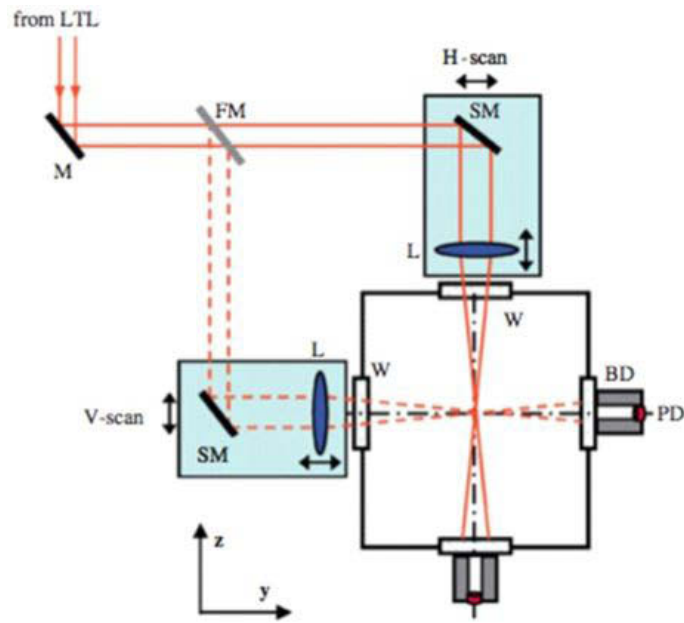


Figure 8.3: diagram of the laser station and laser Beam path.

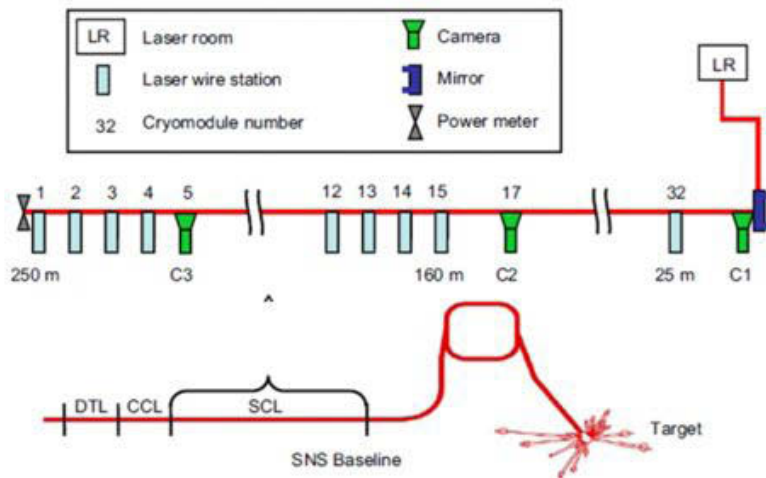


Figure 8.4: Outline of SNS laser wire system.

As shown in Fig. 8.5 a mirror with a picomotor actuator is positioned close to the laser exit, the laser position is monitored at a different location (camera in Fig. 8.4) and the transmission of the laser power is measured at the end of the line. These data are used as input for the feedback system with a speed of few Hz.

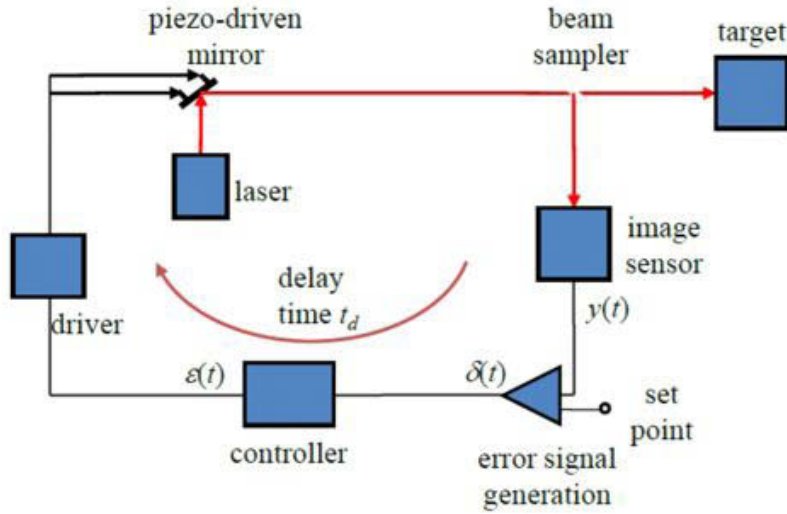


Figure 8.5: Diagram of SNS laser feedback system.

In addition to these laser stations for profile measurement, a new station has been commissioned in 2011 for emittance measurement in the LINAC dump line. The system consists in:

- A laser station positioned upstream a dipole magnet
- A Wire Beam scanner positioned 14 meters downstream the laser station

The laser station has the same design as described above and can perform also profile measurements. The first results of the commissioning can be found in [47].

8.2 Application to LINAC4

At the moment of writing, the transfer line from LINAC4 to the PSB includes two horizontal (closer to the linac) and two vertical bending magnets.

Since it has been decided to measure the beam emittance as close as possible to the end of the linac, the laser station can be positioned just before one of the horizontal bends in the first group of magnet. A diagram of the line in this region and a possible integration of the emittance measurement is shown in Fig. 8.6.

The background particles from the linac (H^0 and protons) mainly generated by beam gas interactions are removed by the first magnet. The line between the two magnets is 14 m long, the magnetic length of the magnet is 1 m assuming a constant field of 1 T without fringe field. For the detection of the neutral particles,

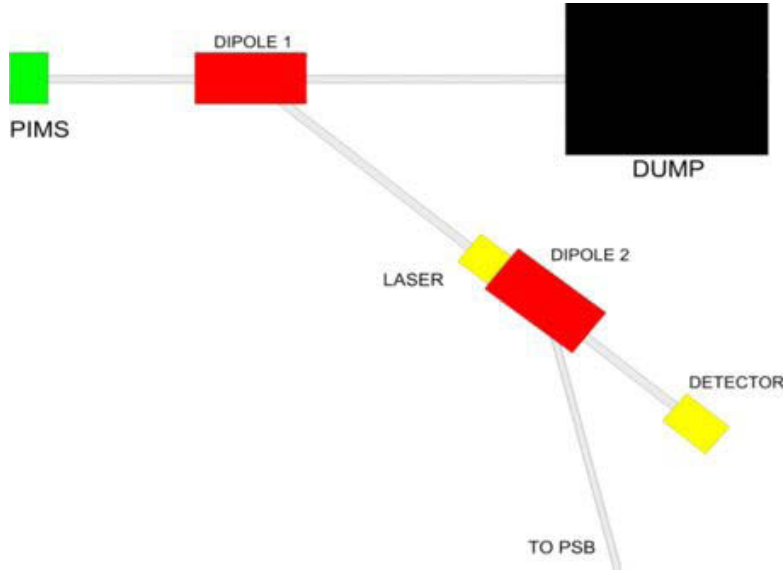


Figure 8.6: Proposal for an emittance measurement after the second horizontal bending magnet.

we assume a detector with an area of $4 \times 4 \text{ cm}^2$, positioned 2 meters downstream the second dipole.

8.2.1 Photo neutralization

The stripping of electron by photons is called photo neutralization. As shown in Fig. 8.7, the cross section is low (in the order of 10^{-17} cm^2). The threshold is at about 0.75 eV and the peak cross section, 4.10^{-17} cm^2 , is at about 1.5 eV .

The photon energy E_{cm} in the H^- rest frame is related to the laser photon energy E_L by the equation:

$$E_{cm} = \gamma_{rel} E_L [1 - \beta_{rel} \cos \theta_L] \quad (8.1)$$

Where θ_L is the laboratory angle of the laser beam relative to the H^- beam.

The wavelength of a Q-switched Nd:YAG laser is 1064 nm , i.e a photon energy of 1.16 eV . Assuming an angle θ_L of 90° , at 160 MeV , the photon energy in the beam rest frame will be 1.60 eV i.e a wavelength of 776 nm , which is closed the cross section peak.

Compared to SNS, the speed of the beam particles is lower in the LINAC4 case, the interaction time is longer and the efficiency of the stripping is higher. The bunch length is longer in case of LINAC4, and the saturation effect is expected be also less important.

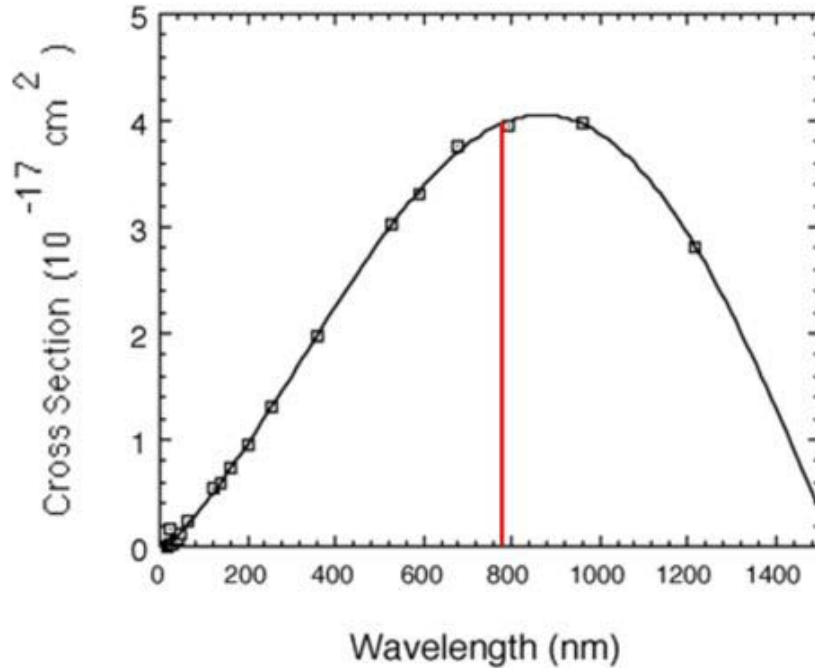


Figure 8.7: Photo neutralization cross section as function of the photon wavelength. In red, the photon energy in the beam frame (Beam energy =160 MeV , $\theta_L = 90^\circ$).

We can assume that the laser can be focused at $100 \mu\text{m}$ and the H^- ions are fully stripped. From this assumption, we can estimate the number of particles stripped by the laser during a pulse, with an error of few tens of percent. With the Twiss parameter of the beam at the end the PIMS structure, a source has been generated in PATH. A slit has been used to simulate the laser beam. At the center of the beam, around $4 \cdot 10^7$ ions are stripped. This number decreases to about of 10^4 on the beam edges. Compared to the number of particles in a pulse (10^{14} ions), this method is non destructive. The H^0 detector must have enough resolution to provide good signal to noise ratio with such a small amount of particles.

8.2.2 Background

During the acceleration along the linac and the travel between the end of the linac and the PS booster, the outer electron can be stripped by black body radiation, magnetic field and residual gas. Part of this neutral beam can reach the H^0 detector and perturbs the measurement.

Black body radiation

The LINAC4 machine is a normal conducting accelerator, and for this study the temperature of all LINAC4 components is assumed to be 300 K. The process of ion stripping by black body radiation is shown in Fig. 8.8.

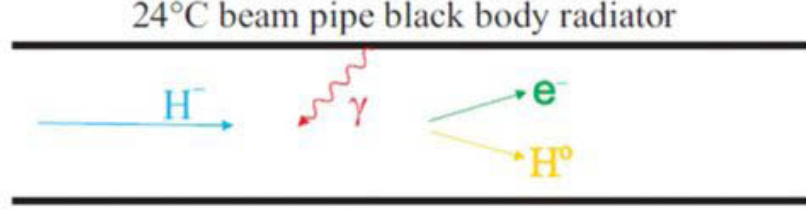


Figure 8.8: Black body stripping

The spectral density of the thermal photons per unit volume emitted by the beam pipe is given by the Planck formula:

$$E(\nu, T)d\nu = \frac{h}{\pi^2 c^3} \frac{\nu^3}{e^{\frac{h\nu}{kT}} - 1} d\nu \quad (8.2)$$

Assuming a temperature of the beam pipe of 300 K, the spectral density is shown in Fig. 8.9.

Without Lorentz boost, the energy of the thermal photons is below the threshold energy for photo neutralization. With the maximum boost (when the beam energy is 160 MeV), the Doppler shift factor is around 1.8. The photons spectral density in the rest frame is also shown in Fig 8.9.

The number of photons with a sufficient energy to induce neutralization is low at the top energy of LINAC4. For the lower energy, the Doppler shift is smaller and even less photons have a sufficient energy to induce stripping. Below 100 MeV, this effect disappears. More details about H^- ions stripping by thermal photons can be found in [48] and [49].

Magnetic field stripping

Another loss mechanism is the magnetic H^- stripping in the dipoles of the transfer line. The effect is caused by the electromagnetic field seen by a moving particle when passing through the magnetic field of a bending magnet. The average lifetime of H^- ions of relativistic parameters $\beta_{rel}\gamma_{rel}$ crossing a magnetic field B perpendicular to the direction of motion is:

$$\tau(B) = \frac{7.96 \cdot 10^{-6}}{\beta_{rel}\gamma_{rel}cB} e^{\frac{4.25610^9}{\beta_{rel}\gamma_{rel}cB}} \quad (8.3)$$

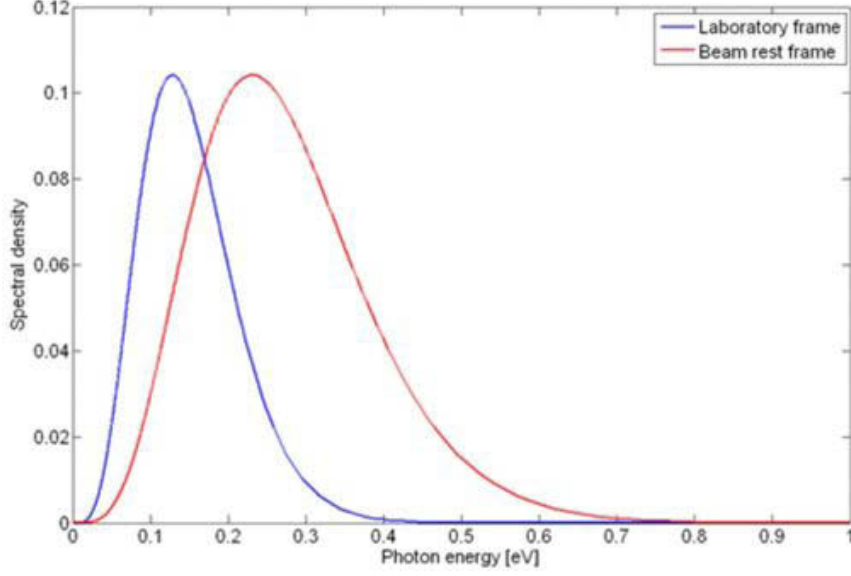


Figure 8.9: Photons spectral density energy in the laboratory frame (blue curve) and Doppler shifted to 160 MeV beam rest frame (red curve) at 300 K.

The stripping probability law is then given as:

$$P = 1 - e^{-\frac{t}{\tau}} \quad (8.4)$$

Where t is the time it takes the particle to traverse the dipole. For $\beta_{rel} = 0.52$, $B = 1T$, and a distance in a magnetic field of 1 m, the stripping probability is 1.1×10^{-5}

Rest gas stripping

The losses induced by H^- stripping in vacuum can be estimated using the formula :

$$P_r = 1 - \exp(-l/\lambda) \quad (8.5)$$

P_r is the probability of losses in a section of length l , where the mean free path λ equals to:

$$\lambda = \frac{kT}{\sigma P} \quad (8.6)$$

with k being the Boltzmann constant, T the temperature, σ the cross-section and P the vacuum pressure.

Stripping cross sections for H^- ions in H, He, N, O and Ar for beam energy of 400 MeV or 800 MeV are available in the literature [50, 51, 52]. These cross section can be scaled to 160 MeV and the values are shown in Table 8.2.

Energy of H^-	Hydrogen	Helium	Nitrogen	Oxygen	Argon
800 MeV	--	--	1	1	3
400 MeV	0.2	0.2	--	--	--
160 MeV	0.376	0.376	2.62	2.62	7.9

Table 8.1: Stripping cross section of H^- ions for typical rest gas molecules (unit= $10^{-18}cm^2$).

To be conservative, we assume that the residual gas is only composed of Nitrogen.

From Eq. 8.6 the stripping probability at 160 MeV per meter is 6.5×10^{-7} .

Total background on the detector

Considering the layout of Fig. 8.6, the number of background particles due to residual gas stripping is 9.1×10^8 for a pulse of 10^{14} ions. The number of background particles due to the magnetic field stripping in the bending magnet is 10^9 , and due to geometrical consideration, only the neutral particles generated in the first 15 cm of the bending magnet are able to reach the H^0 detector, results in 3.3×10^7 particles. We also assume that these particles have the same distribution as the particles beam distribution at the magnet entry. In total 6.87×10^8 particles are reaching the target, 10 times more than the number of particles generated by the laser pulse.

More simulations have been done with different length of the line, in order to simulate the effect of a bending magnet splitted in two part. The results are shown in Table 8.2 and in Fig. 8.10.

Drift length [m]	Number of particles
14	6.87×10^8
0.5	5.80×10^7
0.3	4.59×10^7
0.2	3.94×10^7

Table 8.2: Number of background particles reaching the detector.

Fig. 8.10 shows the background particles distributions in the horizontal plane for the different drift lengths and the distribution of particles generated by the laser pulse.

The number of particles is integrated over a pulse, and in this case the background is an issue for the measurement, even if the drift length between the two

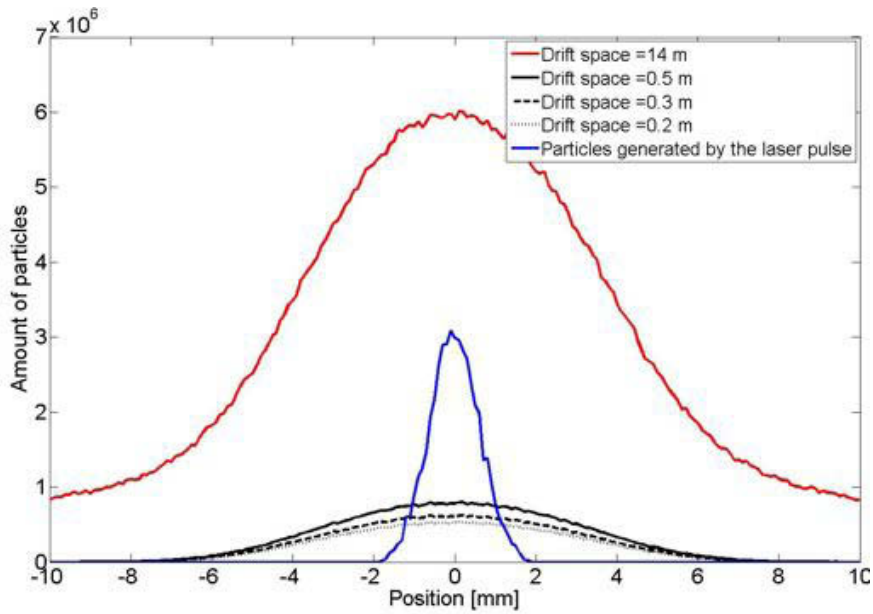


Figure 8.10: Particles reaching a detector positioned 2 m downstream the dipole.

magnets is reduced to less than 1 meter. The background particles are generated over $400 \mu s$, if we assume that the probability of stripping by residual gas interaction or magnetic field stripping is constant during the LINAC4 pulse, while the particles useful for the measurement are generated over a laser pulse, i.e. $10 ns$.

By gating the signal with a short time window, the background effect can be reduced. Assuming a window of $20 ns$, the number of particles reaching the detector is the same for the laser signal, but for the background particles the number can be reduced by a factor 20000 (see Table 8.3 and Fig. 8.11).

Drift length [m]	Number of particles
14	3.44×10^4
0.5	2.90×10^3
0.3	2.30×10^3
0.2	1.97×10^3

Table 8.3: Number of background particles reaching the detector every $20 ns$.

In this case the signal over noise ratio is more than 10^4 . The measurement will not be affected by the background, even when the laser is positioned at the beam edges (see Fig. 8.12).

In order to gate the signal in a very short time window, the H^0 detector must

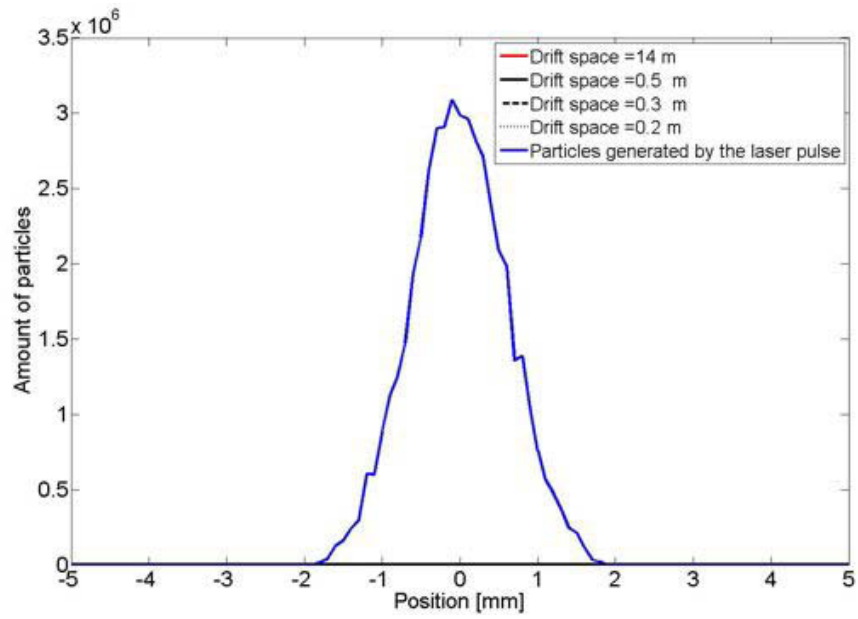


Figure 8.11: Particles reaching a detector positioned 2 m downstream the dipole for laser wire positioned at $x=0$.

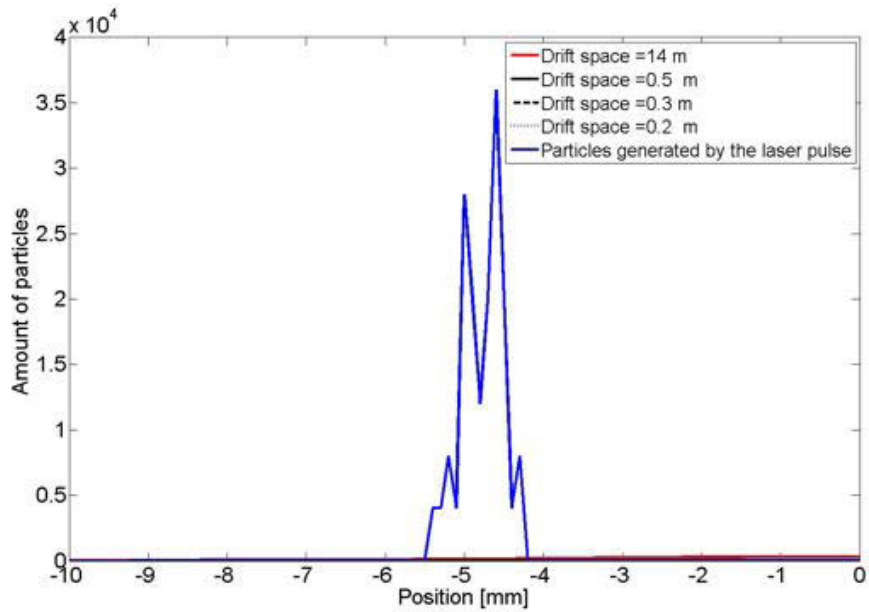


Figure 8.12: Particles reaching a detector positioned 2 m downstream the dipole for laser wire positioned at the beam edge.

have a fast time response. It must also have a good resolution and good signal/noise ratio to detect profile with a low number of particles, a solid state detector has all these characteristics.

8.2.3 H^0 detection

Solid state detector

Solid state detectors have been used in experimental physics for more than 40 years. Over the last 25 years Silicon detectors have become more and more important, first in high energy physics and now in other fields.

The advantages of these detectors are:

- Only a few eV energy spent to create one information (charge) carrier. This implies a large number of charges per single particle crossing the detector.
- Compact size: the detector thickness is about few hundred micrometers.
- Very high spatial resolution.
- High number of channels.

Generally, most Silicon detectors make use of reverse biased p-n junction. Two semiconductors (one of n type, the other of p type) are in contact at the junction, the band structure is deformed and a potential appears. In the transition zone, there is no free charge, this zone is called depletion region (see Fig. 8.13).

Due to the electric field in the depletion region, electron and hole pairs generated by photons or charged particles drift in this field and give a current or charge signal. The region can be increased by applying a reverse bias voltage on the detector. The depletion voltage is the voltage created by the charged ions at the junction and is noted as V_{dep} . This voltage is determined by the electron and hole concentration and the detector thickness:

$$V_{dep} = \frac{q_0}{\varepsilon\varepsilon_0} |N_{eff}| d^2 \quad (8.7)$$

Where N_{eff} is the effective space charged density, d the detector thickness and ε the Silicon permittivity.

The depletion depth w can be calculated as:

$$w = \frac{2\varepsilon\varepsilon_0}{q|N_{eff}|} (V_{bias} + V_{dep}) \quad (8.8)$$

By applying a bias voltage V_{bias} the depletion depth can be increased to the thickness of the detector.

An example of microstrip detector is shown in Fig. 8.14.

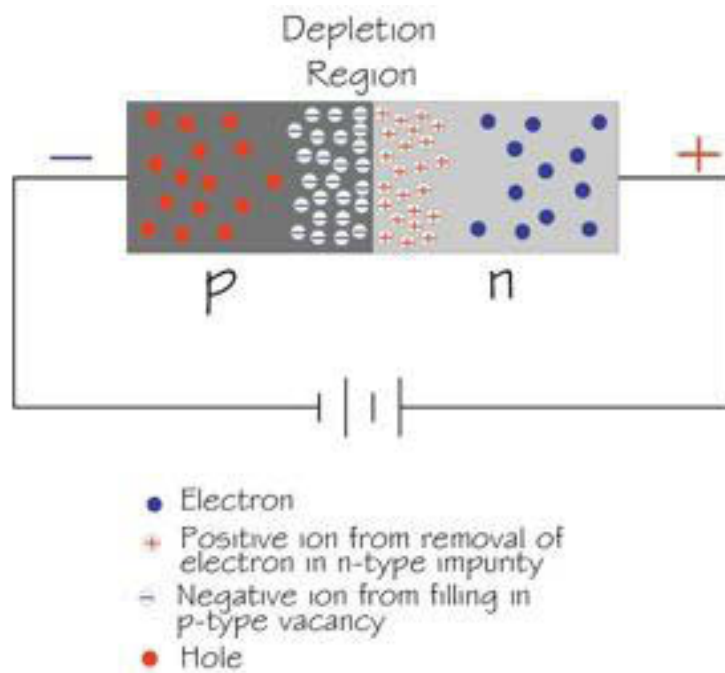


Figure 8.13: Silicon diode junction principle.

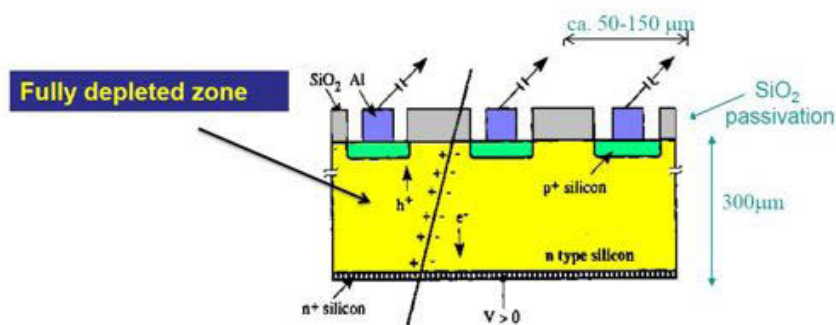


Figure 8.14: Typical microstrip Silicon detector used for particles tracking.

11000 electrons-hole pairs are created by a minimum ionizing particle (detector thickness $\approx 100 \mu m$), typical value set for bias voltage are around few hundred of Volts.

Since few years, Diamond detectors are developed for high energy physic applications. Due to the large band gap the density of free charges in diamond is smaller compare to Silicon and this detector can be used at room temperature as

an ionization chamber. An example is shown in Fig. 8.15.

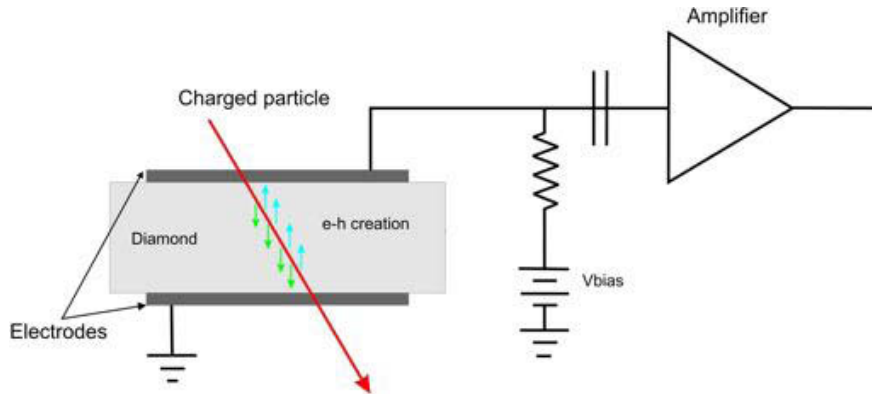


Figure 8.15: Schematic view of a diamond detector.

If there is an electric field, like in the depleted space charge region of a p-n junction device or due to the bias voltage in case of a Diamond detector, the charges have a component of movement (drift) along the direction of the electric field (\vec{E}) with velocity

$$v_e = \mu_e E \quad (8.9)$$

$$v_h = \mu_h E \quad (8.10)$$

Where v_e and v_h are respectively the electron and hole mobility. With typical detector thicknesses ($< 500 \mu m$) and the velocities shown in Table 8.4, the signal can be collected in few nanoseconds.

Performance of Silicon and Diamond detector

A microstrip Silicon or Diamond detector can achieve a time response in the order of nanoseconds and a sufficient signal level for the emittance measurement. Depending on the H^- beam parameters, the resolution of the detector can be modified by the pitch of the strip and the length of the drift space between the laser and the detector. The relevant parameters for these types of detectors are shown in Table 8.4.

In Diamond detectors both electrons and holes can be used for fast measurements.

	Silicon	diamond single crystal	diamond polycrystal
Band gap [eV]	1.1	5.47	5.47
Breakdown field [$MV.cm^{-1}$]	0.3	10	10
Electron mobility [$cm^2V^{-1}s^{-1}$]	1450	4500	1800
Hole mobility [$cm^2V^{-1}s^{-1}$]	480	3800	1000
Ionization energy [eV]	3.62	13	13

Table 8.4: Relevant parameters for Silicon and Diamond Detectors.

Radiation hardness of the detector

Concerning the radiation hardness of the detector, Table 8.5 shows the lifetime of solid state detectors.

Detector type	Silicon	Diamond	Diamond
Radiation Hardness [$proton.cm^{-2}$]	10^{12}	10^{15}	10^{17}
Lifetime	0.5h	152 days	42 years

Table 8.5: Radiation hardness and lifetime of different material.

For this calculation we assume 3 hours of measurement per day, 7 days per week. It can be seen that the Silicon lifetime is relatively short to be used in accelerators.

Scattering effect and profile reconstruction error

When H^0 particles hit the diamond, the electron is stripped in the first few micrometers and stops in about $40 \mu m$, Fig. 8.16 shows the energy deposition of a $90 keV$ electron beam on diamond. The electron energy deposition and its chaotic trajectory can have an influence on the measurement.

FLUKA simulations have been done in order to estimate the error on the profile due to electron scattering inside the detector. The beam profile has been reconstructed from both energy deposition in the detector (by using a Cartesian mesh) and from the position of the electrons at the detector surface.

The error between the two profiles is less than 0.1 %. Nevertheless the Monte Carlo simulations are not able to track electrons with a kinetic energy less than a keV and a second design of the H^0 detector has been considered. A thin foil can be used as a stripper and a dump for the electron of H^0 in order to avoid signal from the stripped electrons in the detector. A simple geometry has been simulated

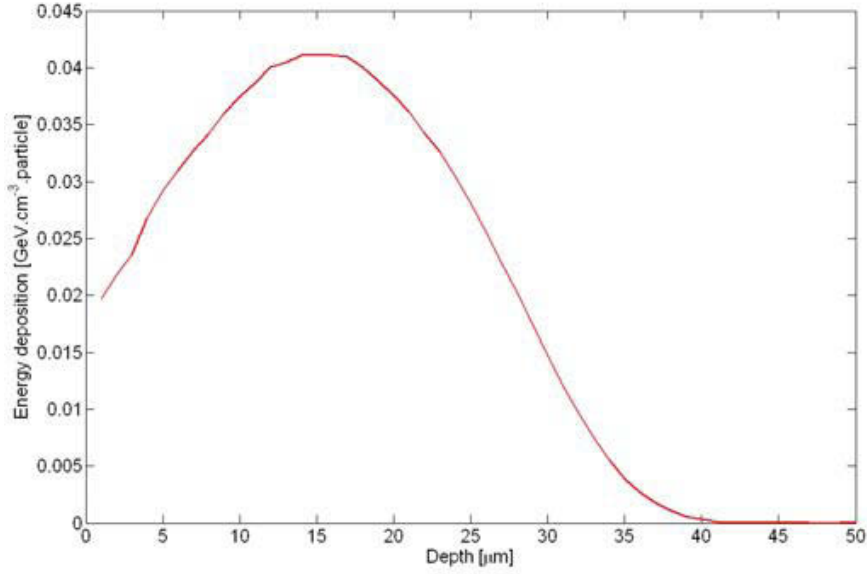


Figure 8.16: Energy deposition of a 90 *keV* electron beam on diamond.

in FLUKA in order to estimate the effect of the multiple scattering of proton in the foil and the detector:

- A stripping foil is positioned upstream the detector. This foil consists in a 100 μm thick Tungsten blade (10 times larger than the range of 90 *keV* electrons).
- A 160 *MeV* proton beam has been generated in FLUKA,
- Beam profiles have been reconstructed with particles positions at the entry of the foil and at the exit of the detector

The error on profile reconstruction due to multiple scattering for different distance between the two components is shown in Table 8.6

Distance [cm]	0	1	2	3	4	5	10
error [%]	0.01	0.74	2	3.88	6.42	9.36	30

Table 8.6: Error in the beam profile due to multiple scattering in the stripping foil and the detector.

The error on the reconstruction increases with the distance between the foil and the detector, when both components are in contact the error is about 0.01 %. From these results, it can be concluded that the foil has no influence on the beamlet

reconstruction (with the foil and the detector in contact), this solution prevents also any error due to stripped electrons.

From the results presented in Table 8.6, we can also conclude that the H^0 detector can not be installed in air, the multiple scattering in the vacuum window and the drift between this element (several cm) lead to a large error on the beam size reconstruction.

8.3 Conclusion

The transverse beam profile and emittance measurements with a laser wire have several advantages:

- Non destructive measurement, the losses due to the laser is below the losses induced by residual gas or magnetic stripping.
- No material interacts with the H^- beam, consequently, the measurement can be done with the full LINAC4 beam power.
- As a wire beam scanner or slit and grid system, the measurement is flexible and accurate:
 - The laser beam can be focused to 10-20 μm .
 - The resolution of the H^0 detector can be increased by modifying the pitch strip and the drift.
- For emittance measurement, the space charge effect is avoided, a drift as long as possible can be used.

However, this method presents some issues. The laser system is complex and it can take time to be fully operational. The experience of the SNS beam diagnostic group can be very useful for the design and commissioning phases. The feedback system must be implemented at the early phase of the design. The diamond detector must be tested in order to demonstrate the accuracy and reliability of the system for profile measurement. In order to test the detector a contract between CIVIDEC [53] and CERN has been signed:

- CIVIDEC will provide a $20 \times 20 \times 0.5mm^3$ polycrystalline CVD¹ diamond detector with 5 readout strips on one side and a common BIAS plane on the other (see Fig. 8.17).
- CIVIDEC will provide 5 analog fast front end amplifiers (40 dB 2GHz).
- CERN will have to provide the counting/sampling electronics with the corresponding software.

1. Chemical Vapor Deposition

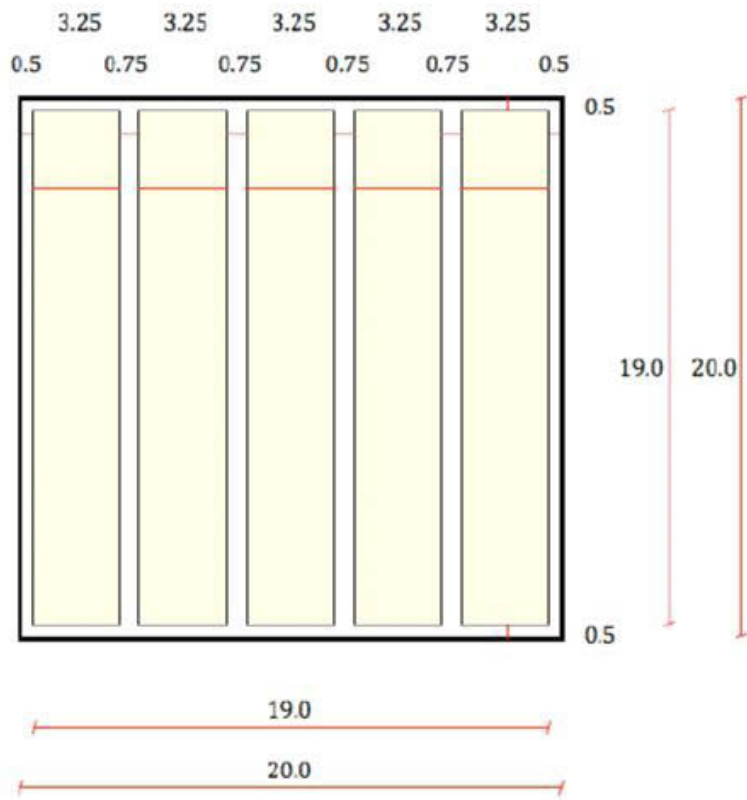


Figure 8.17: Layout of the diamond detector, dimensions are in mm.

The beam tests are foreseen in late 2011 early 2012.

Chapter 9

Conclusions

Designing beam diagnostic for high intensity hadron machines is very challenging. In particular the constraints on intercepting devices are a concern, due to the large energy deposition in matter. The LINAC4 beam instrumentation is not an exception, and the thermal load is the main issue for profile and emittance monitors.

Concerning the profile monitors to be installed at the 3-12 *MeV* test bench (see Chapter 4), the thermal load on the SEM grids used for emittance and energy spread measurements can be neglected. Most of the beam power is absorbed by the slit. Therefore, the wire material choice does not depend on the thermal load, but is related to the signal amplitude. At 12 *MeV*, the signal is similar for 33 μm diameter Carbon wires or 40 μm diameter Tungsten wires. At 3 *MeV*, due to the lower SEY the Carbon wires provide a larger amplitude and should be used in case of H^- beam. For proton beam at 3 *MeV*, the difference is smaller and both materials can be used.

For all profile monitors that will be permanently installed in the LINAC4 tunnel, above 50 *MeV*, a compromise between the signal amplitude and the thermal load must be found. Carbon wires can stand the full beam intensity, but the signal starts to drop around 100 *MeV* and becomes 10 times smaller than a Tungsten wire at 160 *MeV*. Biased Tungsten wires can provide a signal that doesn't depend on beam energy (i.e. the signal is given by the charge deposition only), but the LINAC4 beam power must be reduced in order to avoid wire damages. Given such assumptions, two solutions can be proposed:

- Use Tungsten wires at all energies and operate at lower power (40 *mA* and 100 μs).
- Use Carbon wires below 100 *MeV* with full beam power and Tungsten wires

at higher energies and low beam power.

Concerning the wire scanner monitors to be installed in the 3 MeV chopper line, Carbon provides a better signal than Tungsten . In this case (no slit) also at 3 MeV and with Carbon wires the beam power must be reduced to 100 μs and 40 mA in order to preserve the wire integrity.

Cross talk between wire due to stripped electrons can be an issue for H^- beam profile measurements with SEM grids and wire scanners. Monte Carlo simulations have shown that the profile reconstruction with SEM grid is possible within an accuracy of less 1 %. For the wire scanner, the experience at SNS shows that a design similar to the LPI design is not suitable. The design has to be changed in order to separate the wires and perform the measurement separately. A diagram of the new system is shown in Fig. 9.1.

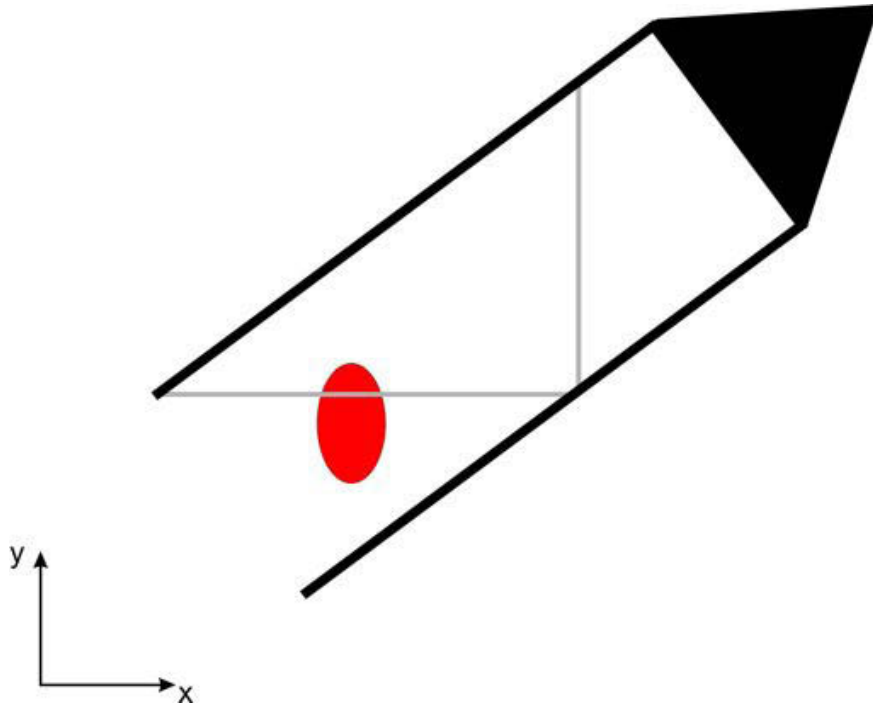


Figure 9.1: Diagram of the proposed new fork design for the LINAC wbs.

For SEM grid and wire beam scanner, due to the thermal load on the wire, it has been decided to have an on line test of the wire integrity. The electronic and mechanical design has been modified to integrate this test.

The design of the new slit for the emittance measurements at 3 and 12 MeV

has been completed and the device is being fabricated at the moment of writing (see Chapter 6). In order to cope with the high energy deposition density it has been decided to use Graphite blades inclined of 15° with respect to the beam axis. Even with the commissioning beam ($100 \mu s$, $65 mA$), it is expected to approach the Graphite thermo mechanical limits, it is advised to start the commissioning with even more reduced power (e.g. $50 \mu s$, $40 mA$).

When reconstructing the emittance (see Chapter 5), the systematic error due to multiple scattering and space charge can be reduced to 2-3 % by using a slit aperture of $100 \mu m$ and applying a background subtraction on the data (this last point is already implemented in the emittance data analysis application).

For emittance and profile measurements at $160 MeV$, the photo neutralization cross section is maximum when using a laser wavelength of $1064 nm$, the background in case of emittance measurement can be removed by gating the signal, therefore a fast detector is required. Several locations has been proposed for the installation of the laser station and the H^0 detector (see Chapter 8). The H^0 beamlet profile can be reconstructed by a Diamond detector, this type of detectors are enough radiation hard and fast for this purpose, in addition, a crosscheck with conventional methods needs to be installed.

The experimental results of the LINAC4 ion source and LEBT instrumentation are encouraging (see Chapter 7). The measurements and the simulations show a good agreement, the different Faraday cups installed in the LEBT allow the determination of the beam transmission in the line. The emittance meter has been used to determine the solenoid current for the beam matching on the RFQ entry and to determine the steerer settings. When the source is running in proton mode and with an extraction voltage of $45 kV$, the normalized emittance varies from 0.07 to $0.29 \pi.mm.mrad$, a dependency of the emittance on the source RF power has been demonstrated. It has to be noted that aperture limitation appears for injected RF power above $50 kW$.

The beginning of 2012 will be dedicated to the commissioning of the RFQ and then of the chopper line.

Appendix A

Appendix: Effect of stripped electron on profile measurement

A.1 Introduction

When H^- ions interacts with matter the outer electron is stripped almost immediately. These electrons can be considered free with an energy of:

$$E_e = \frac{E}{1836} \quad (\text{A.1})$$

where E is the energy of the H^- beam.

For LINAC4 the stripped electrons energy ranges from about 25 eV at the source exit to about 87 keV at the end of the linac. Considering the above energy range and the materials considered for the LINAC4 wires, some data about the electron scattering can be found in literature [17, 35, 36]. For electron energies below the MeV range, the proportion of backscattered electrons is around 10 % for low Z material and up to 50 % in case of material with high density.

In order to estimate the influence of these backscattered particles on the performance of the SEM grid and WBS in the LINAC4 line (for beam energies above 50 MeV), we performed Monte Carlo simulations with different wire materials and geometry considering directly electron beam distributions as source. Below 50 MeV beam energy (e.g. $3\text{ MeV } H^-$ beam for the wire scanner installed in the chopper line), the electrons energy is too small to have reliable results with FLUKA.

A.2 Cross talk between two wires due backscattered electrons

The first FLUKA simulation consisted in two parallel wires of the same material and diameter separated of $500\ \mu\text{m}$, as shown in Fig A.1. A beam composed by 10^6 electrons, with a rectangular shape of width equal to the wire diameter has been sent to one wire in order to investigate the amount of scattered particles reaching the second wire. The simulation has been repeated varying the following parameters:

- Electron beam energy equal to $27\ \text{keV}$ or $87\ \text{keV}$, corresponding to $50\ \text{MeV}$ and $160\ \text{MeV}$ H^- energy respectively.
- $33\ \mu\text{m}$ Carbon wires or $40\ \mu\text{m}$ Tungsten wires.

The angular distribution of the particles emerging from the first wire can be reconstructed from the particle flux on a cylinder centered on the wire axis revol. Simultaneously, the number of particles entering and exiting each wire and their energy can be scored. Fig A.2 shows the angular distribution of the particles emerging from the first wire for the four simulated settings.

At the position of the second wire (i.e. 90° or symmetrically 270° on the figure), the ratio of particles vary from 2×10^{-4} to 3×10^{-3} . The ratio drops for angles between 90° and 270° and reaches its minimum for an angle equal to 180° .

In the case of Tungsten wires the angular distribution seems to be independent of the beam energy for the range considered, and at 180° the flux is less 10^{-5} for both the considered energies. For Carbon wires, at the lowest energy, the flux is around 10^{-5} at 180° . At $87\ \text{keV}$ some electrons have enough energy to cross the wire, 44% of the particles exiting the wire have angles between 150° and 210° . Table A.1 shows the percentage of scattered electrons emerging from the first wire and how many of them reach the second wire.

For a Tungsten wire, the amount of scattered electrons emerging from the first wire is about 55% at both energies and in the worst case less than 0.7% reach the second wire.

For a Carbon wire and $27\ \text{keV}$ electrons, about 17% of the impinging particles are scattered, while at $87\ \text{keV}$ the amount of scattered electrons is hardly distinguishable from the ones traversing the wire. At both energies, it can be estimated that the percentage of scattered electrons reaching the second wire is below 0.3%.

Fig A.3 and Fig. A.4 show the energy spectrum of particles emerging from the first wire and the one of particles entering the second wire, in case of $40\ \mu\text{m}$ Tungsten wires. The distributions have a similar shape, proving that scattering angle and electron energy are uncorrelated.

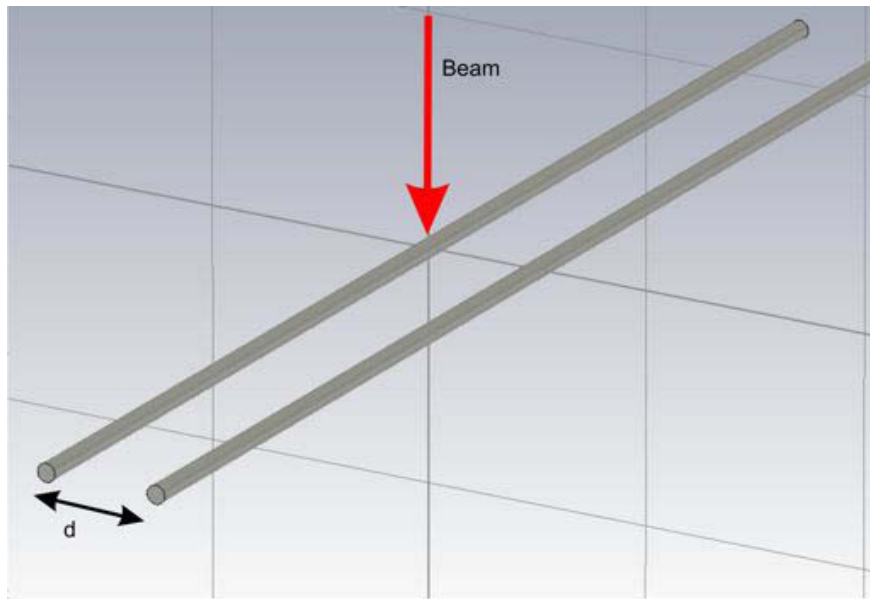


Figure A.1: FLUKA model consisting of two parallel wires separated of $d=500 \mu m$.

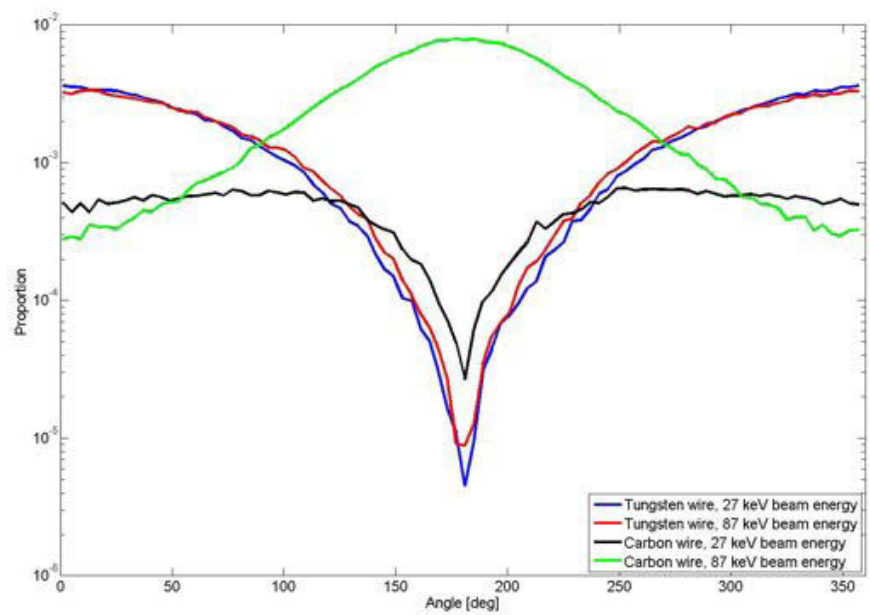


Figure A.2: Angular distribution of particles emerging the wire, normalized to the number of primary electrons.

	Carbon ($33 \mu m$)		Tungsten ($40 \mu m$)	
Energy [keV]	27	87	27	87
$\frac{N_1}{N_{tot}}$	17 %	N.A.	55 %	55 %
$\frac{N_2}{N_{tot}}$	0.24 %	0.05 %	0.6 %	0.66 %

N_{tot} = electrons hitting the first wire

N_1 = scattered electrons emerging form the first wire

N_2 = scattered electrons emerging from the first wire
and reaching the second

Table A.1: Percentage of scattered particles that emerging from the first wire reach the second.

As a conclusion of this first simulation, it can be assessed that looking at each wire of a SEM grid monitor, a meaningful amount of stripped electrons are scattered away from the first wire (thus degrading the wire signal), but only a small amount of them are expected to intercept the neighboring wires.

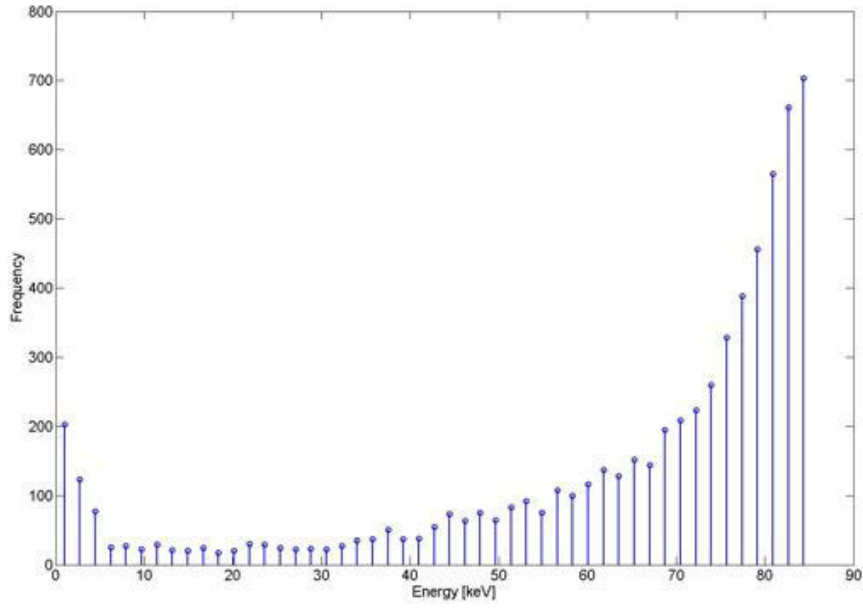


Figure A.3: Energy spectrum of scattered electrons emerging from a $40 \mu m$ Tungsten wire ($87 keV$ electron beam energy).

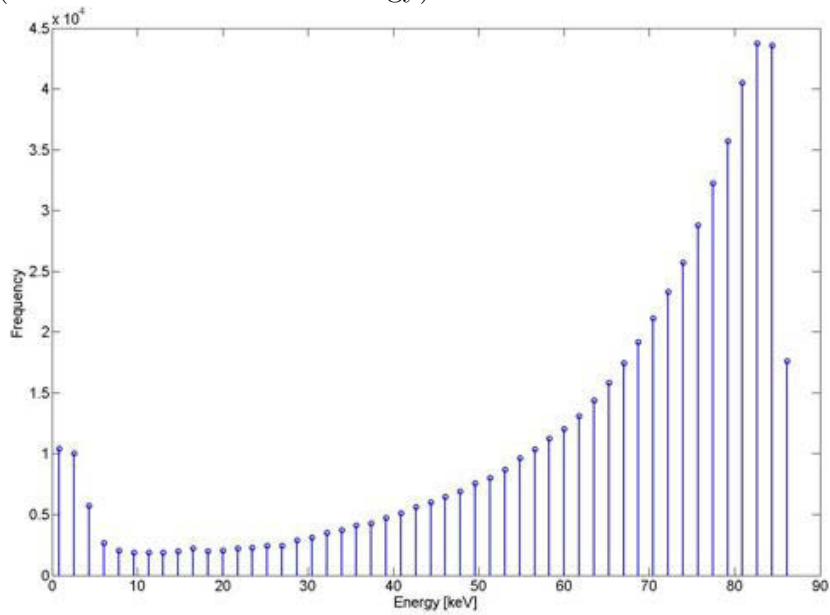


Figure A.4: Energy spectrum of scattered electrons reaching a $40 \mu m$ Tungsten wire positioned at $500 \mu m$ from an identical wire ($87 keV$ electron beam energy).

A.3 Error on profile reconstruction with SEM grid and effect on the signal due to cross talk

A.3.1 Error on profile reconstruction

To investigate more in detail the effect of stripped scattered electrons, a full profile measurement using SEM grids has been simulated in FLUKA. The simulation parameters were:

- SEM grid with 24 wires and 500 μm pitch.
- 33 μm Carbon wires or 40 μm Tungsten wires.
- A Gaussian electron beam has beam with a kinetic energy of 27 keV or 87 keV (corresponding to 50 MeV and 160 MeV H^- energy respectively), with beam sizes $\sigma_x=\sigma_y=2$ mm).

The beam profile has been reconstructed from the net charge stopped in the wire. This net charge is the difference between entering and exiting particles from each wire. This corresponds to the principle of measurement proposed for LINAC4 SEM grid measurements with polarized wire in order to suppress the Secondary Emission (SE).

In addition, a simulation has been done in order to have a reference profile. In this case, the particle tracking is stopped as soon as the electron interacts with matter, thus reproducing the ideal case without scattering.

The beam profiles reconstructed from the simulations are show from Fig. A.5 to Fig. A.8.

Fig. A.9 summarizes the error on the profile reconstruction (Gaussian fit) as function of the electron energy.

In all cases, the beam profile is reconstructed with an error of less than 0.5 %. The worst case is for Carbon wires at high energy, where a large number of electrons have enough energy to cross the wire.

A.3.2 Effect on the signal

In an ideal case (biased wires), the signal on the wire is independent of the beam energy and is determined by the charge deposition of all electrons interacting the wire. From the simulation used to estimate the reference profile, the ideal signal on the central wire, when assuming a 40 mA H^- beam, is:

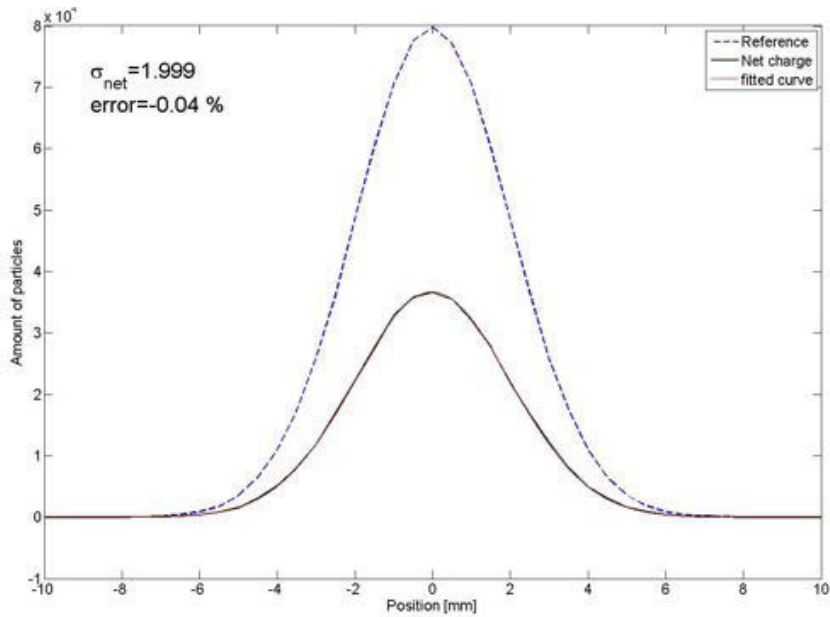


Figure A.5: Beam profile reconstruction without backscattering effect (dashed blue curve) and with backscattering effect (black curve, Gaussian fit in red) for a $40 \mu\text{m}$ Tungsten wire at 27 keV electron beam energy.

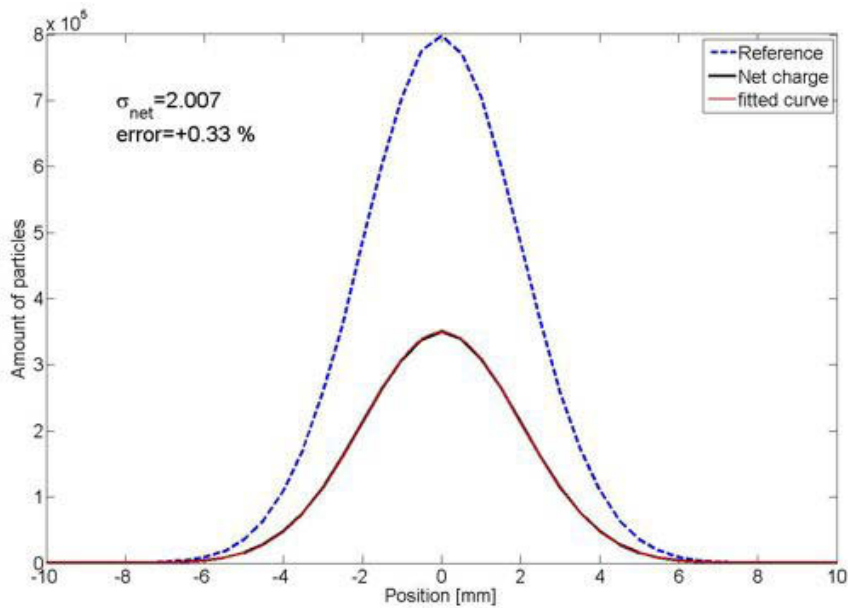


Figure A.6: Beam profile reconstruction without backscattering effect (dashed blue curve) and with backscattering effect (black curve, Gaussian fit in red) for a $40 \mu\text{m}$ Tungsten wire at 87 keV electron beam energy.

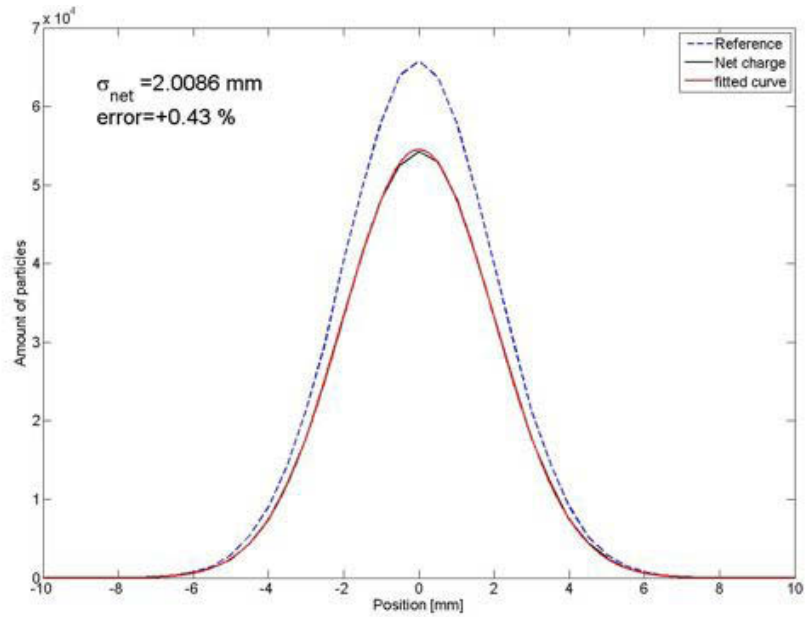


Figure A.7: Beam profile reconstruction without backscattering effect (dashed blue curve) and with backscattering effect (black curve, Gaussian fit in red) for a $33 \mu\text{m}$ Carbon wire at 27 keV electron beam energy.

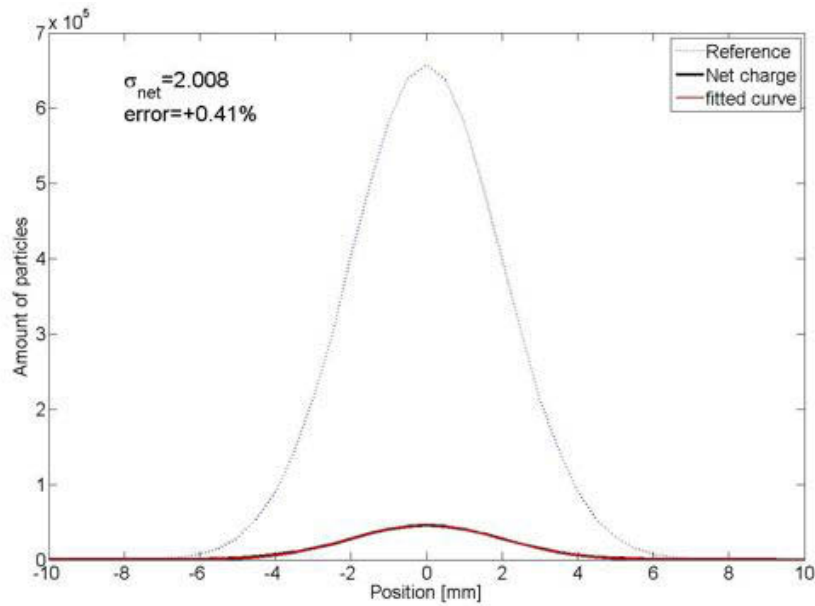


Figure A.8: Beam profile reconstruction without backscattering effect (dashed blue curve) and with backscattering effect (black curve, Gaussian fit in red) for a $33 \mu\text{m}$ Carbon wire at 87 keV electron beam energy.

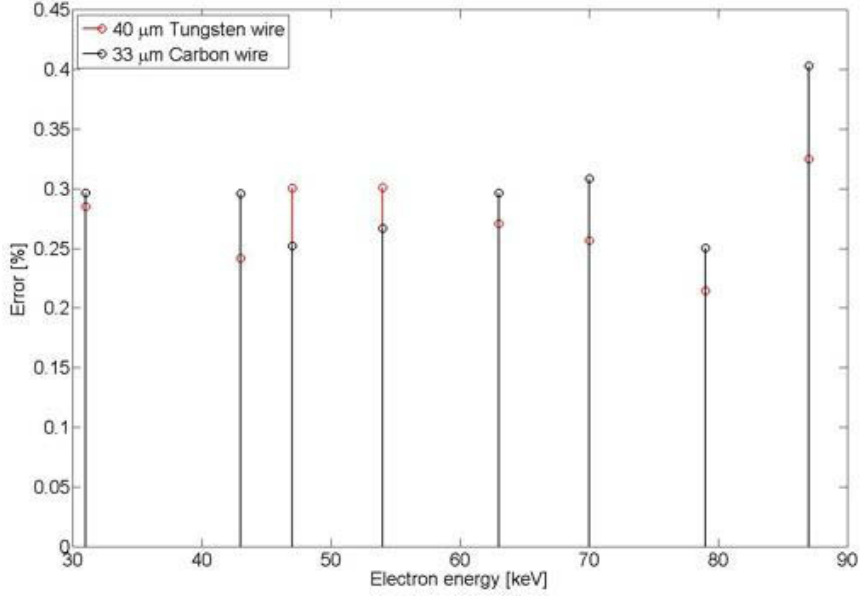


Figure A.9: Beam profile reconstruction error as function of energy.

- 0.64 mA when considering Tungsten wires (constant with energy when biasing the wire)
- 0.52 mA when considering Carbon wires¹

On the other hand, the expected signal on the central wire as simulated by FLUKA (i.e. accounting for the stripped electrons scattering) is shown in Table A.2 for Tungsten and Carbon wires for different energies.

The signal for Tungsten wire is reduced by more than a factor 2 and does not depend on beam energy.

For Carbon wire, at low energy, the signal is reduced by 20 % and by a factor 12 at 87 keV (i.e an energy of 160 MEV for H^-). At high energy, the signal provided by charge deposition (e.g. 40 μA at 160 MeV H^- energy) is comparable to the signal due to SE (in the order of 20 μA , not simulated here, see Chapter 4 for more detail) but with opposite polarity and there is a not negligible probability to have a very low net signal.

As a general concern about these simulations, one must remind that the Monte Carlo simulations cannot track electrons with energy below 1 keV , thus enhancing the simulation results uncertainty.

1. For Carbon wires this result is strictly correct only for H^- beams below about 110 MeV , for which no electrons have enough energy to traverse the 33 μm wire. Above 110 MeV , the signal depends on energy since more and more electrons can escape despite the wire polarization.

H^- Energy	[MeV]	61	79	86	99	116	129	145	160	
Scattered e^- Energy	[keV]	33	43	47	54	63	70	79	87	
Carbon wire signal	[mA]	0.43	0.39	0.38	0.34	0.28	0.16	0.08	0.04	
w.r.t. ideal	[%]	83	75	73	65	54	31	15	8	
Tungsten wire signal	[mA]	0.29					0.28			
w.r.t. ideal	[%]	45					44			

Table A.2: Expected current on 33 μm Carbon wire and 40 μm Tungsten wire when accounting for stripped electrons scattering.

A.4 Profile reconstruction with Wire Scanners when accounting for stripped electrons scattering

At the moment the LINAC4 wire scanners design is based on the old CERN LPI devices and consists of a single fork traveling at 45° with respect to the beam axis, equipped with two wires mounted symmetrically (see Fig A.10). This would allow the sampling of the horizontal and vertical planes at exactly at the same time. Since the wires must be electrically decoupled, one wire is mounted few millimeters downstream the other.

Similarly to what discussed above for SEM grids, when considering the scattering of stripped electrons there is a certain probability that electrons emerging from the second wire reach the upstream one, thus perturbing its signal, i.e. generating a cross-talk.

Indeed, a measurable cross-talk has been observed at the SNS linac (that is equipped with similar devices) over a wide beam energy range. Even though not supported by calculations or simulations yet, such an effect has been attributed to the stripped electrons scattering, given the fact that the effect disappears when measuring proton beams instead of H^- .

With the aim of reproducing the SNS observations, we performed FLUKA simulations assuming 544 keV electrons (i.e. 1 GeV H^- energy). Even though this energy is not representative of the LINAC4 case, it has been chosen because

- the higher the energy, the lower the FLUKA uncertainties
- the scattering coefficient is almost constant from 10 keV to few MeV electron energy for Tungsten, as described in literature [17] and confirmed up to 87 keV by the simulations above

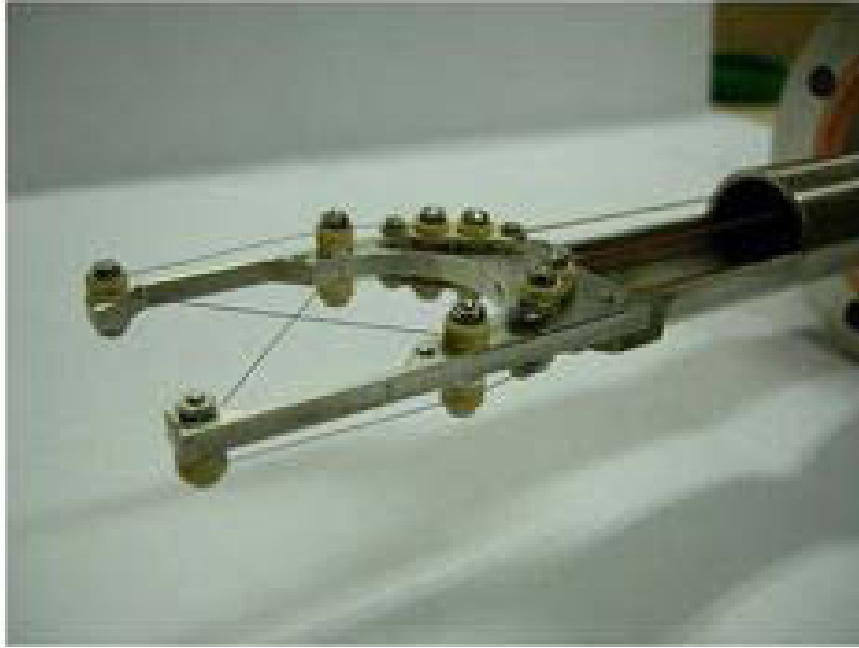


Figure A.10: Wire beam scanner used in the LPI (LEP injector), the two wires are used to sample the two transverse planes at the same time.

- the SNS observations include the 1 GeV case.

A.4.1 FLUKA simulations of the SNS 1 GeV H^- beam case

Two geometries have been simulated:

- a SEM grid with 24 Tungsten wires with a diameter of $100\ \mu\text{m}$ spaced of $500\ \mu\text{m}$.
- A wire scanner with two Tungsten wires with a $100\ \mu\text{m}$ diameter.

The two wires are separated by 1 mm along the z (beam) axis and one of them is off centered by 8 mm. The *off-centering* concept is illustrated in Fig A.11 and allows identifying any cross talk more easily, since during the scan the beam core crosses the two wires at different times. In the simulations, the scan has been performed by moving the beam.

As in the previous sections, the beam sizes are $\sigma_x = \sigma_y = 2\ \text{mm}$. For the SEM grid, the number of particles simulated was 10^7 , while for the wire scanner was 10^8 .

Fig. A.12 shows the reconstructed profile when considering the charge deposition

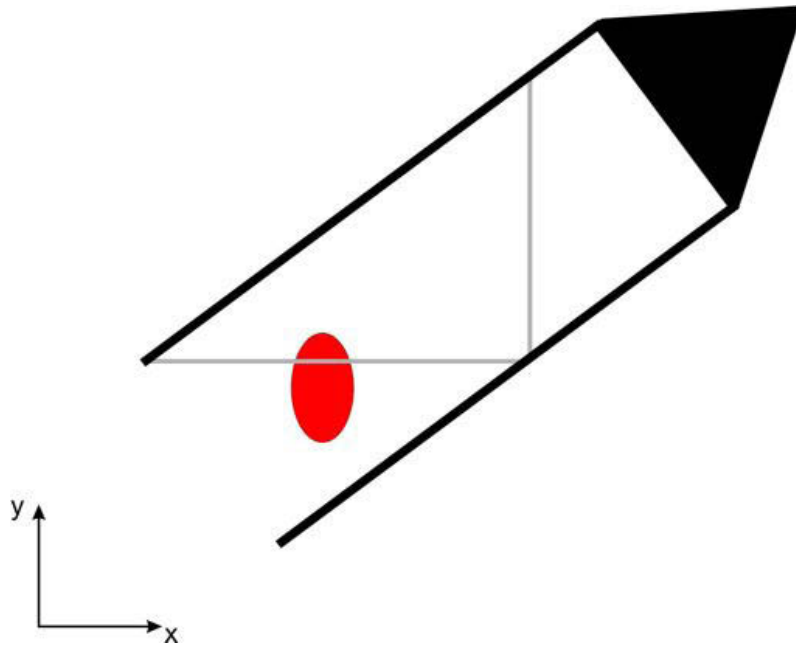


Figure A.11: Sketch of a wire scanner fork with off-centered wires, in order to separate in time any cross talk between wires originated by stripped electrons scattering.

in the wire (i.e. no SE, as in the case with polarized wires). The error on the reconstructed profile is less than 0.3 %.

Fig. A.13 shows the reconstructed profiles with wire beam scanner, in logarithmic scale. In this case, each profile point has been normalized to the peak signal. The beam profile of the wire positioned downstream (H plane on Fig. A.13) is reconstructed with an error of -0.11 %. The effect of scattering produces a cross talk appearing in the tail of the profile reconstructed with the upstream wire. As evident from the plot, the cross-talk is in the 10^{-3} level, at least one order of magnitude less than what observed at SNS.

A.5 Conclusion and outlook

The Monte Carlo simulations presented in this note could not fully reproduce the SNS observations about cross-talk between wire scanner wires, mainly attributed to stripped electrons scattering. According to the simulation results, even though for both SEM grids and Wire Scanners the expected signal can be reduced up to 55 % when accounting for electron scattering, the reconstruction of the beam profiles seems to be hardly affected. For all considered cases (different

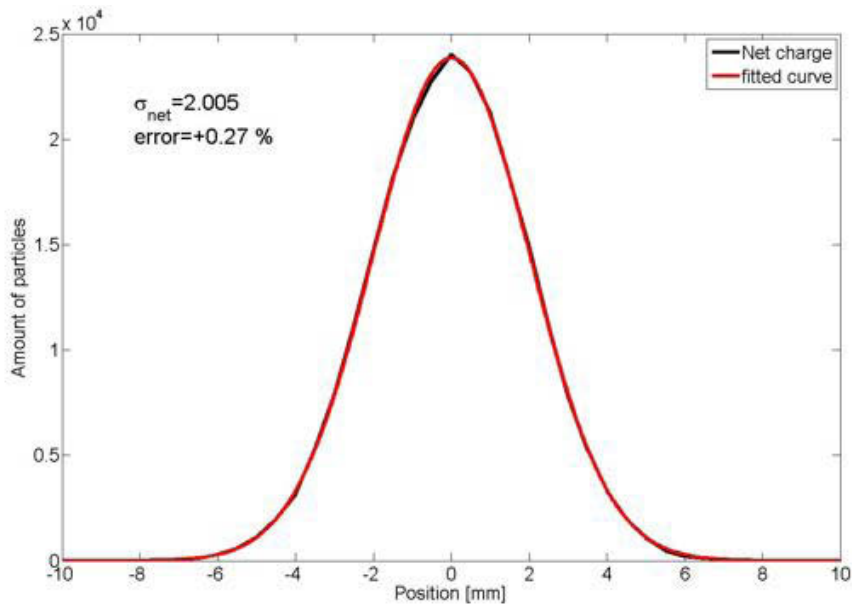


Figure A.12: Beam profile reconstruction with backscattering effect (black curve, Gaussian fit in red) for a $100 \mu\text{m}$ Tungsten wire at 544 keV electron beam energy.

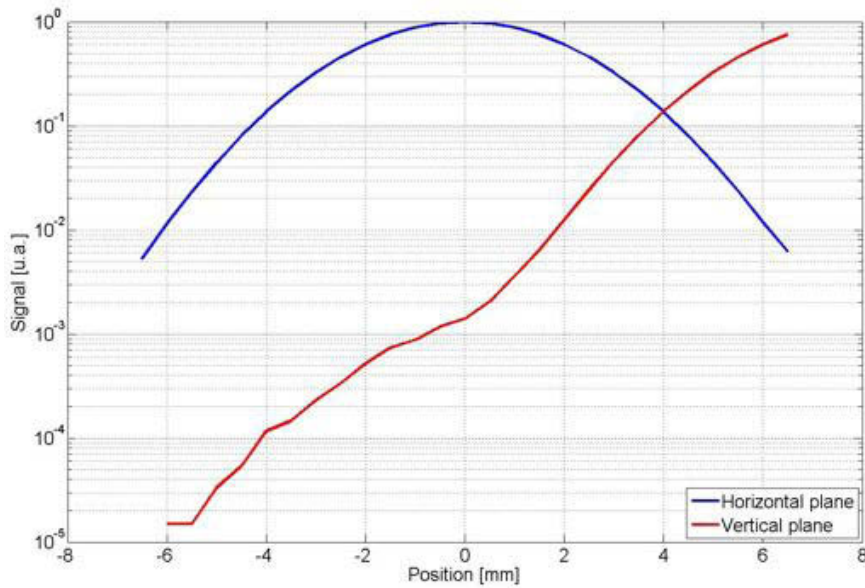


Figure A.13: Beam profile reconstruction from wire scanner. The kink in the vertical profile tail (red curve, upstream wire) is an indication of cross-talk from the horizontal profile wire due to stripped electrons scattering.

LINAC4 energies, 1 GeV SNS case, Carbon and Tungsten wires) the error on the measured beam size is expected to be below 1%.

A source of uncertainty could arise from the fact that the simulated electron beam was considered as representative of the real case (H^- beams interacting with the wires with the consequent scattering of stripped electrons), but for the moment we could not find any phenomena (e.g. space charge from H^- or so) that would indicate the contrary. In addition, it must be noted that the scattering coefficients (amount of stripped electrons emerging from the wire) determined with the FLUKA simulations agree very well with the data found in literature [17] and both the scattering coefficients and the scattering angles seems to be in agreement with similar studies performed at INR with GEANT4 [54].

In any case, it is advisable to slightly modify the LINAC4 wire scanners design by off centering the two wires, as was decided at SNS. With this configuration, even in the presence of an unpredicted signal perturbation, the signal cross talk would appear not simultaneously in time (the maximum signal on one wire, i.e. the maximum amount of scattering would appear shifted in time w.r.t. the maximum on the other wire).

In order to study more in detail the disagreement between the SNS observations and the simulations presented here, an experiment based on a 70 keV electron gun is in preparation at the CERN CTF3 facility. The idea is to test the two wires types foreseen for the LINAC4 SEM grids and wire scanners. For each type of wire, a SEM grid with 3 wires has to be fabricated. The pitch should be 500 μm . Each wire will be polarized at few hundred volts to suppress SE and connected to an individual acquisition channel. A collimator should be used to reduce the beam to less than 1 mm (6σ) and positioned in front of the central wire.

Bibliography

- [1] D. Warner, “Project study for a new 50 MeV linear accelerator for the cps,” 1973.
- [2] L. HEIN and A. LOMBARDI, “Update of the linac4-psb transfer line.”
- [3] W. W. et al, “160 MeV h^- injection into the cern psb,” Tech. Rep. CERN-AB-2007-0433.
- [4] M. Hori and K. Hanke, “Spatial and temporal beam profile monitor with nanosecond resolution for cern linac4 and spl,” *Nucl.Instr.Meth.*, no. A,588(2008) 359-374, 2008.
- [5] A. Feshenko, “Methods and instrumentation for bunch shape measurements,” in *Proc. of the PAC 2001*, 2001.
- [6] B. Dehning and al., “Lhc beam loss detector design : Simulations and measurements,” Tech. Rep. CERN-LHC-PROJECT-Report-1026, CERN.
- [7] K. Hanke and A. Lombardi, “Beam measurements for linac 4 and its transfer lines.”
- [8] D. Edwards and M. Syphers., *An Introduction to the Physics of High Energy Accelerators*. Wiley, 1993.
- [9] “Cas - cern accelerator school: 5th general accelerator physics course,” 1994.
- [10] A. Lombardi in *Joint University Accelerator School*.
- [11] *Particle Data Group*.
- [12] Peskin, *An Introduction to Quantum Field Theory**An Introduction to Quantum Field Theory*. Perseus Publishing, 1994.
- [13] N. Mott and H. Massey, *The Theory of Atomic Collisions, Third Edition*. Oxford University Press, 1965.
- [14] A. Halzen, Francis; Martin, *Quarks & Leptons: An Introductory Course in Modern Particle Physics*. John Wiley & Sons, 1984.
- [15] C. Lynch and O. Dahl *Nucl. Instrum. and Meth.*, no. B58 (1991) 6, 1991.
- [16] G. Moliere *Naturforsch.*, no. 2a (1947)133; 3a (1948) 78, 1948.

- [17] T. Tabata and R. I. S. Okabe *Nucl. Instrm. and Meth.*, no. 94 (I97I) 5o9-53, 1971.
- [18] Evans, “The atomic nucleus,” 1975.
- [19] L. Austin and H. Starke *Ann. Phys.*, no. vol. 9, 1902.
- [20] D. H. ans S. Hippler and A. Scharmann, “Ion-induced secondary electron spectra from clean metal surface,” 1987.
- [21] H. Rothard, “Secondary-electron yields from thin foils: A possible probe for the electronic stopping power of heavy ions,” *Phys. Rev.*, no. A 41, 2521 - 2535 (1990), 1990.
- [22] J. Ashley, C. Tung, and R. Ritchie, “Electron inelastic mean free paths and energy losses in solids,” *Surface Science* 81., 1979.
- [23] E. Sternglass, “Theory of secondary electron emission by high speed ions,” *Phys. Rev.*, no. 108(1957) 1, 1957.
- [24] P. Koschar and al., “Secondary-electron yield as a probe of preequilibrium stopping power of heavy ions colliding with solids,” *Phys. Rev.*, no. A 40, 3632-3636, 1989.
- [25] E. Silveira and J. Jeronymo, “Secondary electron emission from the entrance and exit surfaces of thin aluminium foils under fast light ion bombardment,” *Nucl. Instrm. and Meth.*, no. B24/25, 1987.
- [26] D. Kramer, *Design and Implementation of a Detector for High Flux Mixed Radiation Fields*. PhD thesis, 2008.
- [27] A. S. Artemov, Y. K. Baigachev, A. K. Gevorkov, and A. O. Sidorin *Zh. Tekh. Fiz*, 1998.
- [28] R.C.Webber and C.Hojvat, “Measurement of the electron loss cross sections for negative hydrogen ions on carbon at 200 MeV,” *IEEE Trans. Nucl. Sci.*, no. 26, 4012 (1979), 1979.
- [29] E. Bravin, “Thermal analysis of a diagnostic metallic foil for the ctf3 injector.”
- [30] S. Grigoriev and E. Meilikhov, *Handbook of Physical Quantities*. 1997.
- [31] G. Bellodi, “User specifications for linac4 test bench diagnostics.”
- [32] A. Fasso, A. Ferrar, J. Ranft, and P. Sala, “Fluka: a multi-particle transport code,” 2005.
- [33] A. Perrin, J.-F. Amand, and T.Muetze, “Travel user manual.”
- [34] F.Ziegler and J. Biersack
- [35] p. Verdier and F. Arnal *Compt. Rend.*, vol. 267, p. 1443, 1968.
- [36] j. G. Trump and R. J. V. de Graaff *Phys. Rev*, vol. 75, p. 44, 1949.

- [37] C. Bovet and al., “Wire scanner for lhc,” 1997.
- [38] “Ansys simulation code.”
- [39] A. D. F. Carra, “Linac4 3MeV test stand: Thermo-mechanical fatigue analysis of the slit,” 2010. edms document 1102151.
- [40] E. Berthome, “Rapport de conception du slit assembly pour ligne de mesure 3 MeV linac4,” tech. rep.
- [41] “Cst microwave studio.”
- [42] R. Scrivens, “Engineering parameters for diagnostics for a source test line for linac4,” Tech. Rep. L4-B-EP-0001.
- [43] A.Zhukov, A.Aleksandrov, and A.Shishlo, “Transverse emittance measurements in mebt at sns,” in *Proceedings of LINAC10*, 2010.
- [44] J.Pogge, “Sns emittance scanner, increasing sensitivity and performance through noise mitigation ,design, implementation and results,” *AIP Conf. Proc.*, vol. 868, pp. 435–444, 2006.
- [45] H. K and H. T, “Transverse emittance measurement with the three-monitor-method at the cern linac4,” Tech. Rep. CERN-sLHC-PROJECT-Report-0033, CERN, 2010.
- [46] Y. Liu, C. Long, C. Peters, and A. Aleksandrov, “Measurement of ion beam profiles in a superconducting linac with a laser wire,” *Applied Optics*, vol. 49, pp. 6816–6823, 2010.
- [47] Y. Liu and Al., “Laser based diagnostics for measuring h^- beam parameters,” in *PAC 2011 proceedings*, no. WEOCN1, 2011.
- [48] H. Bryant and G. Herling, “Atomic physics with a relativistic h^- beam,” *Journal of Modern Optics*, vol. 53, 2006.
- [49] C. Hill and Al., “Preliminary notes: h^- ions stripping in transport by thermal photon.” December 2004.
- [50] G. Gillespie and Al., “Double closure calculation of the electron-loss cross section for h^- in high h^- energy collisions with h and he,” *Phys*, vol. A 15, 1977.
- [51] B. Gervais and Al., “Simulation of excited-state formation of hydrogen in transmission of relativistic h^- ions through thin foils,” *Phys. R*, vol. A 53, 1996.
- [52] P. Kurpick and Al., “Excited-state subshell population of hydrogen atoms after transmission of relativistic h^- ions through thin foils,” *Phys. Rev.*, vol. A 58, 1998.
- [53] “Cividec.”
- [54] A. Feshenko, “Private communication.”